2018-12-05

Cement-Based Composites for Rehabilitation of Concrete Structures

Houman Akbari Hadad
University of Miami, houman@miami.edu

UNIVERSITY OF MIAMI

CEMENT-BASED COMPOSITES FOR REHABILITATION OF CONCRETE STRUCTURES

By

Houman Akbari Hadad

A DISSERTATION

Submitted to the Faculty
of the University of Miami
in partial fulfillment of the requirements for
the degree of Doctor of Philosophy

Coral Gables, Florida

December 2018

UNIVERSITY OF MIAMI

A dissertation submitted in partial fulfillment of
the requirements for the degree of
Doctor of Philosophy

CEMENT-BASED COMPOSITES FOR REHABILITATION OF CONCRETE STRUCTURES

Houman Akbari Hadad

Approved:

Antonio Nanni, Ph.D. Professor and Chair Civil, Architectural, and Environmental Engineering	Quingda Yang, Ph.D. Professor Mechanical and Aerospace Engineering
Landolf Rhode-Barbarigos, Ph.D. Assistant Professor Civil, Architectural, and Environmental Engineering	Prannoy Suraneni, Ph.D. Assistant Professor Civil, Architectural, and Environmental Engineering
Francisco De Caso y Basalo, Ph.D. Associate Scientist Civil, Architectural, and Environmental Engineering	Guillermo Prado, Ph.D. Dean of the Graduate School

AKBARI HADAD, HOUMAN (Ph.D., Civil Engineering)

Cement-Based Composites for Rehabilitation of Concrete Structures (December 2018)

Abstract of a dissertation at the University of Miami.

Dissertation supervised by Professor Antonio Nanni.
No. of pages in text. (138)

Inorganic based composites are a new class of materials used in strengthening and rehabilitation of masonry and concrete structures. In the literature, these composites have been identified using different terminology, among which, Fabric Reinforced Cementitious Matrix (FRCM) and Steel Reinforced Grout (SRG) are adopted by the North American guidelines and acceptance criteria. FRCM fabric/s may consists of carbon, aramid, glass, basalt or polyparaphenylene benzobisoxazole (PBO) fiber rovings that are embedded in an inorganic matrix. SRG shares the same technology with FRCM, except that the fabrics consist of twisted galvanized steel wires which form steel cords. Developed as alternatives to fiber-reinforced polymer (FRP) composites, FRCM provides a better compatibility to masonry/-concrete substrate and superior resistance to high temperatures, ultraviolet radiation, and moisture by virtue of their cementitious matrix.

The purpose of this doctoral dissertation is to provide a better understanding of mechanical behavior of FRCM/SRG for rehabilitation and strengthening of concrete structures including the transportation infrastructure. The dissertation is a combination of three individual but interconnected studies. In the first study, mechanical properties of various FRCM/SRG composites were investigated. The objective of the second study is to discuss the effectiveness of FRCM/SRG composites

to improve the flexural strength of reinforced concrete (RC) beams. An appealing use of FRCM composites is in RC bridges which are subject to cycles of loading and unloading from the vehicular traffic, and thus, liable to fatigue failure. Therefore, the last study regards the fatigue performance of FRCM-strengthened RC beams.

To my family and friends.

Acknowledgements

I would like to thank my advisor Dr. Antonio Nanni for his exemplary mentorship. He has inspired me time and again throughout this course of studies.
I wish to thank Dr. De Caso for his extended support and his excellent consultancy. I would like to thank my dissertation committee members; Dr. Prannoy Suraneni and Dr. Landolf Rhode-Barbarigos, your discussion, ideas, and feedback have been absolutely invaluable.
I would like to express my gratitude and appreciation to Dr. Vanessa Pino and Dr. Diana Arboleda, from whom I gained plenty of knowledge. A part of this dissertation is a result of direct collaboration with Dr. Pino.
I would like to extend my sincere thanks to Dr. Gianmarco de Felice and Dr. Stefano De Santis for their collaboration in a comparative study which is a part of this dissertation.
I am blessed, for my colleagues were indeed my friends.
Thanks are in order to the Structures and Materials Lab personnel, Keith Holmes, Phil Lavonas, Ana De Diego, Christian Marquina, Roger Solis, Ming Han Soh, Thomas Nanni, and Tais Hamilton for their endless help.
I would also like to extend my deepest gratitude to my fellow graduate students, Mahsa, Marco, Saverio, Pietro, Thomas, Alvaro, Davide, Leire, Vanessa, Janna, Morteza, Carlos, Guillermo, Omar, Guan, Pedro, Khashayar, Babak, Siva, Katelyn, and Busra.
The project was made possible with the financial support received from the University Transportation Center RE-CAST and the Qatar National Research Fund.

HOUMAN AKBARI HADAD

University of Miami

December 2018

Table of Contents

List of Figures

List of Tables

Abbreviations

AASHTO American Association of State Highway and Transportation Officials

AC Acceptance Criteria

ACI American Concrete Institute

ASCE American Society of Civil Engineers

ASTM American Standards for Testing and Materials

CICI Center for Integration of Composites into Infrastructure

DOT Department of Transportation

COV Coefficient of Variation

FHWA Federal Highway Administration

FRCM Fabric Reinforced Cementitious Matrix

FRP Fiber Reinforced Polymer

IBC International Building Code

ICC-ES International Code Council Evaluation Services

LVDT Linear Variable Differential Transducer

NCHRP National Cooperative Highway Research Program

NSF National Science Foundation

PBO Polyparaphenylene Benzobisoxazole

PSY Percent of the Static Yield

RC Reinforced Concrete

S-N Stress vs. Number of Cycles Curve

TRC Textile Reinforced Concrete/Cement

TRM Textile Reinforced Mortar

UTC University Transportation Center

Chapter 1

Introduction

The current age and state of buildings and the infrastructure in the U.S. and Europe indicates that the demand for strengthening and rehabilitation technologies is growing (Herrmann, 2013). Accordingly, manufacturers are responding to market demands with several novel technologies, among which are externally bonded, thin laminated composites. The use of thin laminated composites in construction as a strengthening and rehabilitation solution has been the subject of various studies for well over three decades (Alexander, 1991; Ahmed & Robles-Austriaco, 1991; Mourad & Shannag, 2012). Laminated composites are high strength, light weight, flexible in shape, and easy to install. Furthermore, the design professional has the freedom to engineer these materials to meet the specific application requirements by choosing the fiber type, fabric orientation, and number of fabric layers.

Among the currently available systems are Fabric Reinforced Cementitious Matrix (FRCM) and Steel Reinforced Grout (SRG). FRCM and SRG are composed of an inorganic matrix that embodies a load-bearing fabric. The inorganic matrix can be cement-, lime-, or geopolymer-based mortar, for which the term "cementitious" is

used in what follows. The cementitious matrix rather than being a generic mortar, is specifically formulated to be compatible with its fabric and the substrate. The inorganic nature of the FRCM matrix is aesthetically and chemically compatible with concrete and masonry substrates. The fabric is in the form of largely-spaced yarns or cords of synthetic fibers which allow proper mortar penetration. Currently, common FRCM fabric types are mineral based fibers of glass and basalt or polymer-based fibers of carbon, aramid, and polyparaphenylene benzobisoxazole (PBO). FRCM fabrics can be uni- or bidirectional. SRG fabrics, on the other hand, consist of high-strength metallic micro-cords which are twisted together to form cords. This metallic cords are then stitched to plastic fibers in the perpendicular direction to form unidirectional fabrics. FRCM fabrics can be dry or coated to improve the matrix-to-fabric bond.

Various studies confirm the effectiveness of FRCM/SRG composites in strengthening RC structures. Experimental investigations on full-scale structural members have been carried out under shear (Triantafillou & Papanicolaou, 2006; Loreto et al., 2015; Ombres, 2015b; Gonzalez-Libreros et al., 2017; Aljazaeri & Myers, 2017; Azam et al., 2017), axial (Ombres, 2014; Colajanni et al., 2014; Minafò & La Mendola, 2018) and bending (Pino et al., 2016; Papanicolaou et al., 2009; D'Ambrisi & Focacci, 2011; Babaeidarabad et al., 2014) stresses.

FRCM/SRG has proven effective to improve the performance of masonry structures. Tests have been conducted on walls under in-plane (Prota et al., 2006; Papanicolaou et al., 2007; Faella et al., 2010; Babaeidarabad & Nanni, 2013; Marcari et al., 2017; Ismail et al., 2018) and out-of-plane (Papanicolaou et al., 2008; Babaeidarabad et al., 2013; Valluzzi et al., 2014; De Santis et al., 2016; Bellini et al., 2018;

Kariou et al., 2018) actions, on arches and vaults (Borri et al., 2009; Garmendia et al., 2014; Alecci et al., 2016; Ramaglia et al., 2016; Cescatti et al., 2018; De Santis et al., 2018), and on columns (Carloni et al., 2014; Fossetti & Minafò, 2016; Ombres, 2015a; Santandrea et al., 2017).

Among FRCM/SRG shortcomings are a brittle matrix with a strain to failure lower than that of the fabric, and a lower bond strength at the fabric-matrix and matrix-substrate interfaces. Studies suggest that loss of bond, either at fabric-matrix or at matrix-substrate interfaces, is the predominant failure mode of the FRCM/SRG strengthened members in flexure (Pino et al., 2017; Akbari Hadad et al., 2018). Moreover, the matrix bond strength limits the maximum effective number of fabric layers (thus, the maximum attainable increase in strength) of an FRCM/SRG system (Pino et al., 2017). Due to the peculiar bond interaction between yarns and mortar, various parameters such as number of fabric layers, fabric architecture and coating, and mortar thickness nonlinearly affect the mechanical performance of the FRCM/SRG materials (Pino, 2016) (Arboleda, 2014).

1.1 Background

Ferrocement can be named the first structural cementitious based composite, which was patented in 1855 by Lambot in France (Naamann, 2012). Nonetheless, ferrocement technology was almost absent in construction industry until the commercial development of concrete. It consists of continuous reinforcement embedded in a cementitious matrix of about 50 mm thickness. The idea of using

ferrocement as a strengthening and rehabilitation technology dates back to the 1990s where ferrocement laminates were used to repair damaged wooden vessels (Alexander, 1991) and reinforced concrete (RC) members (Ahmed & Robles-Austriaco, 1991). Studies reported an increase in ultimate capacity of strengthened beams (Al-Kubaisy & Jumaat, 2000) and columns (Kazemi & Morshed, 2005). However, the application of ferrocement for strengthening and rehabilitation purposes remained limited, and it was mainly used as a stand-alone structural member in new construction (Naamann, 2012).

In parallel, sophisticated polymer-based composites were developed in the 1960s and 1970s to meet superior performance challenges of space exploration and air travel. Widely known as fiber reinforced polymers (FRP) or fiber reinforced plastics, these composites consist of layer(s) of high strength fabric made of carbon, glass, basalt, or aramid fibers embedded in a polymeric matrix (Nanni, 1993). The application of FRP was limited to the niche technologies in aerospace and defense industries at the outset (Bakis et al., 2002). By the early 1990s, the cost of FRP manufacturing was reduced, and the technology became available to other industries. During the 1990s, FRP was used to strengthen or rehabilitate concrete and masonry structures. FRP installed by external lay-up has been proven effective to rehabilitate and strengthen existing reinforced concrete (RC) (Nanni, 1995), masonry (Hamid et al., 1994), and steel (Zhao & Zhang, 2007) structures. Various studies concluded that externally bonded FRP laminates effectively improve axial, shear, and flexural capacity of structural elements (Nanni, 1993) (Balaguru et al., 2008). By virtue of their high strength to weight ratio, these composites can provide a significant upgrade in terms of ultimate bearing capacity with a negligible

added mass to the original structure. Moreover, externally bonded composites are applied to the outer surface of the structural elements, and can take any shape to fit the contour of elements being strengthened, which makes the installation process versatile, fast, and economic.

Nevertheless, FRP composites showed some limitations in practice. Firstly, the polymeric matrix is sensitive to heat (Bisby et al., 2005). Secondly, the application of FRP materials on wet surfaces (e.g., inner surface of tunnels) is problematic, and FRP is not permeable. The latter can introduce problems in masonry substrates, where the polymer matrix can trap the moisture within the masonry and lead to loss of bond between the substrate and the matrix.

FRCM and SRG replaced the resin matrix of the FRP with an inorganic (cementitious) one. Put differently, the new FRCM/SRG substituted the steel reinforcement of ferrocement with high strength synthetic fabrics. The main difference of these FRCM/SRG systems with ferrocement is that they are designed specifically for strengthening of existing structural elements, and not as a stand-alone structural material.

In defiance of their terminology, FRCM and SRG shared the same technology having an inorganic matrix reinforced with a fabric. The mortar-base matrix of FRCM/SRG systems offers resistance to the elevated temperatures (Donini et al. 2017), ultraviolet radiation, and moisture. In contrast with FRP, mortar-based composites could be installed on wet or uneven surfaces.

1.2 Research Objectives

The overall objective of this research is to better understand the mechanical performance of FRCM/SRG systems as a rehabilitation and strengthening technology for concrete structures. This dissertation is composed of three individual, but interconnected studies as follows.

1.2.1 Material Characterization

In the process of technology deployment, material characterization methods are a key prerequisite, which should produce representative values to be used in evaluating and designing strengthened structural members. Correspondingly, the acceptance criteria for tensile characterization is essential to ensure that the composite materials possess the required structural performance and durability under projected service conditions. Finally, test standards are necessary in order to obtain material characteristics and performance of composite systems in a controlled, scientific, and reproducible manner. In the U.S., the acceptance criteria AC434 ICC-Evaluation Service (2016) was first published for FRCM composites and later expanded to include the SRG systems. ICC-ES can issue an evaluation service report, which demonstrates compliance with the model building code, and thus building officials can accept the use of FRCM/SRG in a strengthening project. According to the AC434, design values of FRCM/SRG systems are to be obtained through tensile test on composite coupons using clevis grips (i.e., without applying lateral pressure in the gripping zone).

The first part of this dissertation seeks to investigate the basic constitutive behavior of FRCM and SRG composites. Influence of number of fabric layers, fabric archi-

tecture, fiber/matrix ratio, mortar properties, and test-setup boundary conditions on overall performance of the composite were considered.

1.2.2 Structural Performance

The second part of this the dissertation is focused on the flexural performance of FRCM/SRG strengthened RC beams and slabs. First, existing design guidelines were used to analytically compute the capacity of the strengthened RC beams. The FRCM/SRG characteristic values obtained earlier were used to analytically determine yielding and ultimate capacities of the FRCM/SRG strengthened RC beams according to the ACI 549.4R-13 (American Concrete Institute (ACI), 2013). The strengthened RC beams were then tested. The experimental and analytical values were compared. Failure mechanisms and the influencing factors in flexural performance of the RC beams were discussed.

1.2.3 Fatigue Behavior

An appealing application of FRCM composite is to strengthen or rehabilitate structurally deficient RC bridges. Bridges sustain cyclic service loads due to vehicular traffic, which makes them vulnerable to fatigue failure (Paris, 1961). The dominant design approach of components subject to cyclic loading is to minimize the material flaws in manufacturing, and to hold the stress levels low enough to avoid crack initiation (Bathias & Paris, 2004). This "damage tolerance" method determines the crack growth under fluctuating stresses, or endurance limit, assuming that the flaws already exist in component materials.

Thus, the relation of applied cyclic stress range to endured number of cycles (or

S-N curves) becomes the basis for design.

Fatigue behavior of FRCM-strengthened RC beams as a measure of their long-term performance is the last component of this dissertation. Experimental fatigue studies were performed on glass and carbon FRCM strengthened RC beams. Since the beams and test setup were identical to those used by Pino (2016), the results were combined to provide a better assessment of fatigue behavior of FRCM strengthened RC beams. The FRCM mechanical properties from the first study and the flexural behavior of FRCM-strengthened RC beams under monotonic loading from the second study were used in the analysis. Beams were tested under cyclic loading with variable applied peak load. Fatigue life and failure mechanisms were studied. Combined S-N curves of PBO, carbon, and glass FRCM strengthened RC beams allow to draw new recommendations for fatigue life. The ultimate goal of this study was to develop a fatigue endurance limit which contributes to the guidelines for the design of externally bonded FRCM strengthening systems.

1.3 Acceptance and Design

When an FRCM/SRG system is developed, it must undergo various tests and meet certain criteria in order to be considered for structural application. The ICC Evaluation Services (ICC-ES) created a document titled "Acceptance Criteria for Masonry and Concrete Strengthening Using Fabric-reinforced Cementitious Matrix (FRCM) and Steel Reinforced Grout (SRG) Composite Systems (AC434)" which defines the test methods and related acceptance criteria to be performed by an accredited laboratory in order to produce a product research report. The Interna-

tional Building Code (IBC) (Section 104.11.1) requires a product research report for any new material and technology in order for it to be used in structural design. For the FRCM/SRG the following parameters are evaluated: material properties, axial, flexural and shear capacity, durability (environmental exposure) performance, fire performance, and structural design procedures. In particular, AC434 Annex A outlines the test procedure and data analysis which yields the tensile properties of FRCM. The tensile testing of FRCM is a critical component of this research; therefore, Annex A of AC434 is included in Appendix A of this dissertation.

ACI 549.4R-13 "Guide to Design and Construction of Externally Bonded Fabric Reinforced Cementitious Matrix (FRCM) Systems for Repair and Strengthening Concrete and Masonry Structures" was developed by the American Concrete Institute (ACI), and contains all necessary tools for the effective design and construction of FRCM system. It covers the many aspects of FRCM including: background information, installation guidelines, field applications, material properties for different systems, system qualifications, design guidelines (axial, flexural, and shear capacities), reinforcement details, and design examples. The material properties determined from AC434 are used by ACI 549.4R-13 to effectively design externally bonded FRCM/SRG systems for strengthening RC and masonry structures. The design methodology provided in ACI 549.4R has been used in study 2 and study 3 of this dissertation, where FRCM/SRG systems are designed for the strengthening of RC beams.

(a) AC434

(b) ACI 549.4R

Figure 1.1: Codes

Chapter 2

Material Characterization

In accordance with AC434 guidelines, the mechanical properties of FRCM systems are obtained from direct tensile tests performed on FRCM composite coupons. In the test method, axial load is transferred from a universal test frame through clevis grips. The composite coupon is connected to the clevis grips through two sets of metal tabs adhered to its ends. The following parameters are derived from clevis-grip tensile tests on FRCM coupons.

- Maximum load before failure, P_{max};
- Tensile modulus of elasticity of the cracked specimen, E_f;
- Ultimate tensile strain, ϵ_{fu};
- Tensile strain corresponding to the transition point (i.e., the point at which the two lines that represent the uncracked and cracked behavior intersect), ϵ_{ft};
- Ultimate tensile strength, f_{fu};

- Tensile stress corresponding to the transition point, f_{ft}.

Fig. 2.1 shows the FRCM/SRG typical stress-strain curve and the simplified bilinear model.

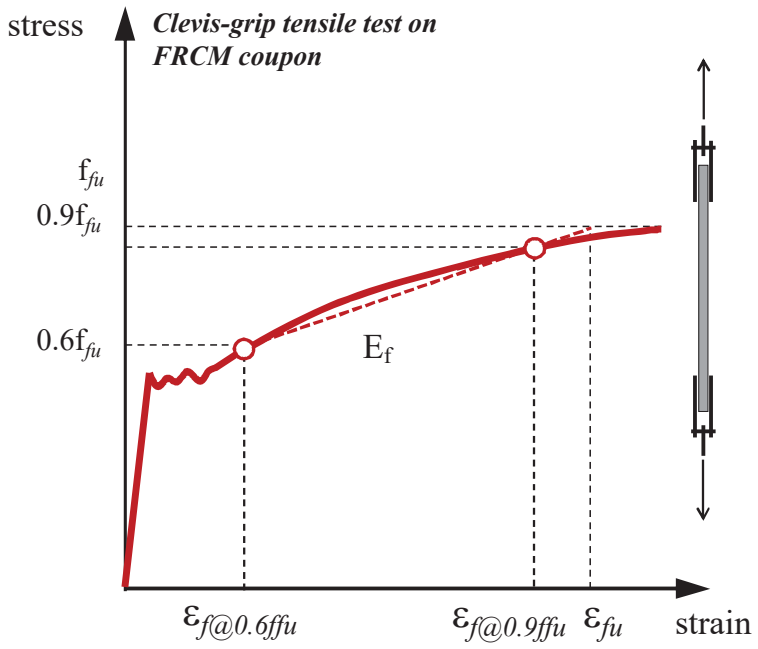

Figure 2.1: Typical stress vs. strain curve per AC434 test method

The fabric cross-sectional area is calculated as the product of the equivalent (or design) thickness and the effective width of the fabric, both in direction normal to the load. The equivalent thickness (generally provided by the supplier) is computed as the surface mass density of the fabric yarns parallel to the load application direction divided by the bulk density of the material of the dry fibers. The effective width is the product of the number of load-aligned yarns per fabric layer and the mid-yarn spacing. For design purposes, AC434 reduces the FRCM ultimate strength and strain to the average value of the test results minus one standard deviation, whereas the tensile elastic modulus is the average value of experimental

test results. According to ACI 549.4R-13, the FRCM systems is assumed to behave as linear elastic to failure and the effective stress value (f_{fe}) associated with an effective strain level (ϵ_{fe}) is determined using the tensile modulus of elasticity of the cracked FRCM as $f_{fe} = \epsilon_{fe} E_{fd}$. Finally, based on the type of application (flexural, shear, or axial), ACI 549.4R-13 sets further limitation for ϵ_{fd}.

From a mechanical standpoint, this test method aims at simulating a repair application in which the composite is not anchored at its ends and whose response mainly relies upon the bond at the fabric-matrix interface. The possible occurrence of either the tensile rupture of the fabric or its slippage within the matrix are both accounted at once and the obtained FRCM mechanical parameters are directly used in the design, without the need of performing shear bond tests. On the other hand, other possible shear bond test failure modes are not taken into account, which might pose a question about the possibility of using this method for all kinds of FRCM systems and substrates. Finally, the tensile modulus of elasticity of the cracked specimen includes both the elastic elongation of the fabric and its slippage within the matrix, which takes place after cracking.

2.1 Constituent Materials

Five different FRCM in addition to four SRG systems were tested in this study. The composite systems are as follows:

- **B200-L0-F**: A balanced bidirectional basalt fabric with a natural hydraulic lime based mortar modified with geopolymeric binders

- **G225-C1-F**: A balanced bidirectional glass fabric with a two-component ready-mixed pozzolan-reaction fiber-reinforced cement based mortar
- **G360-L0-F**: An unbalanced bidirectional fabric consist of glass in the main and aramid in the secondary direction with a natural hydraulic lime based mortar modified with geopolymeric binders
- **C440-C2-F**: A unidirectional carbon fabric with polypropylene-fiber reinforced cement based mortar
- **C130-C2-F**: A balanced bidirectional carbon fabric with polypropylene-fiber reinforced cement based mortar
- **S600-L0-S**: A unidirectional steel fabric with a natural hydraulic lime based mortar modified with geopolymeric binders
- **S600-G0-S**: A unidirectional steel fabric with a geopolymeric based mortar comprising natural kaolin and bauxite binders
- **S1200-L0-S**: A unidirectional steel fabric with a natural hydraulic lime based mortar modified with geopolymeric binders
- **S1200-G0-S**: A unidirectional steel fabric with a geopolymeric based mortar comprising natural kaolin and bauxite binders

Fig. 2.2 show the fabrics used in the FRCM/SRG systems above.

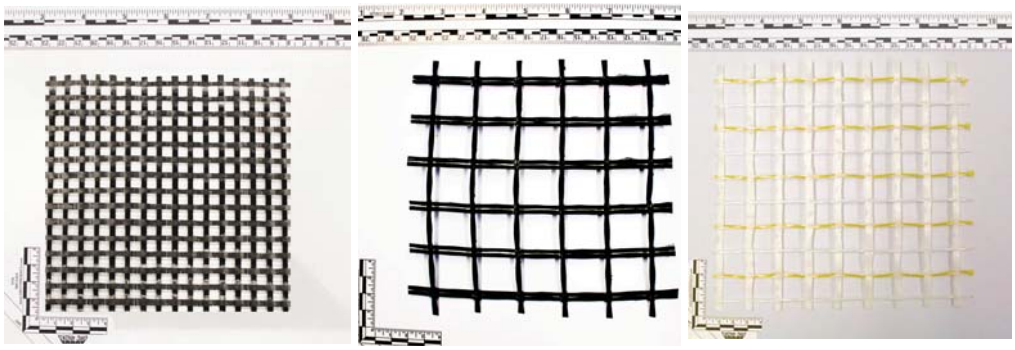

(a) B200 (b) G225 (c) G250

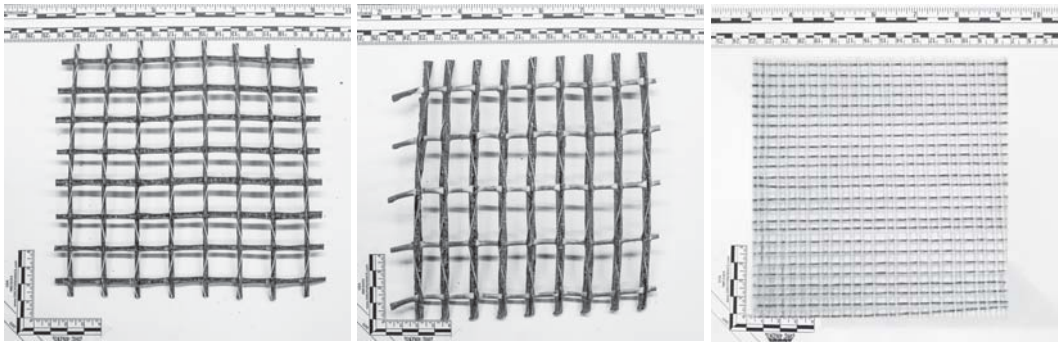

(d) C130 (e) C440 (f) S600

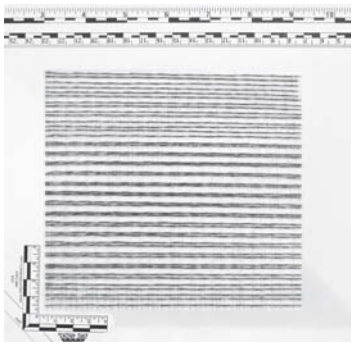

(g) S1200

Figure 2.2: FRCM/SRG Fabrics

Table 2.1: Constituent material properties

Composite System	Fabric Properties						Matrix Properties		
	γ_f $[g/m^2]$	i_f $[mm]$	t_f $[mm]$	f_f $[MPa]$	E_f $[GPa]$	ϵ_f [%]	f_{mc} $[MPa]$	E_m $[GPa]$	f_{mt} $[MPa]$
B200-L0-F	200	17x17	0.032	1718	70	1.9	20.6	13.3	5.4
G225-C1-F	225	25x25	0.035	1285	72	1.8	25	10	8
G250-L0-F	250	15x18	0.031	1580	80	2.2	20.6	13.3	5.4
C440-C2-F	440	12	0.157	2866	191	1.5	52	26.8	4.8
C130-C2-F	130	14x14	0.044	3136	209	1.5	52	26.8	4.8
S600-L0-S	670	6.35	0.084	2800	190	1.5	20.6	13.3	5.4
S600-G0-S	670	6.35	0.084	2800	190	1.5	56.3	22	10.3
S1200-L0-S	1200	3.2	0.168	3000	190	2	20.6	13.3	5.4
S1200-G0-S	1200	3.2	0.168	3000	190	2	56.3	22	10.3

Properties of each FRCM/SRG system, namely, fabric surface mass density γ_f, grid spacing i_f, equivalent thickness t_f, fiber tensile strength f_f, fiber elastic modulus E_f, fiber ultimate strain ϵ_f, mortar compressive strength f_{mc}, mortar Young's modulus E_m, and mortar tensile strength f_{mt} are listed in Table 2.1.

2.2 Test Setup

These tests determine the mechanical properties of FRCM/SRG systems following the test guidelines of AC434 Annex A. FRCM/SRG coupon specimens were cut from larger panels manufactured using a manual impregnation technique in a rectangular mold.

In manufacturing the panels, first a 5-mm thick layer of the cementitious matrix

was applied, then a layer of fabric was placed and lightly pushed into the first layer of matrix. Eventually the top layer of matrix was applied to form the surface of the specimen.

Panels were cured for 28 days at 22 degrees Celsius and 95% relative humidity before cutting and conditioning can be performed. Fig. 2.3 shows the panel and coupon preparation.

Clevis-grip direct tensile tests were performed on coupons cut from FRCM/SRG panels using a diamond blade wet-saw. Primary direction of the fabric was aligned with the length of panels.

Nominal dimensions of test coupons were 500 mm x 50 mm x 13 mm (length x width x thickness). Four steel tabs were attached to the ends of each coupon with high strength epoxy. Bonded tab length was 250mm. Clevis grips were attached by a pin to the ends of the metal tabs, as shown in Fig. 2.4. Tests were performed using a universal screw-driven test frame, with a maximum capacity of 130 kN. Tests were performed under displacement control at a rate of 0.25 mm/min.

In order to engage the clevis grip mechanism, a pre-load of less than 5% of the anticipated ultimate load was applied to the specimens. Values of strain were measured using an extensometer over a 100 mm gauge length.

(a) FRCM/SRG panel

(b) FRCM/SRG coupon

(c) Test specimen

Figure 2.3: FRCM/SRG Fabrics

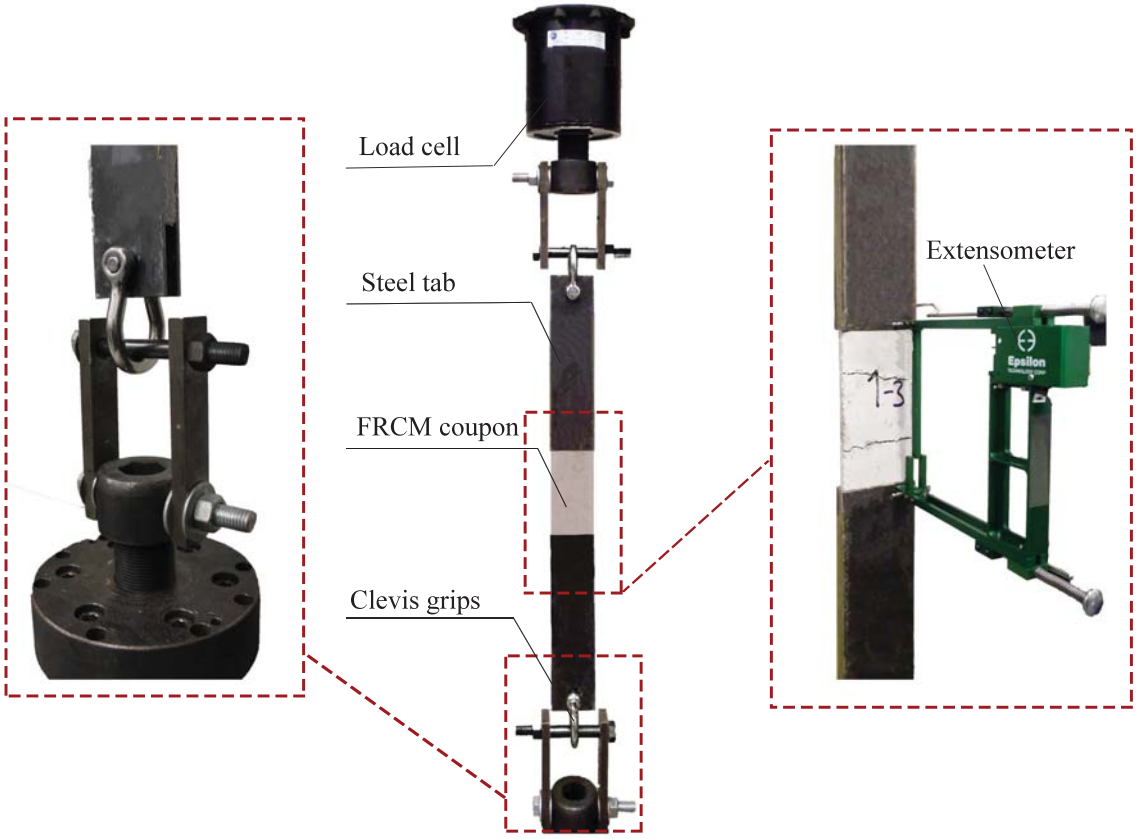

Figure 2.4: Direct tensile test setup per AC434

2.3 Experimental Results

Mechanical properties of each composite system is given in Table 2.2. In the table, stresses were computed based on the fabric cross-sectional area, which rendered the values of stresses independent from the thickness of the matrix and from the width of the specimen. Ten specimens were tested for each material type.

The predominant failure mode of all FRCM materials systems was specimens was slippage of fabric within the matrix, which was attained after multiple through-cracks developed. Once the crack pattern was stabilized (no new cracks formed), the imposed displacement was accommodated by crack opening, which required fiber yarns to slip within the matrix. Since failure occurred when the bond between fabric and matrix was lost at one end or throughout the specimen length, the performance of FRCM specimens depended primarily on the bond characteristics at the fabric-matrix interface.

SRG specimens exhibited a different behavior. The fabric slippage was lower with respect to the other FRCM systems,revealing a better bond between the twisted galvanized steel cords and mortar. The applied displacement was accommodated by the formation of multiple micro-cracks and cracks of small width throughout the monitoring length.

Failure started when the shear bond stress at the fabric-matrix interface was sufficient to form a rupture surface. Longitudinal cracks were initiated at the location of perpendicular cracks and developed aligned with and parallel to the primary direction of the fabric. Eventually the failure occurred by splitting of mortar due to longitudinal cracks with the steel cords still linear elastic. Thus, the performance of mortar and its strength in the net area through the steel cords governed the mechanical behavior of the SRG.

Fig. 2.5 shows the typical failure modes of FRCM and SRG specimens as discussed. The effect of mortar strength on the overall performance of SRG systems was studied by comparing S600-L0-S and S600-G0-S systems which share the same fabric, but use two different mortars.

As showed in Table 2.1, the G0 is a geopolymeric binder which has higher strength and modulus compared to the L0 lime-based mortar. As a result, the ultimate strength and modulus of elasticity of S600-G0-S are significantly higher than those of S600-L0-S. The same trend was observed comparing S1200-L0-S and S1200-G0-S material systems.

The ultimate tensile strength of the FRCM and SRG was significantly lower than the nominal strength of the dry fibers because fabric-matrix bond performance and matrix strength governed the ultimate performance of FRCM and SRG, respectively.

A high variation in the transition stress and strain values was observed, which could be caused by several factors: the irregularities of the cross-section of the specimens, the presence of micro-cracks invisible to the naked eye, the irregular position of the fabric in the thickness, and the localization of the first cracks with respect to the position of the extensometer.

Characteristic values of each tested specimen and a representative stress-strain curve of each material system are provided in Appendix C.

Table 2.2: Properties of FRCM/SRG materials

Composite System		P_{max} [kN]	f_{ft} [MPa]	ϵ_{ft} [%]	f_{fu} [MPa]	ϵ_{fu} [%]	E_f [GPa]
B200-L0-F	AVG	1.14	253.6	0.0026	661.3	1.61	45.53
	SD	0.17	108.1	0.0021	48.1	0.81	6.51
G225-C1-F	AVG	1.79	520.3	0.0026	1014.9	2.18	26.07
	SD	0.10	68.5	0.0008	53.9	0.46	5.48
G250-L0-F	AVG	1.92	718.3	0.0036	1193.1	2.97	31.17
	SD	0.29	137.4	0.0002	170.3	0.56	4.12
C440-C2-F	AVG	10.46	392.8	0.0029	1394.1	1.64	63.50
	SD	1.46	51.4	0.0009	195.2	0.43	8.33
C130-C2-F	AVG	5.06	463.8	0.0010	1149.0	1.23	65.26
	SD	0.28	66.7	0.0000	64.0	0.22	15.95
S600-G0-S	AVG	5.72	460.2	0.0540	1381.4	1.23	89.49
	SD	0.56	174.9	0.0410	69.1	0.39	26.85
S600-L0-S	AVG	3.70	318.7	0.0081	861.8	1.39	46.27
	SD	0.68	89.0	0.0003	113.7	0.54	17.64
S1200-G0-S	AVG	6.50	388.3	0.0330	769.1	1.36	47.30
	SD	0.87	154.9	0.0190	71.3	0.67	19.70
S1200-L0-S	AVG	5.22	287.5	0.1010	618.0	1.05	37.56
	SD	0.57	80.5	0.0374	66.7	0.26	7.27

(a) FRCM

(b) SRG

Figure 2.5: FRCM and SRG failure modes

2.4 Effect of Fabric Architecture

The effect of fabric architecture was studied by comparing the S600 and S1200 SRG fabrics, because the two SRG fabrics are have identical cords, and differ only in the spacing between the cords and fabric architecture. The steel cords in both fabrics are made of five galvanized high-strength steel micro-cords, which are twisted together as shows in Fig. 2.6. The only difference between the two fabrics is the space between the cords, or their aerial density (i.e., the mass per unit

area). The aerial density of S600 and S1200 are 670 and 1200 g/m^2, respectively, as shown in the first column of Table 2.1.

Figure 2.6: SRG steel fabric

From the results in Table 2.2, the S600-G0-S outperforms the S1200-L0-S, and similarly, the S600-L0-S outperforms the S1200-L0-S in terms of ultimate strength and modulus of elasticity, even though the S1200-SRG has a larger fabric area. The reason is that both materials were tested using clevis-type grips with no pressure applied to the SRG coupons. The slippage was minimal in both SRG systems and the failure was splitting of mortar along the longitudinal axis, at the fabric interface (see Fig. 2.5). The failure in these specimens occurred whenever the shear stress at the fabric-mortar surface reached capacity. Thus, fabric-matrix fracture surface remained almost constant in both SRG coupons, whereas the fabric area (and consequently, the applied load at failure) changed. Moreover, the grid space of S600 fabric is larger than the S1200, which allows a better mortar penetration and a better matrix bond.

2.5 Effect of Number of Layers and Width

The effect of number of fabric layers on the mechanical performance of FRCM composites was studied on G225-C1-F system. Test specimens with one, two, four, and six fabrics (for the latter, three layers of two fabrics were jointed without mortar in between) were prepared. In addition, single layer fabric test specimens were prepared with two different widths (50 mm and 75 mm) to consider the effect of coupon width on mechanical behavior. Seven specimens of each configuration were prepared and tested. Specimen names follow the order XX-YY-ZZ, where XX defines the fabric type (G stands for G225 glass fabric) and number of fabric layers, YY is the specimen width in millimeters, and ZZ is the specimen counter. Test results for each group of specimens are given in Table 2.3. In the table, A_m is the matrix area (measured), A_f is the exact fabric area, computed as area of each yarn multiplied by the number of yarns in the coupon, f_{fc} is the cracking strength (based on A_f), P_{max} is the specimen peak axial force, f_{fu} is the ultimate tensile strength, E_f is the cracked modulus of elasticity, and ϵ_{fu} is the ultimate tensile strain. The fabric area calculated per AC434 (which is not in Table 2.1) is the equivalent thickness multiplied by the specimen width, which can be inaccurate because of the small specimen width with respect to the grid spacing. Thus, the exact area (yarn area, A_f) is considered in this section. Stress vs. strain curves for 50 mm specimens with one to six fabrics are illustrated in Fig. 2.7. The average of curves was calculated by first defining a set of horizontal data points that match the sampling frequency of the data acquisition system, and then interpolating the stress-strain values of each curve along the defined horizontal points.

Table 2.3: Effect of number of fabric layers on FRCM characteristics

Specimen	A_m [mm]	A_f [mm]	f_{fc} [MPa]	P_{max} [N]	f_{fu} [MPa]	E_f [GPa]	ε_{fu} [%]
G1-50-01	335.10		1025	1827.1	1036.1	32.1	1.6
G1-50-02	321.24		845	1671.8	948.0	26.2	1.8
G1-50-03	338.08		750	1793.7	1017.1	17.0	2.7
G1-50-04	289.65	1.8	550	1735.5	984.1	24.0	2.2
G1-50-05	340.24		580	1937.1	1098.5	30.5	2.2
G1-50-06	341.33		660	1717.0	973.6	30.7	1.9
G1-50-07	279.21		640	1908.3	1082.1	22.0	2.9
Mean	320.69		721.4	1798.6	1019.9	26.1	2.2
SD	23.91		154.9	91.7	52.0	5.1	0.4
G2-50-01	315.65		460	3548.1	1006.0	19.7	3.0
G2-50-02	315.92		450	3736.5	1059.4	18.7	3.2
G2-50-03	317.61		460	3736.6	1059.4	21.0	2.8
G2-50-04	328.62	3.5	410	3467.2	983.0	18.4	3.1
G2-50-05	400.44		350	3050.8	865.0	22.7	2.4
G2-50-06	414.90		430	3522.3	998.7	24.6	2.7
G2-50-07	407.58		415	3241.5	919.0	22.3	2.6
Mean	357.25		425	3471.9	984.4	21.0	2.8
SD	44.00		36	232.6	66.0	2.1	0.3
G4-50-01	560.86		350	6484.4	919.3	18.8	3.9
G4-50-02	482.10		285	6787.6	962.2	20.1	2.9
G4-50-03	573.23		360	6576.0	932.2	25.0	2.4
G4-50-04	500.99	7.1	345	5930.9	840.8	18.9	2.9
G4-50-05	640.33		375	5947.0	843.1	15.6	3.0
G4-50-06	738.09		370	5868.2	831.9	20.3	2.8
G4-50-07	659.25		300	5959.2	844.8	23.4	2.4
Mean	593.55		340	6221.9	882.0	20.3	2.9
SD	84.40		32	352.3	49.9	2.9	0.5
G6-50-01	640.96		246	9098.1	859.9	22.7	2.4
G6-50-02	649.38		-	9475.7	895.5	17.5	2.9
G6-50-03	605.26		176	9048.7	855.2	18.4	3.4
G6-50-04	639.48	10.6	220	8651.0	817.6	14.6	3.4
G6-50-05	637.95		130	8412.3	795.0	19.3	3.1
G6-50-06	675.42		205	7565.4	715.0	13.6	2.7
G6-50-07	665.99		183	9326.4	881.4	16.7	3.4
Mean	644.92		193	8796.8	831.4	17.5	3.0
SD	20.91		36	607.2	57.4	2.8	0.4

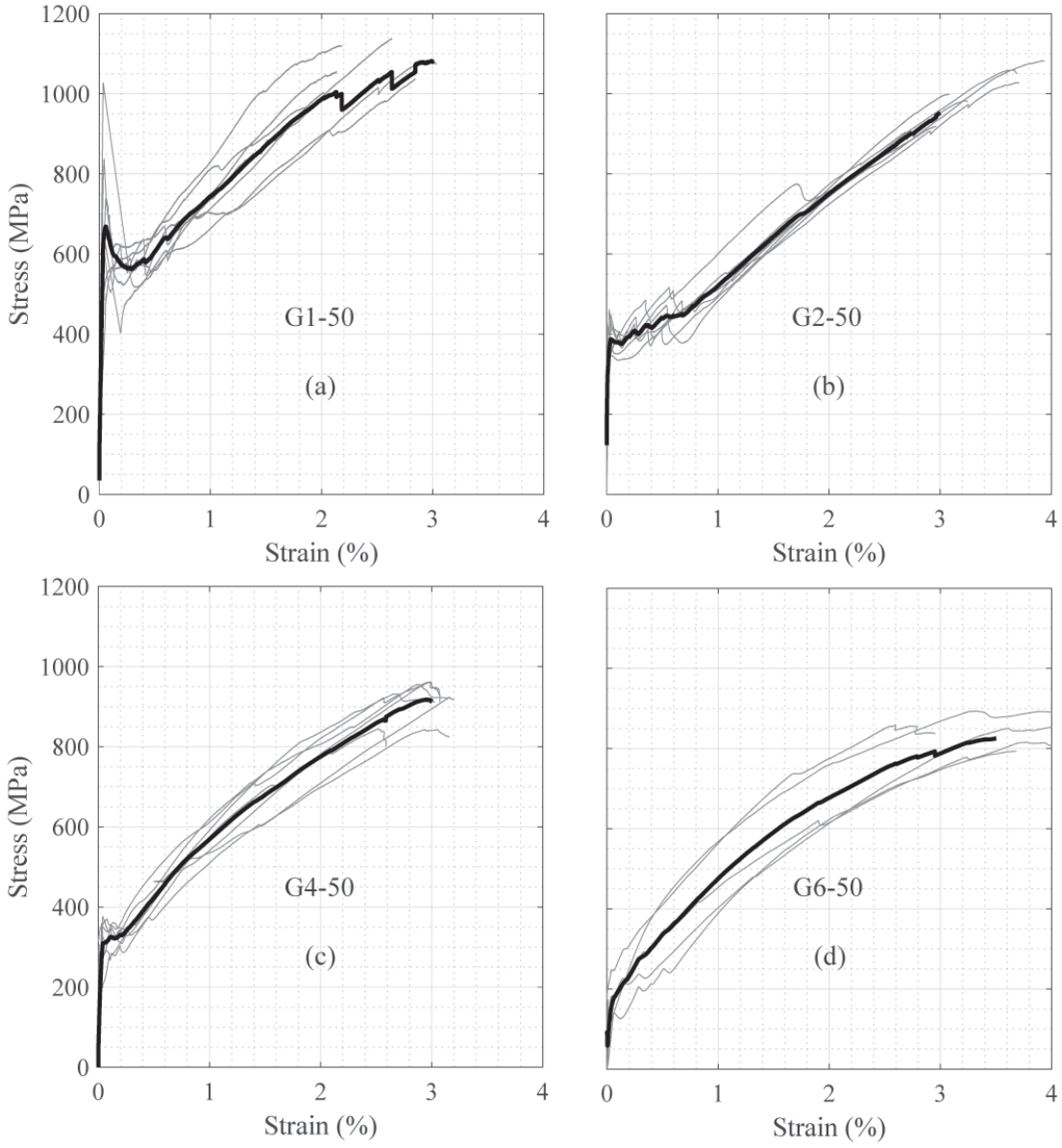

Figure 2.7: Tensile stress vs. strain: (a) 1 fabric layer; (b) two fabric layers; (c) four fabric layers; (d) six fabric layers

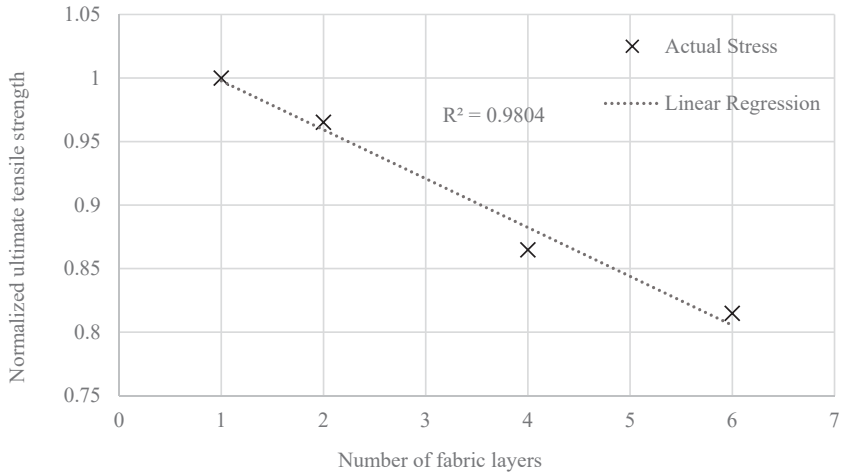

Figure 2.8: Effect of number of layers on ultimate tensile strength

Failure mode of all the specimens was slippage of the fabric(s) within the matrix, which resulted in development of multiple cracks in the matrix and eventually fabric debonding. The ultimate strength was also reduced by increasing the number of fabrics, and the relation was rather linear as shown in Fig. 2.9.

The comparison of single fabric GFRCM coupons with different widths is shown in Fig. 2.9. Increasing the specimen width decreased the ultimate strength, but had minimal effect on the modulus of elasticity and ultimate strain. Comparing the G1-50 and G1-75 specimens in Table 2.4 shows that by increasing the specimen width, the exact fabric area A_f was increased by 30%, while the matrix area A_m was enlarged by 82%. Therefore, following the earlier discussion, 75 mm specimens had a higher cracking strength f_{fc} because of larger matrix area. The average cracking load ($A_f f_{fc}$) for 75 mm and 50 mm specimens were 2.1 kN and 1.2 kN, respectively. The damage induced to the 75 mm specimens due to larger cracking

load (fracture energy) was significant, and the average ultimate tensile strength f_{fu} was less than the average cracking strength f_{fc}. Moreover, the shorter cracked portion of stress-strain diagram for these specimens made it impossible to calculate the elastic modulus based on the AC434 approach, since the $0.6f_{fu}$ was often outside of cracked portion. In this study, the cracked modulus of 75mm specimens was calculated as the best linear fit that represents the cracked portion of the stress vs. strain curves.

Table 2.4: Effect of specimen width on FRCM characteristics

Specimen	A_m [mm]	A_f [mm]	f_{fc} [MPa]	P_{max} [N]	f_{fu} [MPa]	E_f [GPa]	ε_{fu} [%]
G1-50-01	335.10	1.8	1025	1827.1	1036.1	32.1	1.6
G1-50-02	321.24		845	1671.8	948.0	26.2	1.8
G1-50-03	338.08		750	1793.7	1017.1	17.0	2.7
G1-50-04	289.65		550	1735.5	984.1	24.0	2.2
G1-50-05	340.24		580	1937.1	1098.5	30.5	2.2
G1-50-06	341.33		660	1717.0	973.6	30.7	1.9
G1-50-07	279.21		640	1908.3	1082.1	22.0	2.9
Mean	320.69		721.4	1798.6	1019.9	26.1	2.2
SD	23.91		154.9	91.7	52.0	5.1	0.4
G1-75-01	551.45	2.6	710	1878.1	710.0	16.8	3.0
G1-75-02	532.33		700	1891.9	715.2	31.6	2.3
G1-75-03	616.10		900	1645.3	622.0	20.5	2.3
G1-75-04	632.15		720	2306.6	872.0	31.7	1.3
G1-75-05	631.32		949	2137.1	807.9	28.4	1.7
G1-75-06	628.24		900	1965.4	743.0	17.1	2.7
G1-75-07	562.20		600	2568.1	970.8	27.5	2.8
Mean	598.60		833	2056.1	777.3	24.8	2.3
SD	40.81		102	208.6	78.9	6.4	0.6

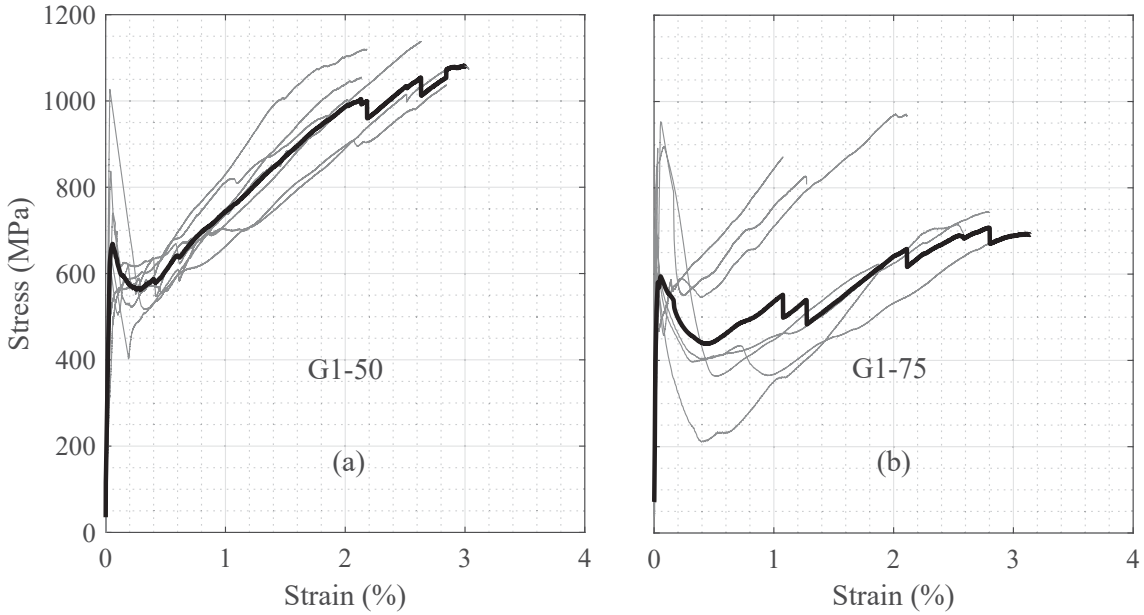

Figure 2.9: Tensile stress vs. strain: (a) 50 mm specimen; (b) 75 mm specimen

2.6 Test Setup and Acceptance Criteria

In addition to AC434 test method which uses clevis grips, another FRCM/SRG characterization method which combines the results of tensile tests on bare fabric specimens (performed with a clamping-grip setup, which applies lateral pressure in the load introduction areas) with single-lap shear bond tests was studied. The test method is according to the RILEM Technical Committee (TC) 250-CSM Composites for the Sustainable Strengthening of Masonry (de Felice et al., 2018).

To investigate the effects of test setup, three FRCM/SRG composites C130-C2-F, G250-L0-F, and S600-G0-S were tested in accordance with the RILEM test method, and their tensile strength, ultimate strain, and tensile modulus of elasticity were

obtained. The constituent materials of the investigated systems were introduced earlier in this chapter, in Section 2.1. Test results are discussed considering the different field applications of FRCM/SRG composites. The effect of test setup has been studied in collaboration with University of RomaTre.

2.6.1 Acceptance Method Based on Clamping-Grip Tensile Tests on Bare Fabrics and Single-Lap Shear Bond Test

Another method to determine the FRCM mechanical properties combining the results of clamping-grip tensile tests on bare fabric specimens and of single-lap shear bond tests (see Fig. 2.10) was developed within the RILEM TC 250-CSM. Shear bond tests provide the load transfer capacity between structural member (substrate) and externally bonded FRCM/SRG and the associated failure mode taking into account a broad range of possible failure modes. The strain and tensile modulus of elasticity corresponding to such ultimate stress are derived from tensile tests. A former version of this method, initially proposed by Ascione et al Ascione et al. (2015), included clamping-grip tensile tests on FRCM coupons, in accordance with a test protocol initially developed by RILEM TC 232-TDT for TRC materials 232-TDT (2016) and later specialized for FRCM/SRG systems. A round robin test performed within the RILEM TC 250-CSM (Caggegi et al., 2017; Carozzi et al., 2017; De Santis et al., 2017; Lignola et al., 2017) showed that the results of tensile tests on coupons may be affected by manufacturing and curing, pre-existing damage, and setup details, due to the brittle nature of the matrix. More specifically, both the crack pattern and the stress drops associated to crack occurrence

may vary widely from specimen to specimen and from laboratory to laboratory. Pre-existing damage or premature cracking may lead to underestimate the tensile modulus of elasticity of the uncracked FRCM/SRG and the stress and strain of the first crack (transition point). Finally, the tensile modulus of elasticity of cracked specimens and the ultimate tensile stress and strain may vary depending on the pressure applied in the gripping areas. As a consequence, the acceptance parameters may in their turn result particularly sensitive to these aspects, especially for some FRCM systems, as, for instance, those whose acceptance stress falls in the first (uncracked) or second (crack development) stages of the response behavior, which raises some doubts on the repeatability of the tests and the robustness of the method.

Furthermore, the stress state and the crack pattern of FRCM/SRG systems in structural applications may differ from those experienced by FRCM/SRG coupons in tensile tests, due to the different boundary conditions (e.g., longer bond length, presence of the substrate which may constrain strain and cracking on its side or promote cracking in the externally bonded FRCM/SRG if cracks were present in the substrate). Therefore, the ultimate strain and tensile modulus of elasticity in this study were determined through clamping-grip tensile tests on bare fabric specimens, and not on FRCM/SRG coupons, in order to improve the robustness of the method and the representativeness of the obtained parameters. This choice is also in accordance with the advice of the Italian standardization board set within the National Research Council (CNR) for the development of qualification guidelines for FRCM/SRG composites. The ends of the fabric specimens are to be clamped in the wedges of a testing machine with sufficient lateral pressure that prevents slip-

page in the load introduction areas to achieve the rupture of the fibers. In this way, the scatter associated to the ultimate strain is expected to reduce when passing from FRCM/SRG coupons to bare fabric specimens. However, the variability of the ultimate strength, which is obtained from single-lap shear bond tests, remains unchanged.

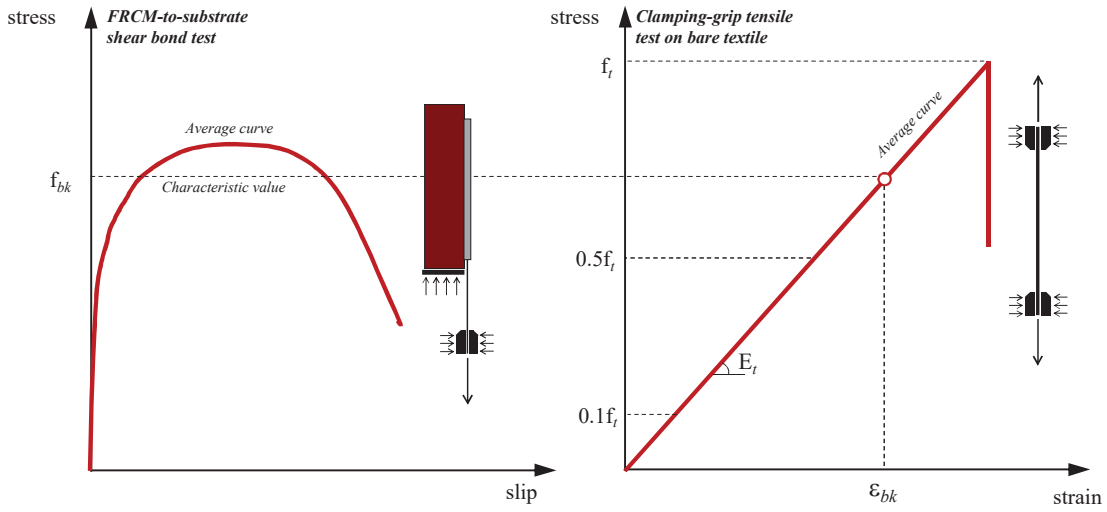

Figure 2.10: Schematic results of single-lap shear bond tests and of clamping-grip tensile tests on bare fabric specimens.

The parameters resulting from this acceptance method are:

(i) characteristic stress associated with the shear bond failure (f_{bk}), derived as the 5% fractile of the peak axial stresses attained in shear bond tests: $f_{bk} = \overline{fb} - K_n \Delta_b$;

(ii) tensile modulus of elasticity of the fabric (E_t), computed between $0.1 f_t$ and $0.5 f_t$ (CEN European Committee for Standardization, 1995);

(iii) characteristic strain associated with the shear bond failure (ϵ_{bk}), computed as $\epsilon_{bk} = f_{bk}/E_t$.

Where $\overline{fb}$ is the mean value of the peak axial stress (computed as the maximum

load attained in the test divided by the fabric cross-sectional area), K_n is statistical coefficient that, according to Annex D of Eurocode 0 (CEN European Committee for Standardization, 2002), depends on the number of specimens, Δ_b is the standard deviation of the peak axial stress values from the tests, ft is the tensile strength of the fabric, and, finally, E_t is its mean tensile elastic modulus.

For design purposes, in accordance with Eurocode 0, the characteristic stress and strain are divided by a partial coefficient (γ), whereas the tensile elastic modulus is the average value of experimental test results ($\overline{E_t}$). Thus, the following design values are derived:

(i) design ultimate tensile strength $f_{bd} = f_{bk}/\gamma$;

(ii) design ultimate tensile strain$\epsilon_{bd} = \epsilon_{bk}/\gamma$;

(iii) design tensile modulus of elasticity $E_{td} = \overline{E_t}$.

The FRCM/SRG systems is assumed to be linear elastic to failure and the effective stress value (f_{fe}) associated with an effective strain level (ϵ_{fe}) is determined as $f_{fe} = \epsilon_{fe}E_t$. Finally, based on the type of application (flexural, shear, etc.), the boundary conditions experienced by FRCM/SRG applied to structural members may vary with respect to laboratory tests. More specifically, the occurrence of the detachment at an intermediate section of the reinforcement (with two FRCM/SRG-to-substrate interfaces involved in the load transfer mechanism) rather than at the end of the FRCM/SRG overlay, and the larger bond area (entailing a higher friction contribution in case of fabric slippage), may lead the composite to attain larger strains. The strain provided by the acceptance method may therefore underestimate the strain in the reinforcement at failure. In order to take into account this issue, the design ultimate tensile strain can be amplified by a coefficient, which

should be calibrated on experimental basis for the different applications.

From a mechanical point of view, this test method aims at providing FRCM mechanical properties accounting for the weakest substrate-composite load transfer mechanism amongst all the possible ones, thus including not only the fabric slippage or tensile rupture, but also the cohesive debonding within the substrate, and the detachment either at the composite-substrate interface or at the fabric-matrix one. With this purpose, the stress needs to be derived from single-lap shear bond tests. As for the strain and the tensile modulus of elasticity, the choice of performing clamping-grip tests on bare fabric specimens (and not on FRCM coupons) not only reduces the scatter, but also it allows for the cracking and slippage which may take place in structural applications to be taken into account.

2.6.2 Test Setup

Clamping-grip tensile tests on bare fabric specimens

Direct tensile tests on bare fabrics (Fig. 2.11a) were carried out on specimens having a length of 600 mm and a (nominal) width equal to a multiple of the grid spacing, namely 50 mm for the C130 carbon fabric (the strip included 5 yarns), 45 mm for the G250 glass fabric (3 yarns) and 50.8 mm for the S600 steel fabric (8 cords). Fabric specimens were clamped in the hydraulic wedges of the testing machine and their ends were provided with 90 mm x 50 mm 13 mm (length x width x thickness) aluminum tabs to ensure a uniform stress distribution and avoid local stress/damage concentrations in the gripping areas. Axial load was applied in displacement control at 0.25 mm/min rate and recorded by an integrated load cell. Strains were recorded by an extensometer over a 50 mm gauge length.

Clamping-grip tensile tests on FRCM/SRG coupons

Clamping-grip tensile tests were carried out on FRCM/SRG coupons (Fig. 2.11b) with 600 mm length, 50 mm width and 10 mm thickness. Specimens were manufactured individually in Plexiglas molds and cured for 28 days at minimum 95% relative humidity. Coupons were clamped in the wedges of the testing machine, which applied a lateral pressure to prevent slippage and attain the rupture of the fabric (232-TDT, 2016). The gripping areas were wrapped with two layers of GFRP to ensure a proper load transfer and prevent damage/spalling. Axial load was applied in displacement control at 0.3 mm/min rate and recorded by an integrated load cell. Strains were recorded by an extensometer with 50 mm gauge length and by two linear potentiometers placed on the mortar by means of metallic plates over a gauge length of 200 mm. Since the reliability of the transducers applied to the matrix relies upon the location of cracks, Digital Image Correlation (DIC) was also used to validate strain data (see (Tekieli et al., 2017) for details).

Single lap shear bond tests

Single-lap shear bond tests (Fig. 2.11c) were carried out on masonry units built using five 55 mm thick clay bricks with 10 mm mortar joints. FRCM/SRG systems were applied to one side of the masonry substrate. The bonded area was 50 mm wide and 260 mm long. Based on previous experimental studies, such bond length was chosen to reach the matrix-substrate and fabric-matrix bond capacities, i.e., the chosen lengths were longer than the effective bond length, beyond which a quasi-stabilization of the maximum load is observed (de Felice et al., 2018).
Tests were carried out on the same universal test frame used for the tensile tests,

with a single-lap push-pull scheme. The specimens were placed in a steel frame clamped from above, whereas the unbonded portion of the bare fabric was pulled from below. The load was applied under displacement control at 0.18 mm/min rate. The relative displacement (slip) was recorded at the loaded end of the bonded area with two linear displacement transducers (LVDTs) and validated by DIC (Tekieli et al., 2017).

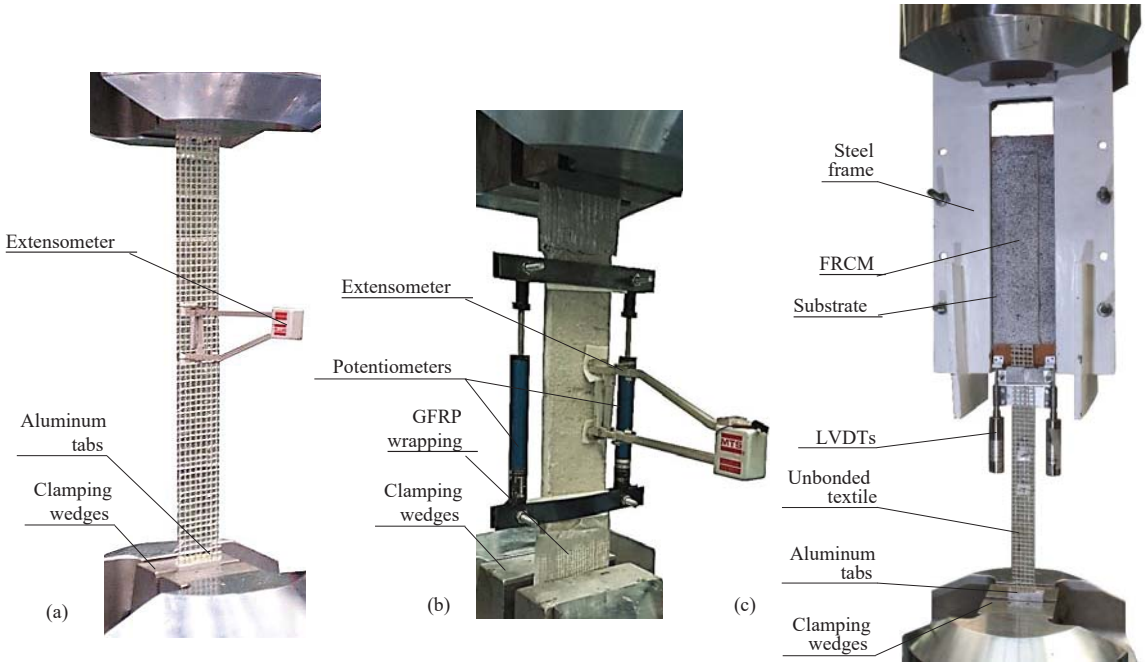

Figure 2.11: Test setups for clamping-grip tensile tests on bare fabric specimens (a); FRCM coupons (b); and single-lap shear bond (c)

2.6.3 Test Results

Test results are presented in terms of stress vs. slip (for shear bond tests) and stress vs. strain (for tensile tests) response curves in 2.12 to 2.14, stresses being computed based on the fabric cross-sectional area, which rendered the values

of stresses independent from the thickness of the matrix and from the width of the specimen. Five specimens were tested for each test type (clamping-grip tensile tests on fabric and on FRCM/SRG coupons, clevis-grip tensile test on FRCM coupons and shear bond tests). The 5% fractile coefficient is $K_n = 2.33$ for 5 specimens. In each graph, the curves of all the specimens are plotted and, for each set of tests, the average curve is also shown with a thicker line.

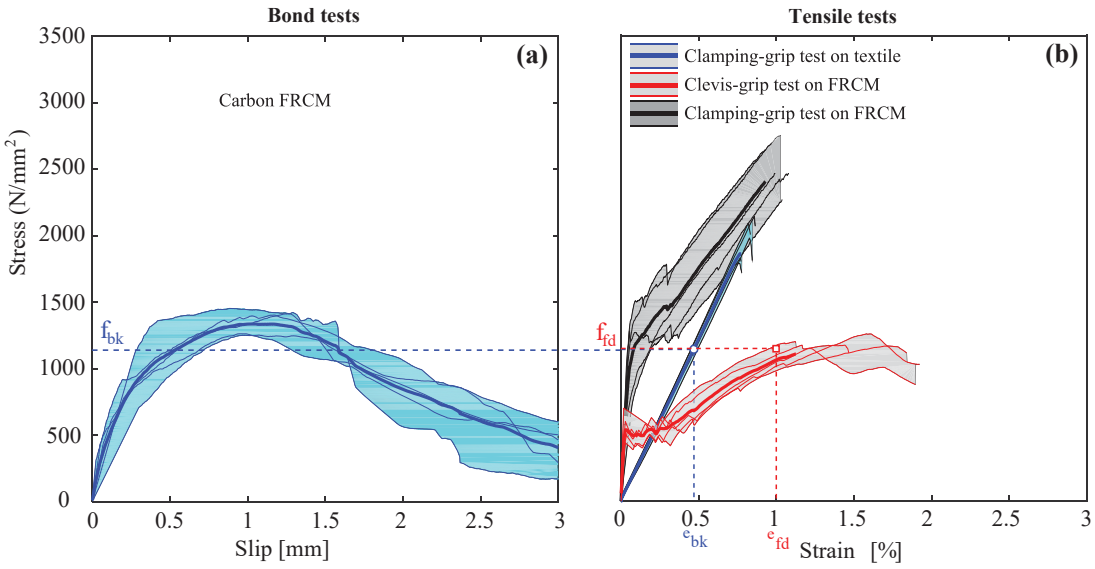

Figure 2.12: Response curves of shear bond (a) and tensile (b) tests and identification of acceptance parameters for carbon system.

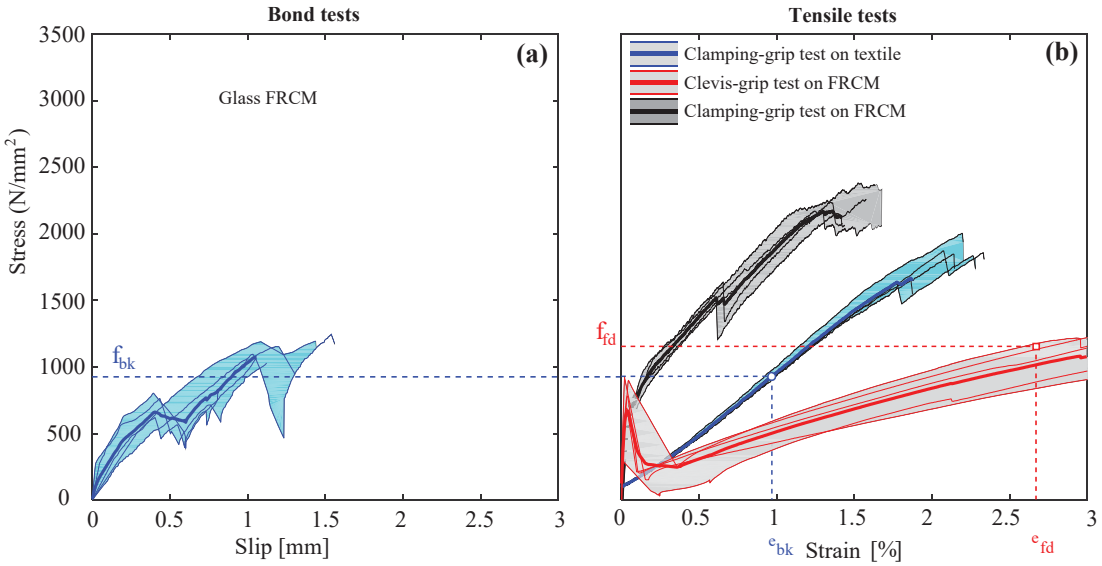

Figure 2.13: Response curves of shear bond (a) and tensile (b) tests and identification of acceptance parameters for glas system.

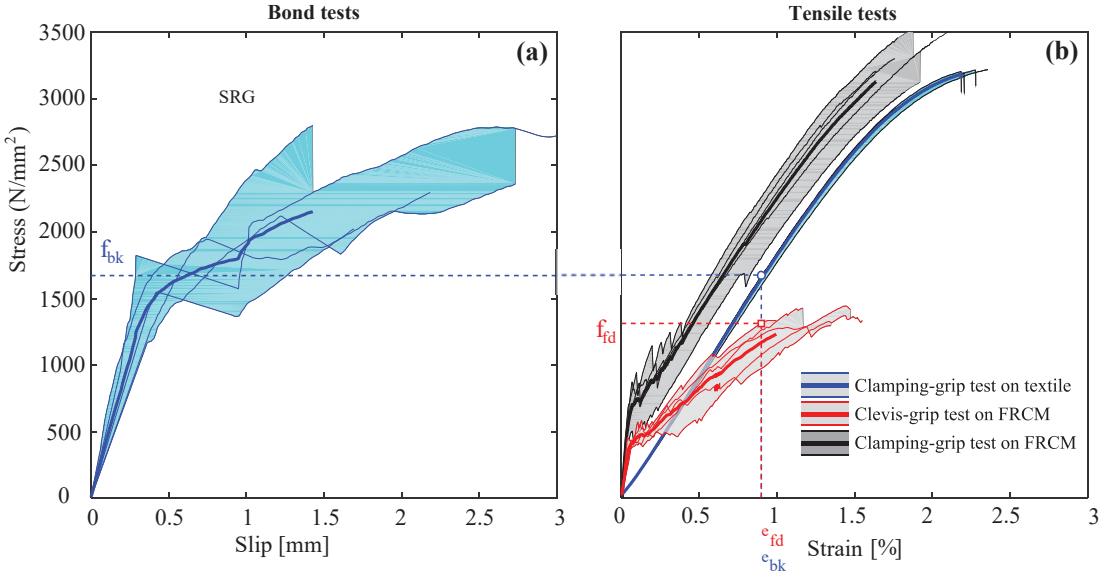

Figure 2.14: Response curves of shear bond (a) and tensile (b) tests and identification of acceptance parameters for SRG system.

Clamping-grip tensile tests on bare fabric specimens

The experimental results (tensile strength, ultimate strain and tensile modulus of elasticity) of tensile tests on bare fabric specimens with clamping grip are collected in Table 2.5, in which Avg and SD denote average and standard deviation, respectively. C130 carbon Fig. 2.12b and G250 glass Fig. 2.13b fabrics exhibited a linear behavior to failure, which was characterized by the progressive rupture of the filaments, whereas the S600 steel fabric Fig. 2.14b showed a loss of linearity after 60% of the peak stress and failed by the nearly simultaneous rupture of the cords. It is worth noting that the ultimate stress attained by the carbon bare fabric specimens (1964 N/mm^2) is significantly lower than that of the individual filament (4800 N/mm^2, according to the technical data sheet) due to the unavoidable unevenness in the stress distribution among the fiber yarns in the tests on fabric strips.

Table 2.5: Results of clamping-grip tensile tests on bare textile specimens

Material system		Tensile strength (f_t) [N/mm^2]	Ultimate strain [%]	Tensile modulus of elasticity (E_t) [kN/mm^2]
C130-C2-F	Avg	1964	0.807	242
	SD	155.8	0.040	9.0
G250-L0-F	Avg	1842	1.968	95
	SD	120.8	0.143	3.5
S600-G0-S	Avg	3201	2.244	186
	SD	14.1	0.073	3.4

Clamping-grip tensile tests on FRCM coupons

The FRCM coupons tested with clamping grip exhibited three response stages (Figs. 2.12b to 2.14b). After the first uncracked phase, perpendicular cracks appeared on the specimens, which opened up as the fabric deformed. In the last stage, the response curve of the composite was parallel but higher than that of the bare fabric, showing the stiffening effect of the (cracked) matrix. As shown in Table 2.6, the tensile stresses were 5 to 30% higher than those of the bare fabrics, due to the stress redistributing effect of the mortar. Apart from two C130-C2-F specimens in which the carbon fabric slipped within the matrix (Fig. 2.15a), failure occurred by tensile rupture of the fabric. In all cases, the maximum stress was higher than that attained in clevis-grip tensile tests. The coated yarns of the G250 fabric exhibited a telescopic failure, which resulted in the formation of a wide crack at the fractured plane (Fig. 2.15b). Finally, in S600-G0-S coupons, the steel cords recoiled after rupture, which spalled the mortar and formed longitudinal cracks aligned with and parallel to the fabric (Fig. 2.15c). It should be noted that the scatter of the parameters obtained from the clamping-grip tensile tests on FRCM/SRG coupons is relatively higher than that of the results of the tensile tests on bare fabric specimens. In specific respect of the outcomes directly related to the acceptance parameters, the coefficient of variation (standard deviation divided by average value) of the stress of the transition point ranges between 5% and 22%, that of the strain between 16% and 56% and, finally, those of the tensile moduli of elasticity between 14% and 37% (uncracked) and between 2% and 6%. On the contrary, the tensile modulus of elasticity of the bare fabric exhibited a coefficient of variation of 2 to

3%, which should ensure more robust acceptance parameters independently from manufacturing and curing, possible pre-existing damage, and setup details.

Table 2.6: Results of clamping-grip tensile tests on coupon specimens

Material system		Transition point		Ultimate point		Tensile modulus of elasticity		Failure mode[(a)]
		Stress [N/mm²]	Strain [%]	Stress [N/mm²]	Strain [%]	Uncracked [kN/mm²]	Cracked [kN/mm²]	
C130-C2-F	Avg	1263	0.112	2587	1.072	2027	155	FR/SL
	SD	192.9	0.063	152.1	0.068	754.0	9.1	
G250-L0-F	Avg	693	0.057	2239	1.425	1416	131	FR
	SD	38.8	0.009	105.1	0.170	201.1	7.8	
S600-G0-S	Avg	784	0.091	3364	1.899	1664	186	FR
	SD	172.9	0.021	164.9	0.134	495.9	3.4	

[(a)] FR: fabric rupture; SL:slippage of fabric within the matrix.

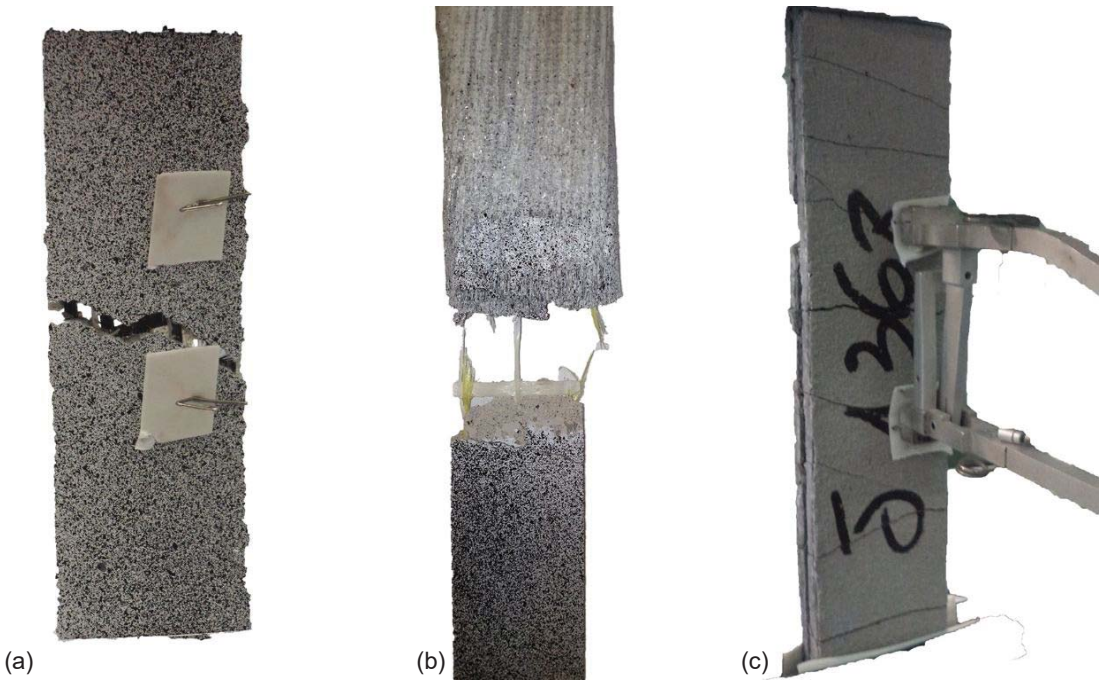

Figure 2.15: Failure modes of C130-C2-F (a), G250-C1-F (b), and S600-G0-S (c) coupons subjected to clamping-grip tensile tests.

Single-lap shear bond tests

In shear bond tests, whose results are collected in Table 2.7, the C130-C2-F system failed by slippage of the fabric within the matrix (Fig. 2.16a), indicating a relatively low adhesion between the carbon fabric and the matrix. In the G250-L0-F system, the fabric broke out of the bonded area (Fig. 2.16b), suggesting that the tensile strength of the fibers was lower than the bond strength at fabric-matrix and matrix-substrate. Finally, the S600-G0-S system exhibited a mixed failure mode in which detachment occurred at the matrix-to-substrate interface (Fig. 2.16c), with the brick surface locally peeled off too. The coefficient of variation of the peak ax-

ial stress, which is directly reflected in the ultimate stress (this latter being a 5% fractile value), ranges between 7 and 14%.

Table 2.7: Results of single-lap shear bond test

FRCM system		Peak axial stress [N/mm^2]	Peak slip [mm]	Failure mode
C130-C2-F	Avg	1360	1.07	SL
	SD	94.1	0.16	
G250-L0-F	Avg	1137	1.27	FR
	SD	90.8	0.21	
S600-G0-S	Avg	2455	2.14	DEB
	SD	335.7	0.55	

[(a)] SL: slippage of fabric within the matrix; FR: fiber rupture; DEB: debonding.

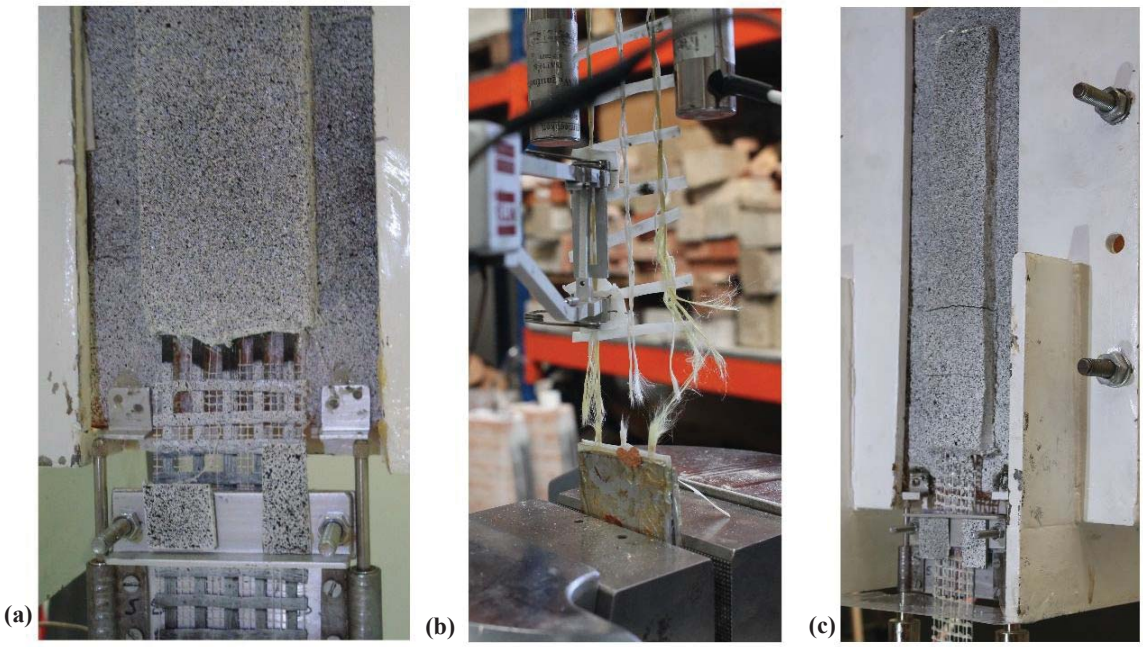

Figure 2.16: Failure modes of C130-C2-F (a), G250-C1-F (b), and S600-G0-S (c) in shear bond test.

2.6.4 Comparisons

The two acceptance methods applied in this work exhibit fundamental differences, due to the different test setup. The AC434 test method was developed anticipating the application of FRCM/SRG composites to concrete substrates, whereas the method developed within RILEM was mainly intended for application on clay brick or stone masonry. Accordingly, different material systems have been tailored to suit different applications. For concrete substrates, cement-based mortars (possibly polymer modified or reinforced with short fibers) are mostly used. For masonry substrates, lime-based mortars, which accommodate higher deformation are mostly used, which exhibit different failure modes. Test methods and acceptance criteria have been conceived to account for these features. Thus, their results are

not necessarily expected to coincide. Finally, acceptance parameters are to be used within different design frameworks (defined by U.S. building codes or Eurocodes) with different design philosophies.

For all these reasons, a direct correlation cannot be established between the two test methods. However, some comparisons can be made among the acceptance parameters provided by the two methods within the present work, as shown in Table 2.8. First, the same ultimate strength was obtained for C130-C2-F system, whose effectiveness relies on the fabric-to matrix bond, which is well investigated by both the clevis-grip tensile test and by the shear bond test. The average ultimate strengths (as well as the corresponding standard deviations) also resulted comparable for G250-L0-F system, despite the observed failure modes were not the same. Nevertheless, the different formulations adopted for the calculation of the design parameters (i.e., the different percentiles associated with the characteristic strength values) led to a mismatch of 24%. Finally, for the S600-G0-S system, shear bond tests provided a 22% higher ultimate strength (associated with the detachment from the substrate) than that obtained with the clevis grip tensile test (in which failure occurred by splitting of mortar).

For both C130-C2-F and G250-L0-F systems, the clevis-grip tensile test on FRCM coupons provided a higher design strain value $\epsilon_{bd}/\epsilon_{bk} = 2.13to2.78/$ and a lower modulus of elasticity ($E_{fd}/E_t = 0.27to0.33$) than the clamping-grip tensile test on fabric strips combined with the shear bond test. In AC434 method, the fabric slippage in the gripping areas allowed for much larger elongations and the stiffness of the cracked FRCM resulted much lower than that obtained when slippage was prevented. Such mismatch in the tensile modulus of elasticity was found also for

the S600-G0-S system, due to the different boundary conditions. However, due to the limited slippage in clevis-grip tensile tests, the strain values from both methods coincide. Finally, differences were found in the determination of the transition point, with the clamping-grip method providing a higher stress (in two systems) and a larger strain (in all systems) than the clevis-grip method. Modulus of elasticity of the uncracked FRCM/SRG with the clevis-grip method was higher than the clamping-grip in two cases. The transition point and uncracked stiffness depend on the cross-section area, the tensile strength, and the Young's modulus of the mortar. Thus, it should be independent of the test configuration.

Table 2.8: Comparison of characterization results

FRCM System	Clevis-grip tensile tests on FRCM coupons			Clamping-grip tensile tests on textiles and shear bond tests			Comparisons		
	f_{fd} [N/mm^2]	ε_{fd} [%]	E_{fd} [kN/mm^2]	f_{bk} [N/mm^2]	ε_{bk} [%]	E_t [kN/mm^2]	$\frac{f_{fd}}{f_{bk}}$	$\frac{\varepsilon_{fd}}{\varepsilon_{bk}}$	$\frac{E_{fd}}{E_t}$
C130-C2-F	1147	1.00	66	1141	0.47	242	1.01	2.13	0.27
G250-L0-F	1151	2.67	31	926	0.97	95	1.24	2.75	0.33
S600-G0-S	1309	0.90	89	1673	0.90	186	0.78	1.00	0.48

2.7 Conclusions

Material characteristics of FRCM and SRG composites was discussed in this chapter. FRCM/SRG materials were tested in accordance with AC434 test meth-

ods.

The failure mechanism of FRCM and SRG materials were distinctly different. The FRCM materials failed due to fabric slippage, while the SRG failed due to mortar splitting. Thus, the bond performance at fabric-matrix interface governed the FRCM tensile properties, which depend on mortar performance, fabric architecture, and presence of polymeric coating on fabrics. SRG characteristics, on the other hand, depended primarily on the matrix performance, because the fracture surface was formed in the matrix due to shear forces. Increasing the fabric area which increases the shear stress in the matrix significantly deteriorated the overall performance of tested SRG materials.

Performance of FRCM reduced by increasing the number of fabric layers. Therefore, material properties based on tests conducted on one-layer specimens are not necessarily representative of multiple-layer configurations.

Two different acceptance methods were compared to characterize FRCM/SRG materials.

For the composites investigated in this study, the ultimate strength values provided by the two methods were comparable, and coincided for the carbon FRCM, which failed by fabric slippage also in the bond test. On the other hand, the different boundary conditions applied in tensile tests generally led to a lower tensile modulus of elasticity and to a higher ultimate strain obtained from the clevis-grip test with respect to the clamping-grip one, except from the SRG, in which the roughness of the cords ensured a good interlocking within the matrix and limiting slippage also in the clevis-grip tensile test.

It should be noted that the acceptance parameters provided by the two approaches

are not necessarily expected to coincide. The FRCM material characteristics represent the fundamental information in the design of externally bonded reinforcements, but the design framework also includes the percentiles associated with the characteristic strength values, the partial coefficients related to material properties or structural capacity (strength reduction factors) and loading demand (coefficient applied to existing actions), and the tuning coefficients (calibrated to make theoretical values match experimental results). Accordingly, further work should be extended to using the acceptance parameters obtained per each method and analytically predicting the performance of structural members with the aim of comparing/contrasting the analytical results with the experimental tests on the structural members.

Chapter 3

Structural Performance

This chapter regards the structural performance of FRCM/SRG strengthened RC beams in bending. Three FRCM and two SRG systems were used in the study. The FRCM and SRG materials systems were introduced in Chapter 2, and their mechanical properties according to AC434 test method was determined. FRCM/SRG material properties were used to analytically calculate yielding and ultimate capacities of the FRCM/SRG strengthened RC beams according to ACI 549.4R-13. Strengthened RC beams were experimentally tested under monotonic loading. Effect of RC beam geometry was investigated.

3.1 Materials

Material properties of FRCM/SRG and RC beams were experimentally determined. Three FRCM (C130-C2-F, C440-C2-F, and G225-C1-F) and two SRG (S600-G0-S and S1200-G0-S) systems were used in this study, which were introduced in Section 2.1 and characterized in Section 2.3 of Chapter 2. Table 3.1 provides ma-

terial properties of concrete and steel rebars used in the RC beams. Compressive strength of concrete cylinders of 100 mm diameter at 28 days was obtained according to ASTM ASTM C39/C39M-18 (2018). Yield strength and elastic modulus of the steel rebars were determined as for ASTM A370-17a ASTM A370-17a (2017).

Table 3.1: Concrete and steel rebar characteristics

Material	Test	Mean	CoV (%)
Concrete	Compressive Strength	40.4 MPa	5.0
Steel Rebar	Yield Strength	501.2 MPa	3.6
	Young's Modulus	193 GPa	3.2

3.2 RC Beams

RC beams were designed and cast per ACI 318 code requirements (American Concrete Institute (ACI), 2014). Beams had a total and effective length of 1829 mm and 1524 mm, respectively, and the concentrated load was applied at mid-span. Three #3 (ϕ9.5 mm) longitudinal rebars were used in tension and two #3 (ϕ9.5 mm) rebars in compression. The beams were designed to be under-reinforced while met the minimum required steel reinforcement. Shear reinforcement #2 (ϕ6.3 mm) stirrups with 127 mm spacing were used to prevent failure due to shear as shown in Figure 3.1. Specimens follow the name order X-Y-Z, where X is the applied load type (S for Static), Y is fabric type, as mentioned in the Chapter 2 and Z denotes the number of fabric layers.

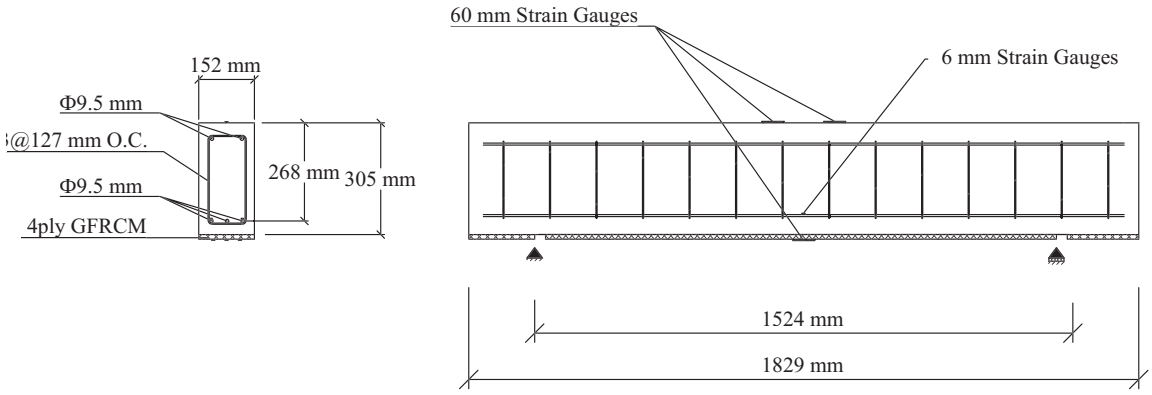

Figure 3.1: RC beam details and dimensions

3.3 FRCM/SRG Reinforcement

Analysis of the FRCM/SRG strengthened beams was according to ACI 549.4R-13. In the analysis, assumptions were that (a) plane sections remain plane after loading; (b) the bond between the FRCM/SRG and the substrate remains effective; (c) the maximum compressive strain in concrete is 0.003; and (d) FRCM/SRG has a linear elastic behavior up to failure.

The design tensile stress in the FRCM/SRG is equal to $E_f \epsilon_f$, where E_f is the FRCM/SRG cracked modulus of elasticity and ϵ_f is the ultimate tensile strength. The values of tensile strength and ultimate strain for design purposes were reduced to the average value minus one standard deviation to meet the ACI 549.4R-13 design guideline. Moreover, the design tensile strain in FRCM/SRG is limited to 0.012 mm/mm per ACI 549.4R-13.

FRCM/SRG and steel rebar contributions were expressed in the form of stiffness-dependent parameters, κ^f and κ^s, respectively:

$$\kappa^s = \rho_s E_s \tag{3.1}$$

$$\kappa^f = \rho_f E_f \tag{3.2}$$

In which E_f and E_s are the Young's moduli of the FRCM/SRG and steel, respectively; ρ_f and ρ_s are the FRCM/SRG and steel reinforcement ratios equal to A_f/bh and A_s/bd, respectively; h is the overall height of RC beams; d is the RC beam effective depth; and b is the width of RC beams.

The dimensionless reinforcement ratio β^f is defined as follows: κ^f over κ^s.

$$\beta^f = \frac{\kappa^f}{\kappa^s} = \frac{\rho_f E_f}{\rho_s E_s} \tag{3.3}$$

β^f is a practical form of expressing the relative stiffness provided by the FRCM/SRG reinforcement in an RC beam. Table 3.2 provides number of fabric layers and reinforcement ratio for each strengthening system.

Numerical capacities of RC beams were determined from section analysis. Appendix **??** provides a sample of cross section analysis calculations. The analytical yielding and ultimate capacities of each configuration are given in Table 3.3. The increase in capacity provided by FRCM/SRG with respect to the unstrengthened beams were also calculated and given in the same table. Lastly, the predicted controlling failure modes were determined. AC434 defines five failure types for the FRCM/SRG strengthened beams, which include crushing of concrete in compression before yielding of steel, yielding of steel followed by concrete crushing, delamination of concrete cover, debonding of the FRCM from the concrete substrate

and tensile rupture of FRCM/SRG. In section analysis, the failure was defined as reaching the design strain in the material. Therefore among concrete in compression, steel rebars in tension and FRCM/SRG in tension, the material that reached its design capacity first governed the controlling failure mode. From the analysis, the steel rebars was yielded in all beams at the ultimate capacity. The failure mode of control beams was concrete crushing. Failure mode of the strengthened beams was failure in the FRCM/SRG, which in reality can be debonding at matrix-substrate interface, delamination at matrix-fabric interface, tensile rupture of FRCM/SRG fabric, or a combination of these. The section analysis conducted herein according to ACI 549.4R-13 could not predict the specific failure mode when the failure occurs in the FRCM/SRG. Controlling failure modes are given for each test configuration in the last column of Table 3.3.

Table 3.2: FRCM/SRG reinforcement comparison

Fabric Type	**Specimen ID**	**Number of Layers**	κ_S [MPa]	κ_F [MPa]	β^f [%]
–	S-Con	–	1089	–	–
	S-C130-2P	2	1089	19	1.74
Carbon	S-C440-1P	1	1089	34	3.12
	S-C440-2P	2	1089	67	6.15
Glass	S-G225-4P	4	1089	12	1.11
Steel	S-S600-1P	1	1089	25	2.26
	S-S1200-1P	1	1089	26	2.39

Table 3.3: Reinforcement ratio and analytical capacity increase

Specimen ID	Number of Ply	β^f [%]	Yield Capacity [kN]	Yield Increase [%]	Ultimate Capacity [kN]	Ultimate Increase [%]	Failure Mode
S-Con	–	–	68	–	84.5	–	Conc.
S-C130-2P	2	1.74	70.1	3.1	96.5	14.2	FRCM
S-C440-1P	1	3.12	71.6	5.2	104.4	23.5	FRCM
S-C440-2P	2	6.15	75.2	10.6	120.8	42.9	FRCM
S-G225-4P	4	1.11	69	1.5	90.7	7.3	FRCM
S-S600-1P	1	2.26	70.8	4.1	100.98	19.5	SRG
S-S1200-1P	1	2.39	70.9	4.2	101.77	20.4	SRG

3.4 Test Setup

Beams were tested in three point bending configuration with purpose-built hinge supports for effective span length, as shown in Fig. 3.2. Test frame was a 250 kN servohydraulic actuator mounted in a steel test frame. FRCM/SRG strips 152 mm in width were applied on the beam soffit throughout its length and cut immediately before the supports to prevent anchoring, as shown in Fig. 3.2. Strain values were monitored by a total of seven strain gauges: two 60 mm strain gauges applied on concrete in compression, three 60 mm strain gauges on FRCM material in tension and two 6 mm strain gauges on steel rebars. Strain gauges on rebars and concrete were placed at midspan. For FRCM, one gauge was placed at midspan

and the other two were attached to the right and left of the middle one 50 mm apart

Three Linear Variable Differential Transformers (LVDTs) were used to measure the defelection. One LVDT was placed at the midspan and the other two were located at the supports to account for settlement.

Test were conducted in displacement control mode at rate of 0.0875 mm/sec with four cycles of partial loading and unloading. The author acknowledges that more structural tests could have been performed to give statistical significance to the FRCM-strengthened RC beams tested under monotonic loading. However, this study includes a limited number of structural tests due to the costly nature of full-scale structural tests.

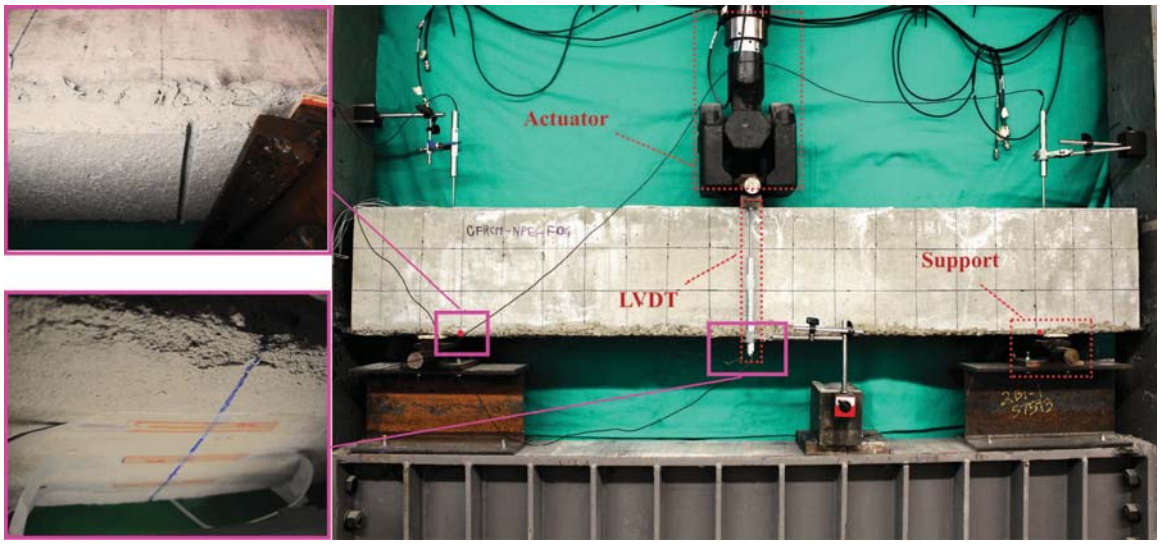

Figure 3.2: Strengthened RC beam test setup

3.5 Experimental Results

RC beams were tested under monotonic loading. The strengthening configuration is according to Table 3.2: 2 ply C130-C2-F FRCM, 1 and 2 ply C440-C2-F, 4 ply G225-C1-F, 1 ply S600-G0-S, and 1 ply S1200-G0-S. One beam was tested unstrengthened as the control specimen.

Applied load vs. mid-span deflection curves for carbon, glass, and steel reinforced specimens are shown in Figs. 3.3 to 3.5 Total area of FRCM/SRG is significantly small compared to the reinforcing steel. Thus, up to cracking load, no significant change in behavior between strengthened and control specimens was observed. The effect of FRCM/SRG became evident after cracks were developed and the strengthened specimens showed a higher post-cracking stiffness compared to the unstrengthened beam.

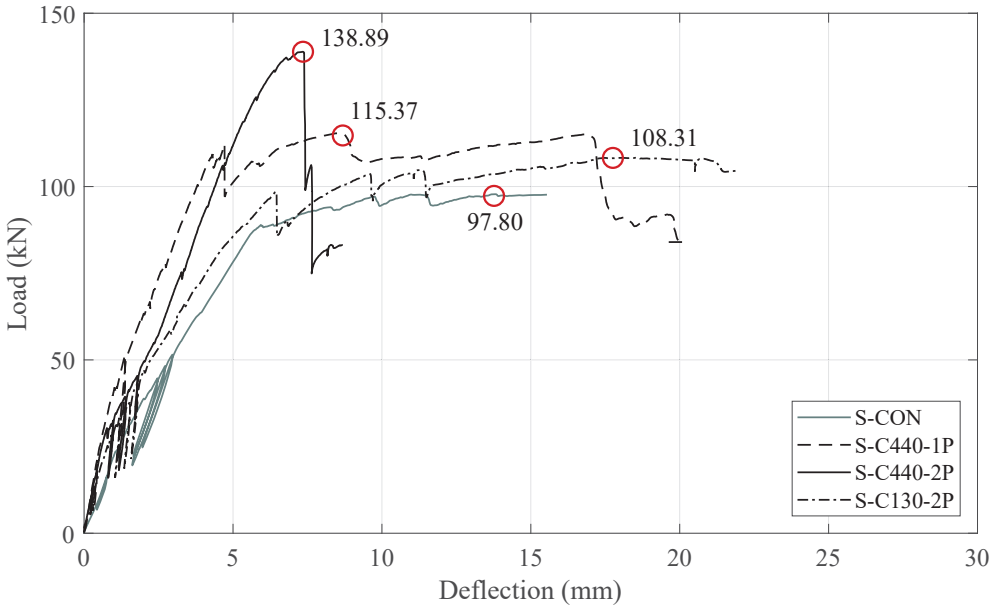

Figure 3.3: load vs. deflection curves of carbon FRCM strengthened specimens

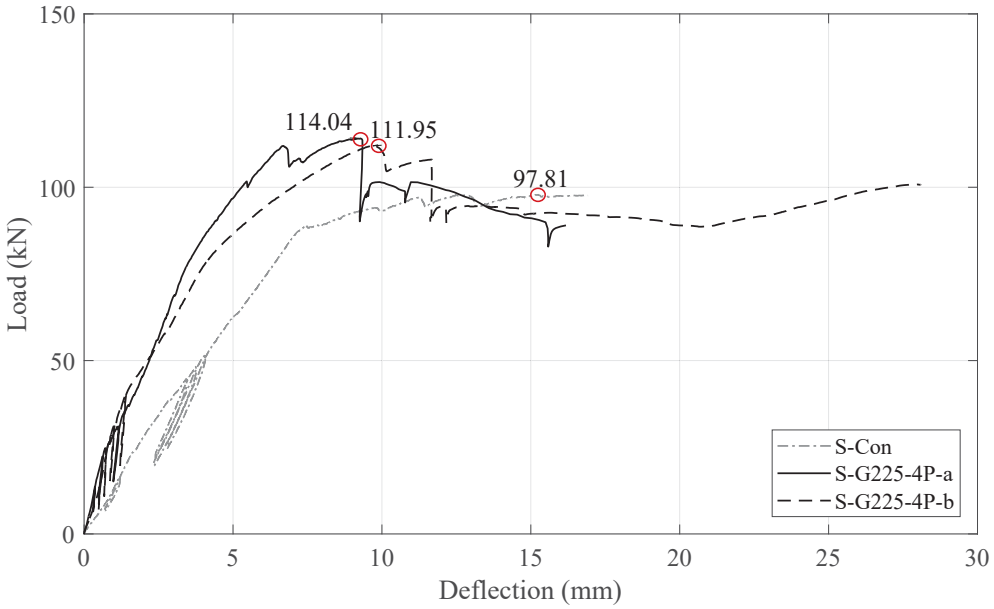

Figure 3.4: load vs. deflection curves of glass FRCM strengthened specimens

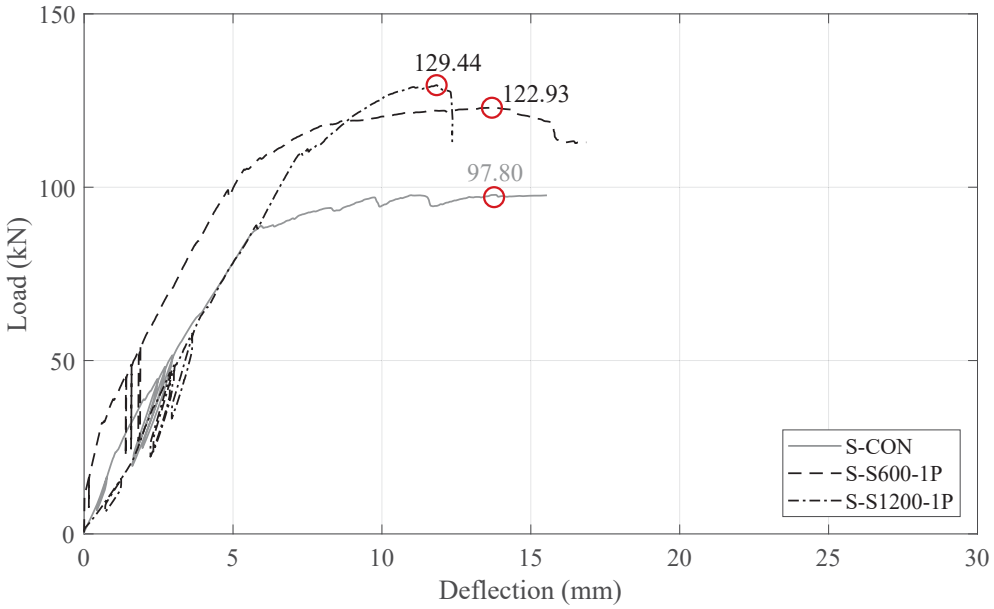

Figure 3.5: load vs. deflection curves of SRG strengthened specimens

FRCM and SRG materials controlled the crack width as shown in the Figure 3.6, where more cracks of smaller width developed in the strengthened specimens. The numbers written next to the cracks in the Figure 3.6 are the applied load in *kip* associated to the crack height.

The increase in ultimate capacity of the strengthened RC beams was 8.2% in S-C130-2P, 15.3% in S-C440-1P, 39.8% in S-C440-2P, 15.5% in S-G225-4P, 25.6% in S-S600-1P, and 32.4% in S-S1200-1P. Values of the capacity obtained from the experiments are higher than those calculated analytically. However, the experimental and analytical increase in capacity are in good agreement.

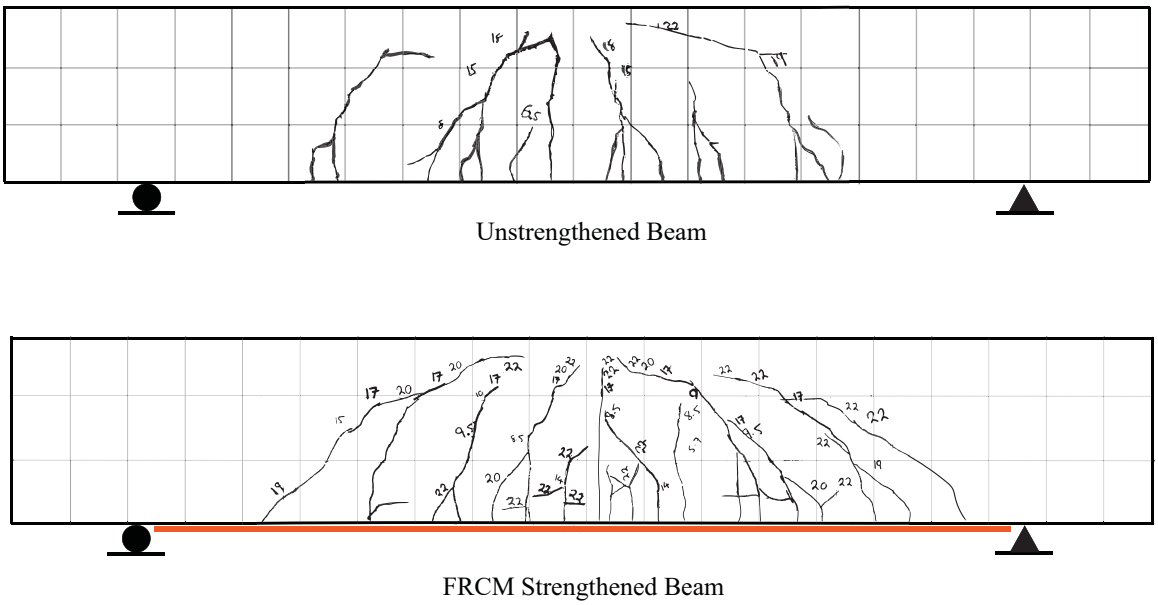

Figure 3.6: Crack pattern comparison in control and strengthened specimens

FRCM failure

The yield strain of steel rebars is 0.00259 mm/mm, which corresponds to 87 kN yield capacity in the RC beams, as shown in Figure 3.7.

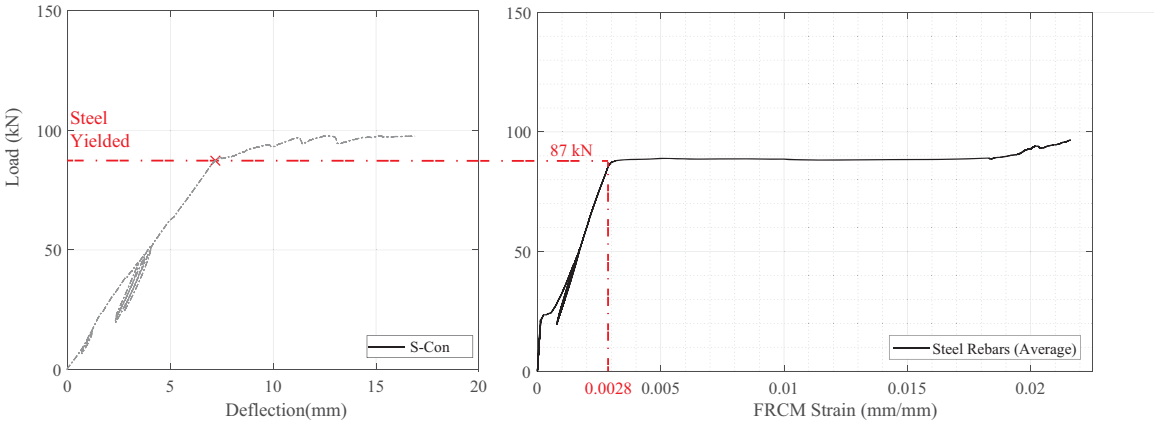

Figure 3.7: steel rebar yielding

S-G225-4P carried the tensile stresses until FRCM debonding strain at 0.0128 mm/mm, which corresponds to 113 kN load capacity in the strengthened RC beam, as shown in Figure 3.8. The S-G225-4P failure happened when the FRCM fabric yarns were internally debonded from the matrix, which resulted in high interfacial slippage in glass-FRCM strengthened specimens, and internal delamination in carbon-strengthened specimens. The debonding occurred after the steel rebars had yielded, and before the concrete crushed in compression.

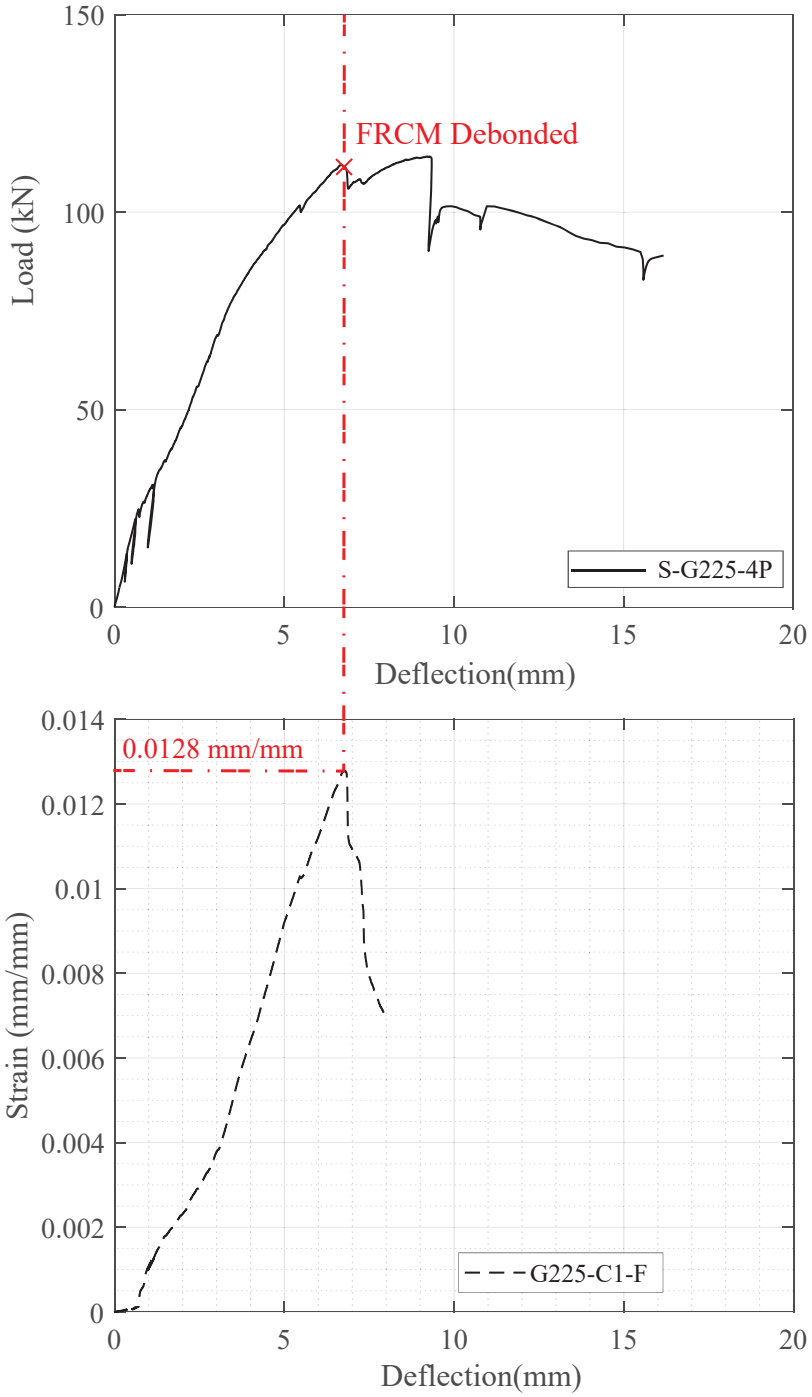

Figure 3.8: S-G225-4P FRCM debonding strain

After FRCM debonding, the beam continued to carry loads because the position of neutral axis in the cross section shifted higher, and the steel rebars which

were previously in compression, went in tension. At this stage, longitudinal cracks parallel to the steel rebars emerged on the concrete beam's face. Eventually, the concrete crushed in compression. Different stages of the failure are shown in Figure 3.9.

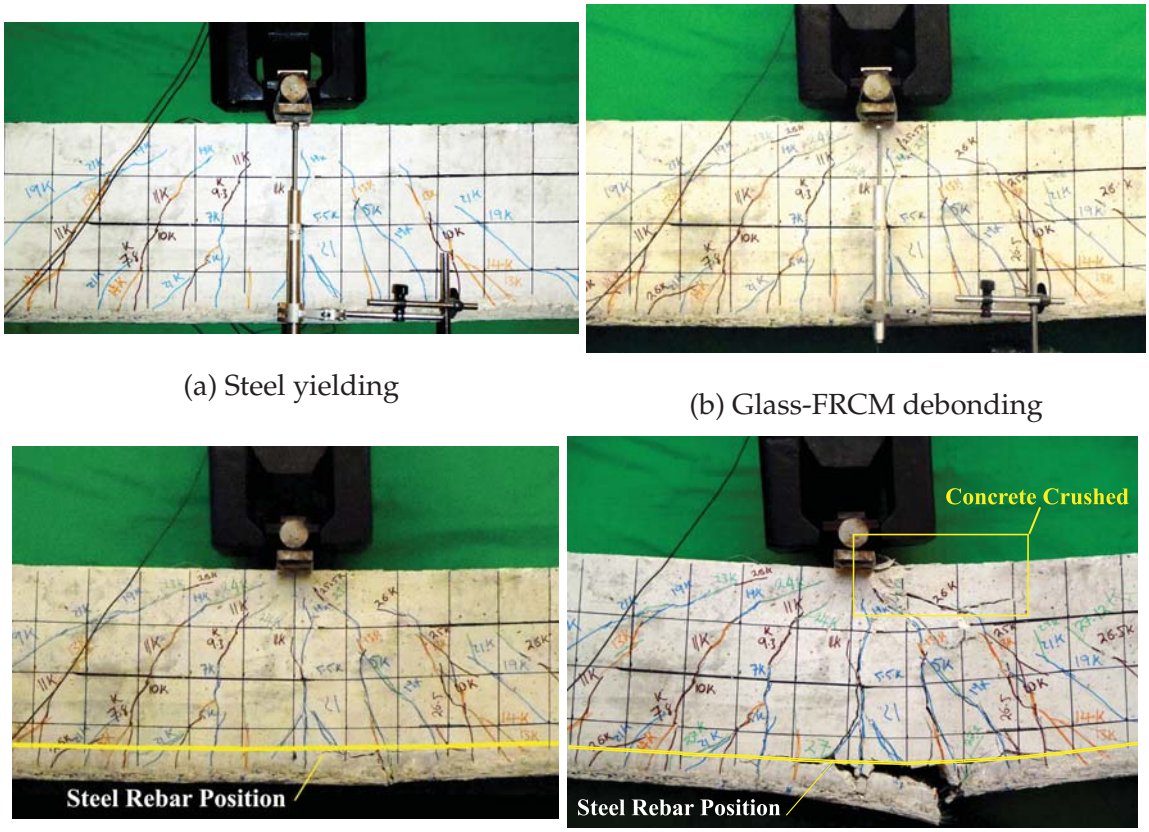

(a) Steel yielding

(b) Glass-FRCM debonding

(c) Longitudinal cracks

(d) Concrete crushing

Figure 3.9: FRCM strengthened RC beams failure

Carbon-FRCM strengthened specimens followed a similar failure mechanism as glass-FRCM strengthened specimens, but the FRCM debonding was internal delamination instead of fabric slippage as shown in Fig. 3.10.

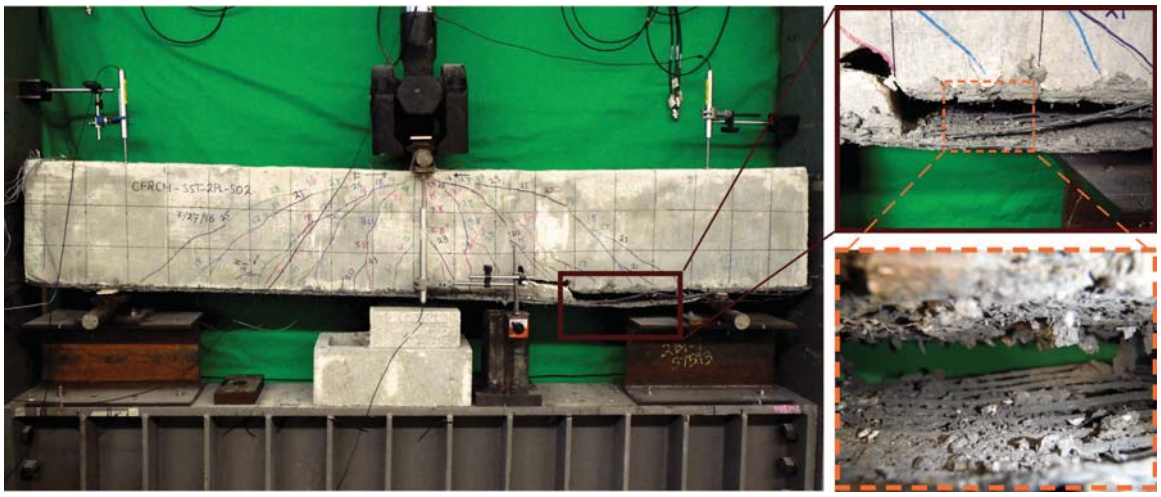

Figure 3.10: Carbon FRCM delamination

SRG strengthened specimens failed due to debonding at the fabric-matrix interface (internal) at one end as shown in Fig. 3.11. The debonding start point concurred with a flexure-shear crack in the beam and it was propagated toward the beam's end.

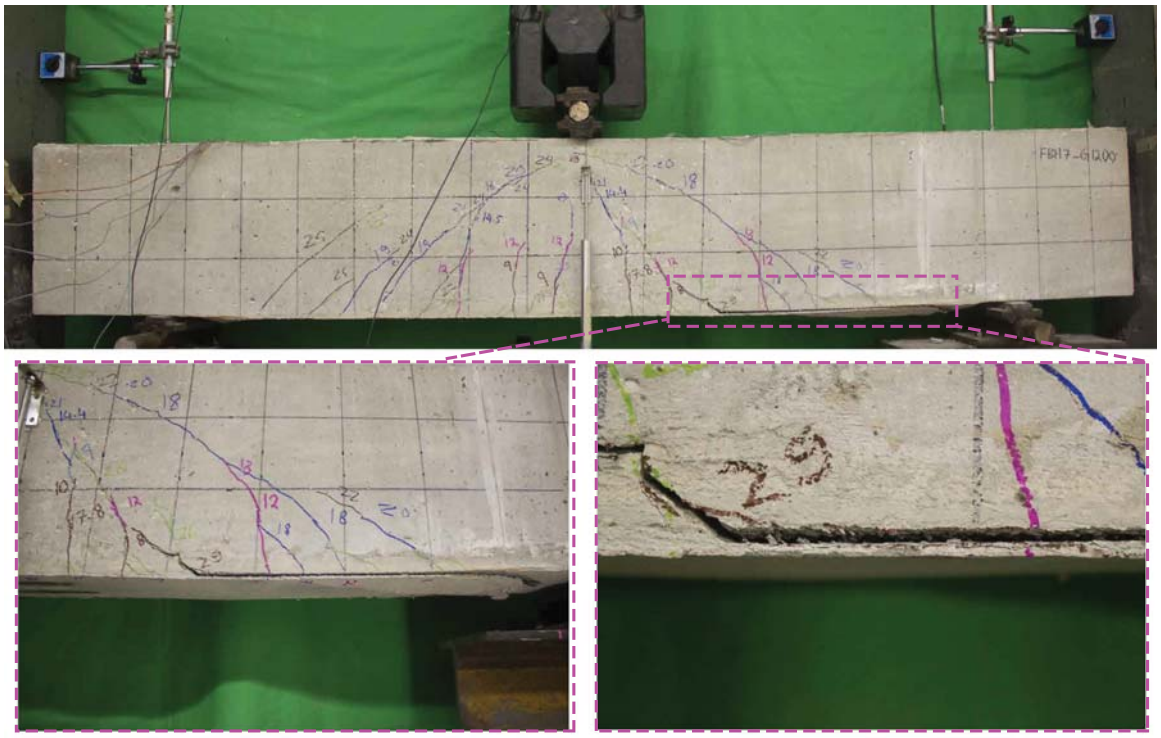

Figure 3.11: SRG debonding

In FRCM strengthened specimens, the cracks in the soffit of the RC beams were transferred to the FRCM matrix as well. Fig. 3.12 shows cracks emerging at the surface of the GFRCM. Cracks in concrete and FRCM appeared as early as 25 kN load (5.7 kip) allowing the fabric to bridge the matrix cracks.

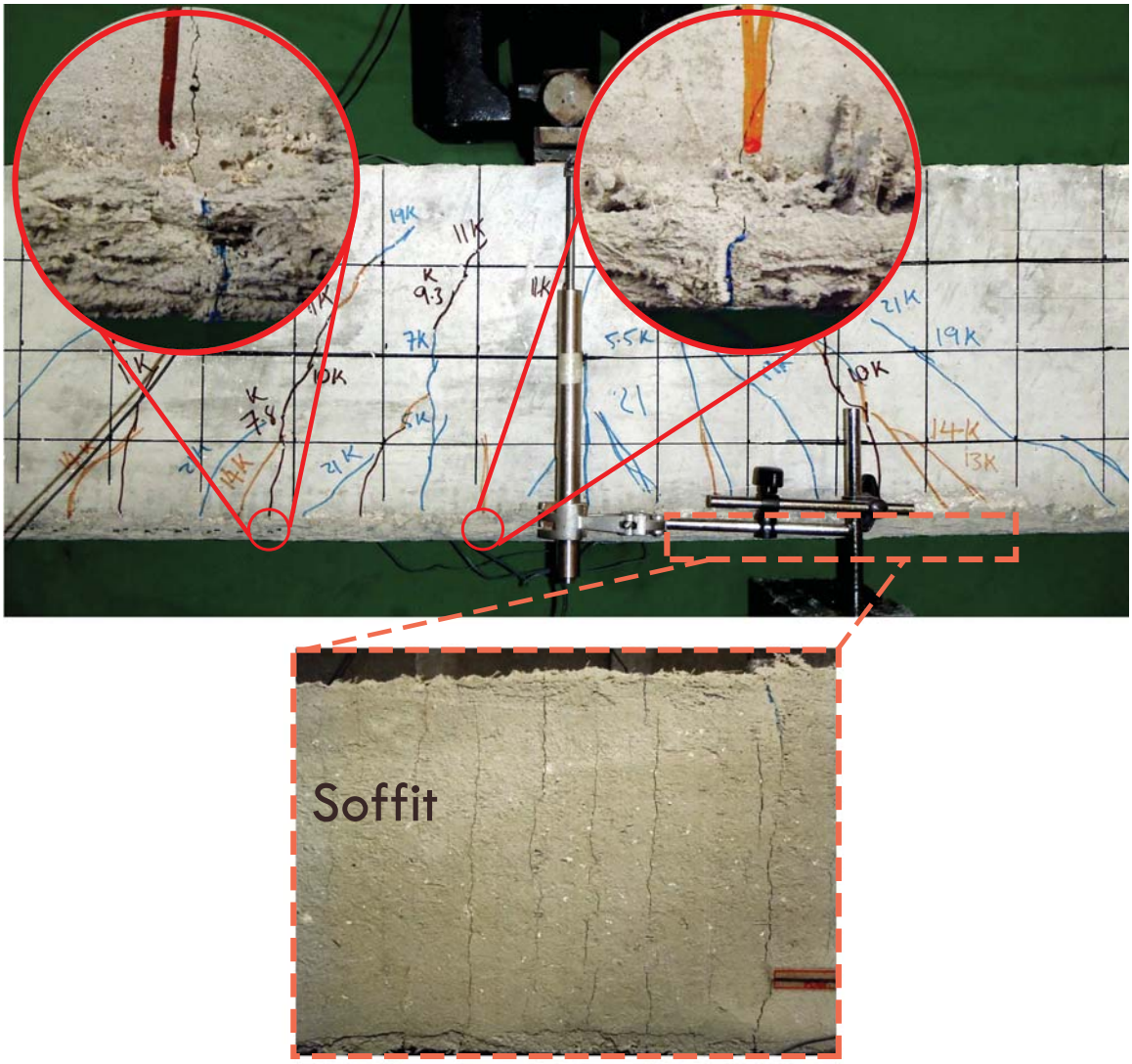

Figure 3.12: FRCM cracking

Unlike the FRCM strengthened specimens, the cracks in RC section did not emerge on the SRG surface. The SRG systems bridged the cracks internally, without visible cracks in the matrix. The micro-cracks started emerging on the surface at higher loads, close to the SRG rupture in S600-G0-S and debonding in S1200-G0-S, as shown in Fig. 3.13. In FRCM strengthened specimens, the cracks in the soffit of the RC beams were transferred to the FRCM matrix as well. Fig. 3.12 shows

cracks emerging at the surface of the GFRCM. Cracks in concrete and FRCM appeared as early as 25 kN load (5.7 kip) allowing the fabric to bridge the matrix cracks.

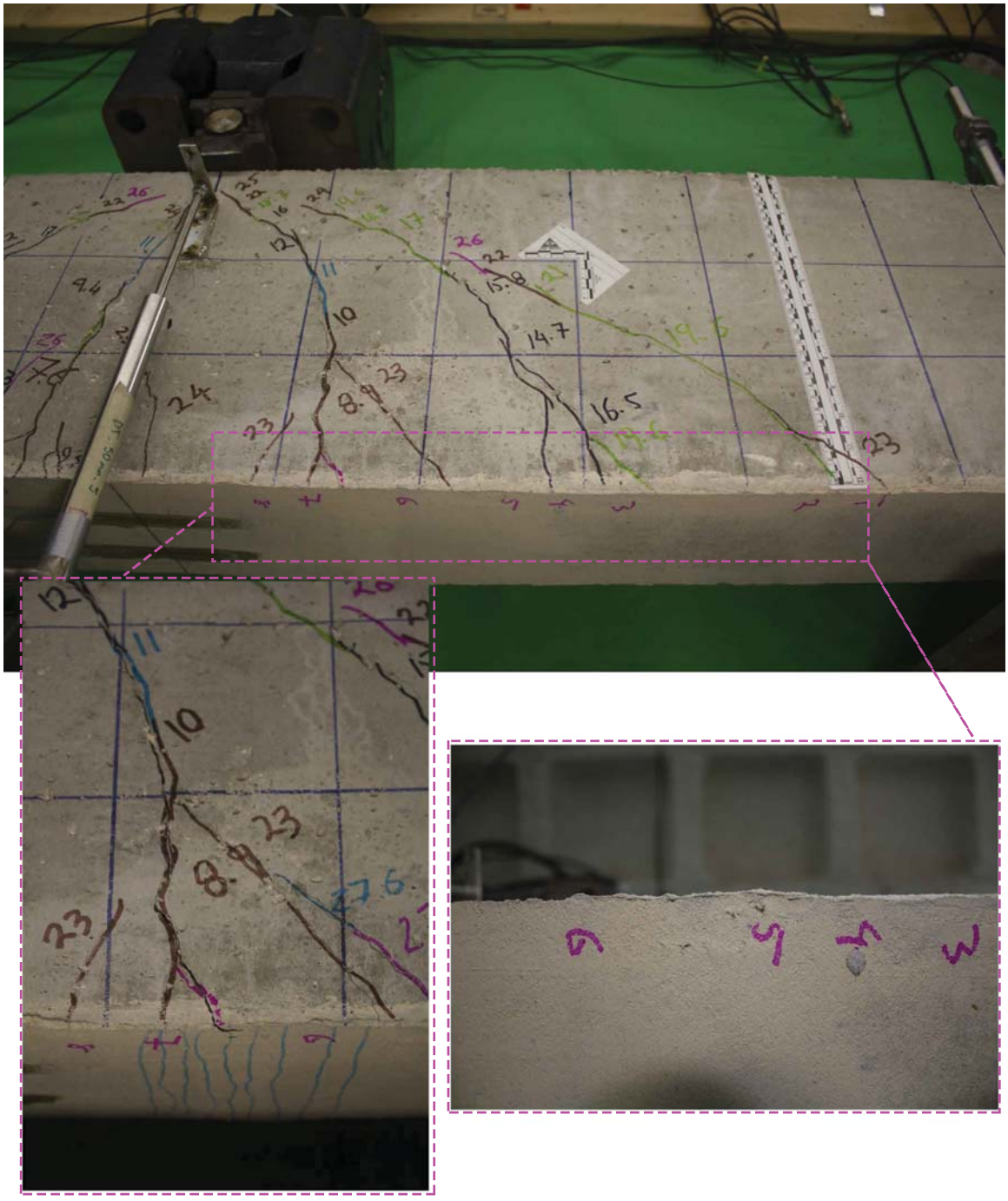

Figure 3.13: SRG cracking

3.6 Structural Performance Discussion

The increase in yield and ultimate capacities of the strengthened RC beams from experiments is in agreement with the analytical results. Compared to carbon and SRG, glass fabrics have a lower modulus of elasticity which contributes to lower β^f values, as shown in Table 3.2. Therefore, even though 4 fabric plies were used in the strengthening scheme, the flexural capacity enhancement was limited. The higher post-yielding stiffness of strengthened RC beams compared to the control beam in load vs. deflection curves is likely to be attributed to ability of FRCM/SRG to control concrete cracks.

The measured average strain in S-G225-4P at FRCM debonding was 0.0128 mm/mm in S-G225-4Pa, and 0.0148 mm/mm in S-G225-4Pb, as shown in Figure 3.14. The measured average strain in S-C130-2P and S-C440-2P at FRCM debonding was 0.0055 mm/mm and 0.0088 mm/mm, respectively, as shown in Figure 3.15. The measured average strain in S-S600-1P and S-S1200-1P at SRG debonding was 0.013 mm/mm and 0.0067 mm/mm, respectively, as shown in Figure 3.16. ACI 549.4R-13 limits the FRCM design strain to 0.012 mm/mm, which was a limiting measure only for G225-C1-F and S600-G0-S materials.

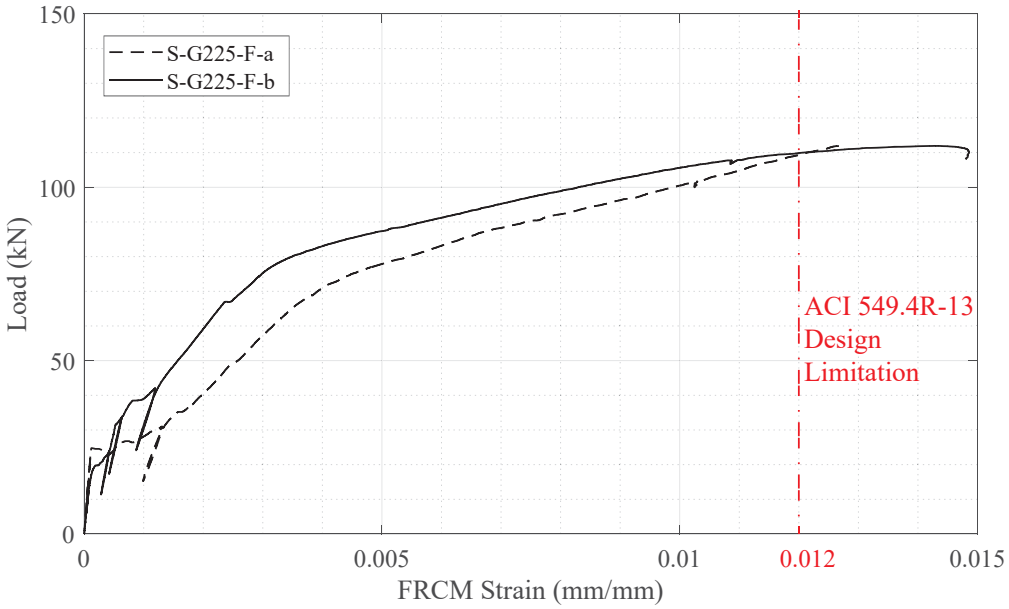

Figure 3.14: Average glass FRCM strain

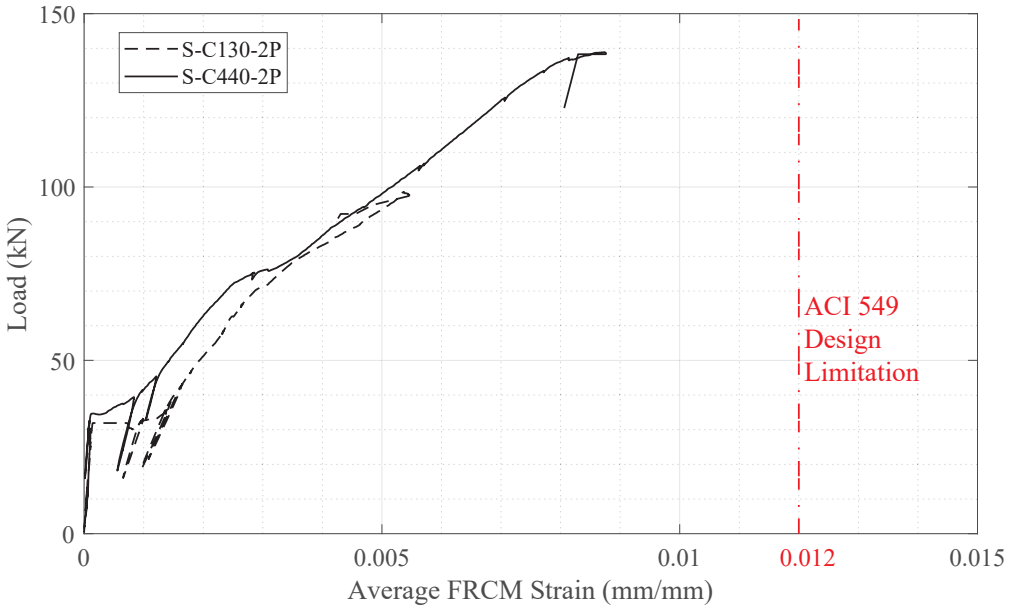

Figure 3.15: Average carbon FRCM strain

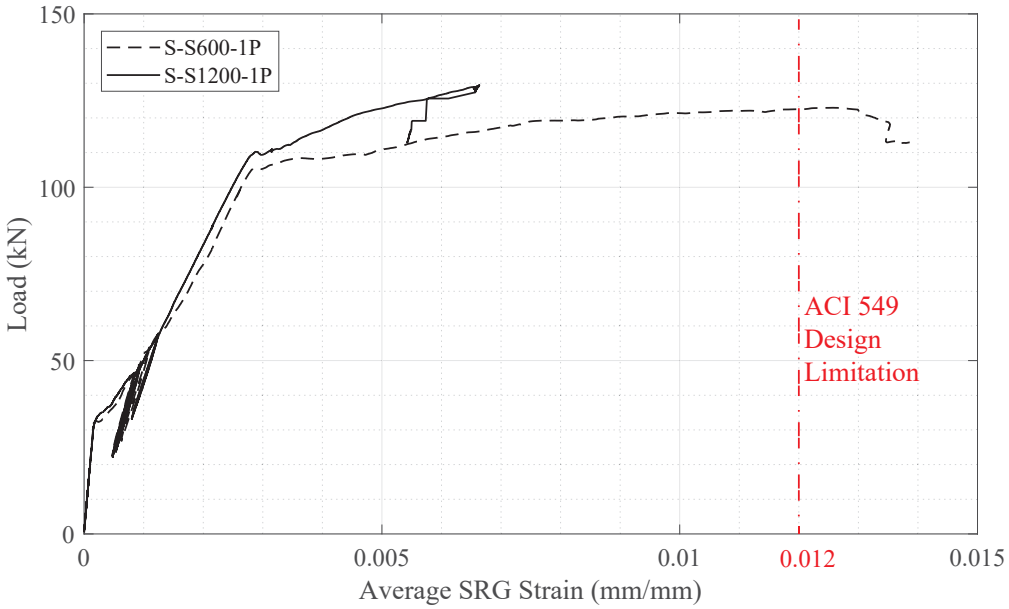

Figure 3.16: Average SRG strain

Figure 3.17 plots the analytical increase in capacity against the β^f factor. In the figure, the data from study of Pino et al. (2017) were added to those of this study in Table 3.3. The figure linear regression in the figure shows that the increase in ultimate capacity of the RC beams corresponds almost linearly to the increase in the β^f factor. Thus, by using β^f factor, the strengthening design can be done independent from the material system's characteristics. The latter is of importance in designing the strengthening projects in practice. Figure 3.18

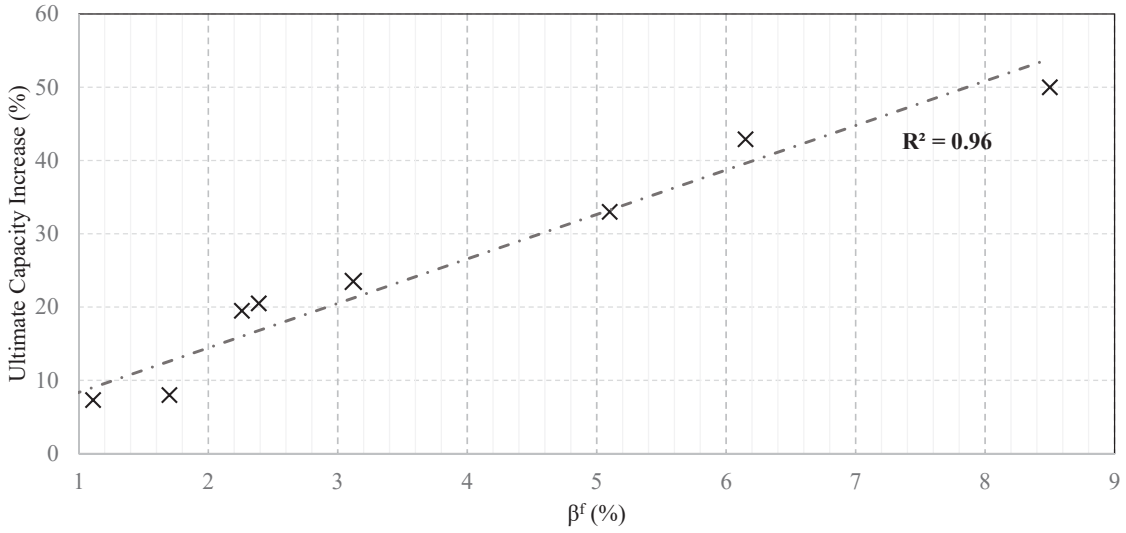

Figure 3.17: Reinforcement ratio vs. ultimate capacity increase

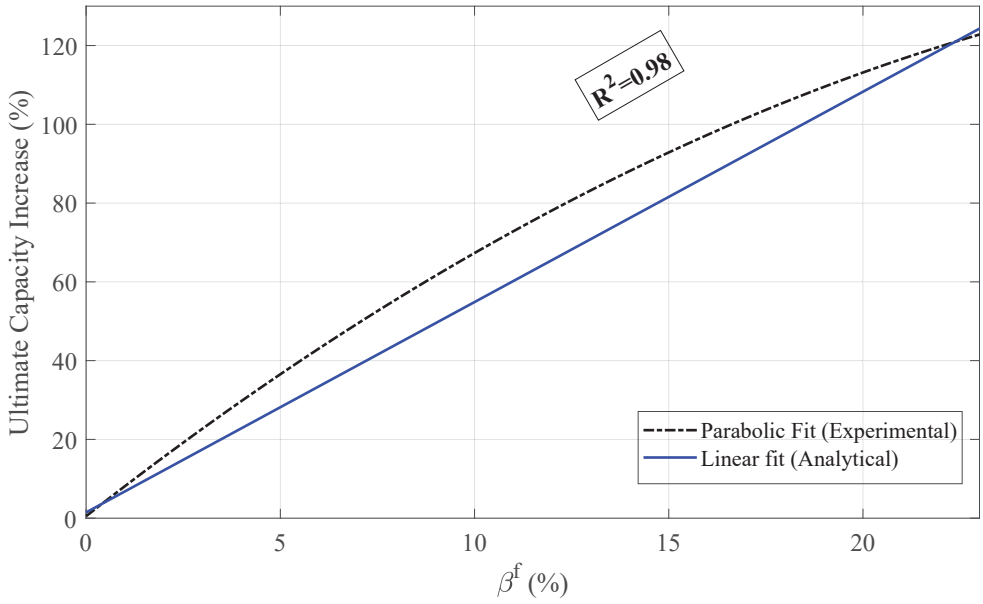

Figure 3.18: Difference between the analytical and experimental results in terms of increase in ultimate capacity

3.7 Effect of Beam Geometry

in order to study the effect of RC beam geometry on the performance of the strengthened specimens with a constant β^f ratio. Five beams with cross section dimensions 356 mm in width and 152 mm in height with 20 mm clear cover were cast. In what follows, these beams are called "slabs" (since their width is much larger than their height) in order to differentiate them from previous RC beams. The singly reinforced slabs were had three #3 (Φ9.5) rebars in tension were designed as under-reinforced flexural elements per ACI 318-14 (American Concrete Institute (ACI), 2014). Total and clear (support-to-support) span of the slabs were 1981 and 1676 mm, respectively, as shown in Fig. 3.19. The soffit of the slabs was sandblasted and power washed before SRG application. SRG strips 152 mm in width were applied on the slab soffit throughout its length, and were cut immediately before the supports to prevent anchoring of the supports. One slab was kept unstrengthened as a control specimen. Material properties of concrete and steel rebars were identical to those used previously, as listed in Table 3.1. Two SRG systems S600-G0-S and S1200-G0-S were used to strengthen the slabs. Material properties of the SRG systems are given in 2.2 of Chapter 2. Specimens follow the name order X-Y-Z, where X is the specimen type(FS for flexural slab), Y is fabric type, as mentioned in the Chapter 2 and Z is the specimen counter.

Figure 3.19: RC slab geometry and reinforcement detail

3.7.1 Slab Test Setup

RC slabs were tested using a hydraulic actuator in displacement control mode at a rate of 0.0875 mm/sec with four cycles of partial loading and unloading to crack the specimen. The slab was simply supported and the load was applied by the actuator at mid-span. Three LVDT's (one LVDT at mid-span and the other two at the supports to account for settlement) recorded displacements. The axial strain was monitored by six strain gauges: two 6 mm strain gauges on the steel rebars, two 60 mm strain gauges on concrete in compression, and two 60 mm strain gauges on the SRG external surface. The test setup is shown in Fig. 3.20.

Figure 3.20: RC slab test setup

3.7.2 Test Results

For the five slabs, the applied load is plotted against the net mid-span deflection in Fig. 3.21. The axial stiffness of the SRG cross-sections compared to the RC cross section were significantly small, thus, the SRG did not have an effect prior to cracking. After first crack, however, the SRG layer controlled the width and distribution of cracks in concrete. More cracks of smaller width appeared in the SRG strengthened slabs. The applied load required to yield the steel rebars also increased in SRG strengthened slabs. The average yielding load of S600-G0-S and S1200-G0-S strengthened slabs increased 18 and 25%, respectively. The ultimate load at failure improved in SRG strengthened specimens. On average, the ultimate load of S600-G0-S and S1200-G0-S Strengthened slabs increased by 26 and 29%, respectively.

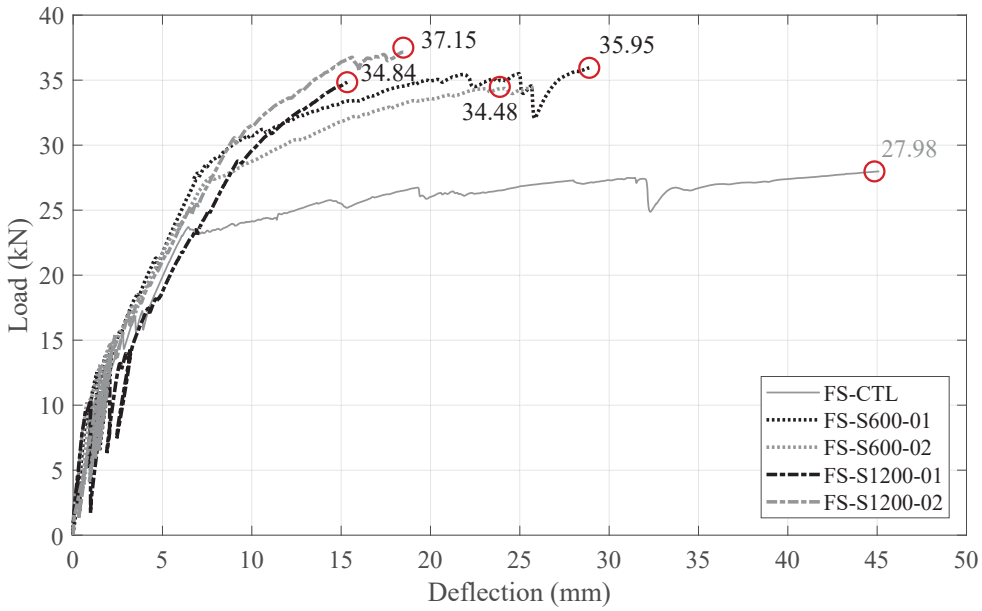

Figure 3.21: Load vs. deflection curves of strengthened RC slabs

Table 3.4 contains the experimental and analytical capacities (yielding and ultimate) for each specimen configuration. The analytical results, which were always lower than the experimental ones, were obtained through cross section analysis in accordance with ACI 549.4R-13. In the analytical results, the strength reduction factor is not considered ($\Phi = 1$).

Table 3.4: RC slab experimental and analytical capacities

		Yielding Load			Ultimate Load			
Specimen ID	β^f [%]	**Experimental** $P_{y,exp}$ [kN]	**Theoretical** **Φ=1** $P_{y.th}$ [kN]	**Ratio** $P_{y,exp}/P_{y.th}$	**Experimental** $P_{u,exp}$ [kN]	**Theoretical** **Φ=1** $P_{u.th}$ [kN]	**Ratio** $P_{u,exp}/P_{u.th}$	**Failure Mode**
FS-CTL	-	23.7	19.6	1.21	27.9	26.8	1.37	Concrete
FS-S600-01	2.73	28.9	23.2	1.24	36.0	32.3	1.12	SRG Delamination
FS-S600-02		27.3		1.17	34.5		1.07	
FS-S1200-01	2.78	28.8	24.1	1.19	34.8	32.8	1.06	
FS-S1200-02		30.5		1.25	37.2		1.13	

Failure mode of the unstrengthened slab was concrete crushing, after the steel rebars were yielded. In strengthened slabs, however, cracks developed in the area of maximum moment near the mid-span. These cracks did not emerge at the surface of the matrix up to the delamination (Fig. 3.22), suggesting that the SRG intercepted the crack development, similar to the results found in SRG strengthened RC beams.

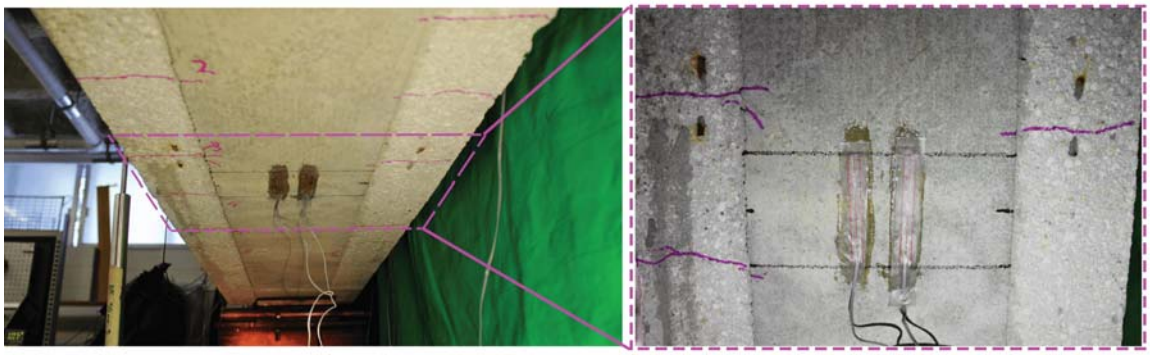

Figure 3.22: Crack control in strengthened RC slab

Slippage at fabric-matrix interface in the SRG layers initiated at the location of these cracks. Up to yielding of the steel rebars, no delamination or excessive slippage at SRG was observed. Growing deformation was followed by crack widening in concrete and more slippage of the fabric, up to the point that the tension and shear stresses at the fabric-matrix reached their capacity and eventually resulted in internal delamination as shown in Fig. 3.23.

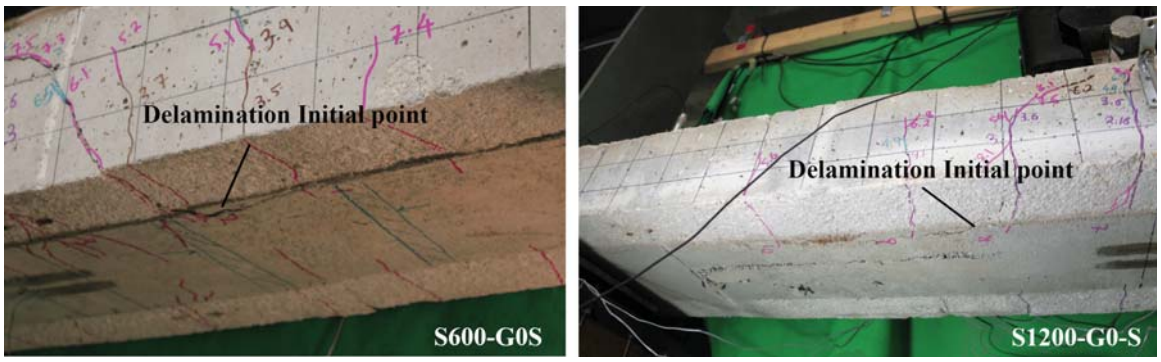

Figure 3.23: Failure of SRG strengthened RC slabs

3.7.3 Discussion

The SRG composites applied on the soffit of slabs worked as a secondary layer of reinforcement, and increased the yielding load of the rebars. The minor increase

in the stiffness of total reinforcement does not directly affect the serviceability of RC slabs (see also the insignificant change of slope in load-deflection curves in Fig. 3.21). Nevertheless, the steel rebars in strengthened RC slabs yield at higher loads. The post-yielding portions of load vs. deflection curves in Fig. 3.21 delineate the effect of SRG, where the highest stiffness (slope) was observed for S1200-G0-S strengthened slabs, followed by S600-G0-S slabs, and eventually the unstrengthened slab (which had almost a flat post-yielded portion).

The ultimate load at failure for S600-G0-S and S1200-G0-S strengthened slabs were comparable (26% for S600-G0-S vs. 29% for S1200-G0-S), which shows that increasing the SRG to rebar proportion does not necessarily translate into increasing the ultimate strength. The reason for this is the matrix-controlled failure mode, in which higher fabric/mortar ratios can cause premature delamination/debonding. From analytical results, the comparable ultimate capacity of S600-G0-S and S1200-G0-S strengthened slabs was anticipated (22.7 kN and 23.7 kN, respectively), because the stress in SRG specimens is evaluated as $E_f\epsilon_f$ per ACI 549.4R guidelines, which results a comparable value for the two SRG composites.

Comparing the results of RC beams and RC slabs shows that for a constant β^f ratio, the increase in ultimate capacity of RC slabs in Fig. 3.21 are in good agreement with those of RC beams in Fig. 3.5. On average, S600-G0-S increased the capacity of both RC beams and and RC slabs by 26%. S1200-G0-S increased the capacity of RC beams by 32% and RC slabs by 29%. Thus, in the specimens tested in this study, the β^f factor was almost independent from the beams geometry.

3.8 Conclusions

Performance of FRCM and SRG strengthened RC beams and slabs was studied in this chapter.

First, FRCM/SRG characteristics from Chapter 2 were used to analytically predict the yielding and ultimate strengths of the RC beams and slabs according to ACI 549.4R-13.

It appears that there is an almost linear relation between the reinforcement ratio β^f and increase in the ultimate capacity of the RC members, which is an important factor for design purposes.

Specimens were tested under monotonic loading. The increase in ultimate strength from experiments were in good agreement with the analytical results. The failure sequence of the strengthened specimens (from analysis and experiments) was yielding of steel rebar in tension, debonding of FRCM/SRG, and concrete crushing. The FRCM debonding was at the matrix-fabric interface with high interfacial slippage for glass FRCM, internal delamination for carbon FRCM, and debonding at substrate-matrix or fabric-substrate for SRG strengthened specimens.

The experimental and analytical results of strengthened RC slabs in this study showed that for a constant β^f ratio, the percentage of increase in the ultimate capacity of the strengthened specimens was almost constant, regardless of beam's geometry.

Chapter 4

Fatigue Behavior

FRCM is an effective and viable strengthening solution for RC structures. The performance of FRCM strengthened RC beams has been discussed in Chapter 3 of this dissertation.

Considering the current condition of the transportation infrastructure in the United States (Herrmann, 2013), an appealing application of FRCM composite is to strengthen or rehabilitate the deficient RC bridges. Bridges sustain cyclic service loads due to vehicular traffic, which makes them liable to fatigue failure (Paris, 1961). The dominant design approach of components subject to cyclic loading is to minimize the material flaws in manufacturing, and to hold the stress levels low enough to avoid crack initiation (Bathias & Paris, 2004). This "damage tolerance" method determines the crack growth under fluctuating stresses, or endurance limit, assuming that the flaws already exist in component materials. Thus, the relation of applied cyclic stress range to endured number of cycles (or S-N curves) becomes the basis for design.

This research experimentally investigates fatigue performance of FRCM strength-

ened RC beams. A glass and two carbon FRCM systems were studied. FRCM type, strengthening configuration, RC beam sections, and test setup were identical to those in Chapters 2 and 3. The results of strengthened RC beams tested under monotonic loading were used in fatigue analysis, and serve as benchmarks for residual strength computation. Strengthened RC beams were tested under cyclic loading with variable applied peak load. Fatigue life and failure mechanisms were studied. Combined S-N curves of PBO (Pino et al., 2017), carbon, and glass FRCM strengthened RC beams allow to draw new recommendations for fatigue life.

4.1 Materials and RC Beams

Two carbon (C130-C2-F, C440-C2-F) and a glass (G225-C1-F) FRCM systems were used to strengthen the RC beams. The FRCM systems were introduced and their mechanical performance was discussed in detail in Chapter 2. Table **??** provides material characteristics of the FRCM systems.

RC beams were identical to those used in studying the performance of FRCM strengthened RC beams under monotonic loading in Chapter 3. 3.1 shows the beams geometry and reinforcement details. The FRCM strengthening configuration is according to the Table 3.2.

4.2 Test Setup

Fatigue tests were conducted on strengthened RC beams under cyclic loading up to two million cycles or failure, whichever occurred first. The literature (Helgason et al., 1976) suggest that the fatigue behavior of RC beams becomes stable after

two million cycles. Test results of strengthened beams under monotonic loading in Chapter 3 were used in fatigue calculation and served as benchmarks in determining the residual stress in fatigue tests that reached two million cycles of loading. Fatigue tests were conducted in force control mode. The specimens were cracked through four cycles of monotonic loading and unloading prior to fatigue testing.

Chang & Kesler (1958) suggested that fatigue failure of tensile steel reinforcement is known to be the main reason of failure in underreinforced beams that are not subject to severe shear stresses. In case of FRCM strengthened beams, Walton & Yeung (Walton & Yeung) in a study of composite tendons found that fatigue life of composites outperformed that of conventional steel. Therefore, applied cyclic loads were normalized to a certain percentage of the load required to yield reinforcing steel in the beam. Beam's capacity at the onset of yielding of steel rebars was determined from section analysis in Chapter 3 and verified with experimental test results. The proportional loads are called *percentage of static yield* (PSY) herein. Advantages of using PSY to express the load are twofold: firstly, the level of stresses in steel reinforcement in control and strengthened beams are comparable, so any gain or loss in terms of fatigue life when FRCM is applied can be highlighted. Secondly, by using PSY, the strengthened beams will receive a higher load in order to maintain the same level of stress in the reinforcing steel.

Cyclic load frequency of 2 Hz was kept constant for all specimens. This relatively low frequcny was chosen to provide enough space for the beams to completely recover between load cycles (Emberson & Mays, 1996) and to avoid hysteresis effects.

To generate cyclic loading, minimum cyclic load equivalent to 20 PSY was used for

all the specimens based on the suggested loading in AASHTO LRFD-2014 (American Association of State Highway and Transportation Officials (AASHTO), 2014) provision. Maximum cyclic load was variable, and it was chosen a value less than 85 PSY. The maximum load also was chosen so that the compressive stress in concrete remained below $0.45f'_c$.

4.3 Carbon FRCM

4.3.1 Experimental Results

Fatigue test results are summarized in Table 4.1. In the table, results of a previous study of the authors (Pino et al., 2017) that was conducted on the same beam geometry strengthened with three layers of PBO FRCM are included for reference. Fatigue specimens follow the name order X-Y-Z, where X and Y are the loading and fabric type, respectively, as mentioned in the Chapter 2 and Z denotes the maximum applied cyclic load in PSY. In order to determine the failure mechanism, steel rebars in tension were extracted from failed specimens and observed under Scanning Electron Microscope (SEM). SEM images of fractured surface of the steel rebars in those specimens that failed before reaching two million cycles of loading confirmed that fatigue fracture of the steel rebars was the leading failure cause. Images of the fractured rebar surfaces matched the fatigue fracture pattern found in the work of Helgason et al. (1976).

Fatigue lives of three specimens under the same applied proportional load ex-

pressed in PSY (F-Con-75, F-C130-75 and F-C440-75) were different but all followed a trend: the higher the FRCM ratio, the longer the fatigue life. Theses results preliminarily suggested that FRCM materials might improve the fatigue life of RC members. Although the fact that FRCM composites impeded crack propagation in concrete supports this idea, it is not feasible to verify such a hypothesis in this study. If FRCM mechanical properties obtained per AC434 guidelines are presumed over-conservative, the real capacity of RC beam is higher than calculations and also the FRCM will carry a bigger share of applied load. Thus, the stress in reinforcing steel will be less than the estimated PSY and it can be a probable cause for the longer fatigue life.

Specimens that endured two million cycles of load repetition were unloaded and tested under monotonic loading to determine their residual strength. The test setup and procedure used for residual strength was the same as monotonically tested specimens described in the previous section. As shown the columns 7 and 8 of Table 4.1, fatigue loading did not remarkably affect the residual strength of these specimens. This is also more evident in Figure 4.1 where residual strength of F-C130-65 and F-C440-65 are compared to monotonically tested S-CON, S-C440a and S-C130 specimens. Compared to the S-C440a benchmark beam, the specimen F-C440-65 showed some damage having been subjected to two million load cycles, but the ultimate capacity almost did not change. The damage and loss of ultimate capacity in F-C130-65 was less, and the beam performed nearly identical to its monotonically tested benchmark S-C130.

Table 4.1: Summary of carbon FRCM fatigue results

Specimen ID	Peak Load PSY kN	β^f (%)	Endured Cycles x10^6	Failure Type	Residual Max. Load Pu_R kN	Residual/ Exp. Load $P_{u_R}/P_{u_{avg}}$
F-CON-75	75	51	-	0.824	S[a]	-
F-C130-75	75	53		1.334	S	-
F-C130-70	70	49	1.7	1.231	S	-
F-C130-65	65	46		2.000	N/A	108
F-C130-60	60	42		2.000	N/A	102
F-C440-75	75	57		1.526	S	-
F-C440-70	70	53	6.0	1.959	S	-
F-C440-65	65	49		2.000	N/A	132
F-PBO-90	90	62		0.492	S	-
F-PBO-85	85	58		0.562	S	-
F-PBO-80a	80	55	5.1	2.000	N/A	132
F-PBO-80b	80	55		1.890	S	-
F-PBO-75a	75	51		2.000	N/A	125
F-PBO-75b	75	51		2.000	N/A	120

[a] Steel: fatigue fracture in the steel rebars.

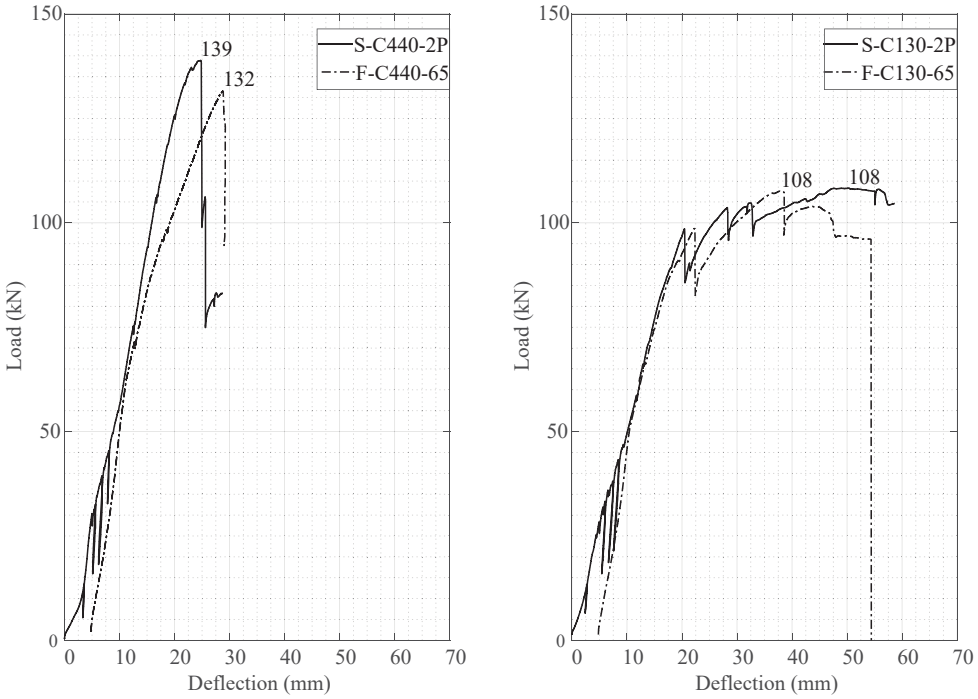

Figure 4.1: Residual capacity of F-C440-65 (left) and F-C130-65 (right)

4.3.2 Strain and Stress

At the maximum cyclic load, the strain in FRCM fibers was back-calculated and normalized to the ultimate FRCM design strain. These Design Normalized FRCM Strains (DNFE) appear in the fourth column of Table 4.2. In obtaining DNFE values, the ultimate strain of the FRCM was limited to 0.012 mm/mm and the tensile strength was reduced to the average value minus one standard deviation per ACI 549.4R-13 to reflect the design properties. These calculations were repeated in the fifth column of Table 4.2 using the ultimate strain values obtained from the tests and given in Table 2.2 without being limited to the threshold values and are called Theoretical Normalized FRCM Strains (TNFE). The values of DNFE are conserva-

tive by a margin of almost 5.0% if compared to the TNFE. The same calculation was repeated to estimate the normalized stresses in the FRCM under the peak load. Design Normalized FRCM Stresses (DNFS) and Theoretical Normalized FRCM Stresses (TNFS) are stresses developed in the FRCM under corresponding applied peak load that are normalized to the tensile strength of FRCM. Under cyclic loading, ACI 549.4R-13 limits the value of DNFS to 0.55 for carbon and 0.30 for PBO FRCM. In two strengthening configurations, C130 and PBO, values of DNFS were higher than the allowed stresses and yet no fatigue failure was associated to the FRCM. Thus, it can be concluded that stress limitation due to fatigue given in the ACI 549.4R-13 is valid within an acceptable margin of safety.

To verify that the hypothesis that concrete in compression remained linear elastic (stress less than $0.45f'_c$), strain and stress of the concrete in compression were also back calculated. The maximum stress in compression concrete peaked $0.34f'_c$ under F-C440-75 specimen.

Table 4.2: Strains and stresses in the carbon FRCM under peak PSY

Specimen ID	Peak PSY	β^f (%)	DNFE[1]	TNFE[2]	DNFS[3]	TNFS[4]
F-CON-75	75	-	-	-	-	-
F-C130-75	75		0.26	0.20	0.64	0.60
F-C130-70	70	1.7	0.24	0.19	0.63	0.59
F-C130-65	65		0.22	0.17	0.62	0.58
F-C130-60	60		0.20	0.16	0.61	0.57
F-C440-75	75		0.21	0.15	0.39	0.34
F-C440-70	70	6.0	0.19	0.14	0.38	0.33
F-C440-65	65		0.18	0.13	0.37	0.32
F-PBO-90	90		0.19	0.13	0.43	0.41
F-PBO-85	85		0.18	0.12	0.42	0.40
F-PBO-80a	80	5.1	0.17	0.11	0.41	0.39
F-PBO-80b	80		0.17	0.11	0.41	0.39
F-PBO-75a	75		0.16	0.10	0.40	0.38
F-PBO-75b	75		0.16	0.10	0.40	0.38

[1] Design Normalized FRCM Strain under peak applied cyclic load.

[2] Theoretical Normalized FRCM Strain under peak applied cyclic load.

[3] Design Normalized FRCM Stress under peak applied cyclic load.

[4] Theoretical Normalized FRCM Stress under peak applied cyclic load.

4.3.3 Deflection

Figure 4.2 shows the mid-span normalized deflection, which is the ratio of deflection at each cycle over the deflection at the beginning of the first cycle (after the specimen was cracked). Note that per experiment method, specimens were monotonically loaded up to average of the maximum and minimum applied cyclic load to prevent generating an impact force from the actuator at the beginning of

the cycles. Results of C130-C2-F and C440-C2-F strengthened specimens are plotted together to better demonstrate the trends of normalized deflection over cycles. Mid-span deflection was always increasing for specimens that failed before two million cycles, and stable for those that endured two million cycles. In the beams that failed before two million cycles, the increasing deformation was accommodated through slippage of fibers within matrix, up to the point that fatigue rupture took place in the reinforcing steel and all of the tensile stress was transferred to the FRCM and resulted in delamination at the matrix-fabric interface. In the beams that endured two million cycles, no sign of delamination or debonding was observed. However, the FRCM matrix was cracked and normalized deflection up to 1.05 were recorded. Although difficult to measure, this increase in deflection had to be translated to the FRCM by means of slippage of fibers within the matrix.

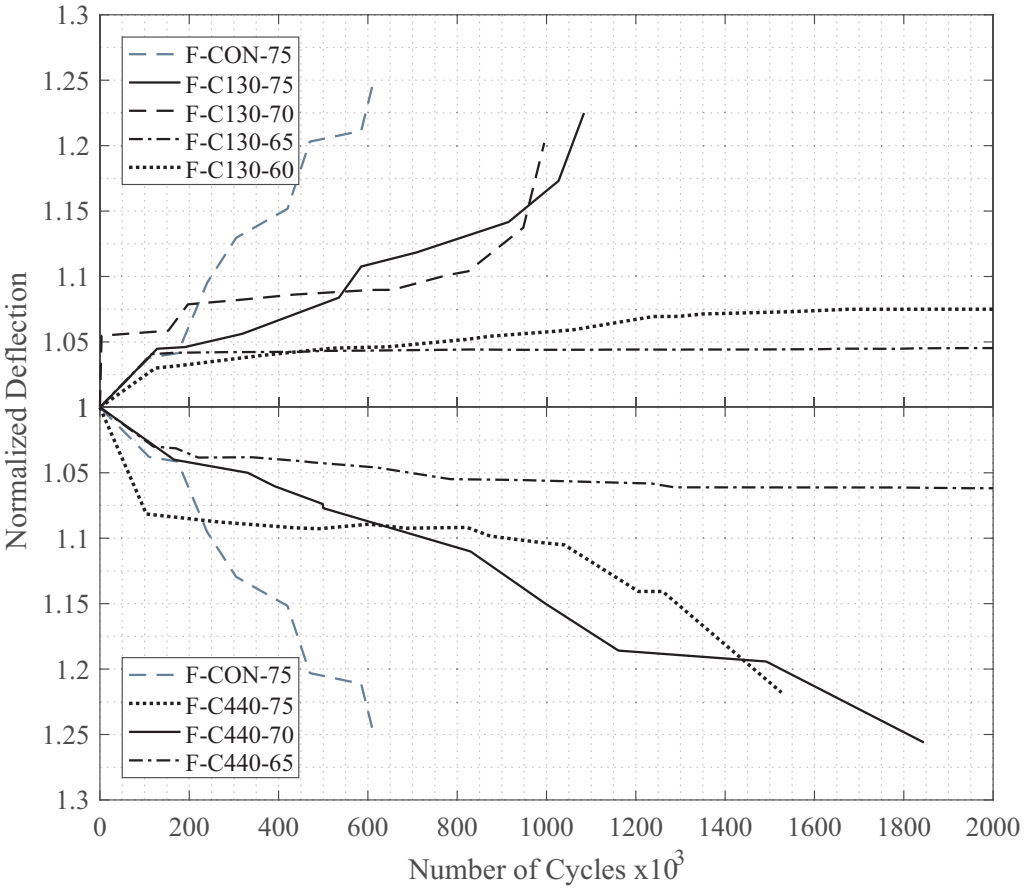

Figure 4.2: Normalized deflection versus number of cycles

4.3.4 S-N Curves

For all the specimens tested under fatigue loading, the stress versus number of cycles, known as S-N curves, are presented in Figure 4.3. In Figure 4.3a, the vertical axis represents the maximum applied cyclic load in PSY and the horizontal axis represents the corresponding endured number of cycles. Specimens that with-

stood up to two million cycles are shown with an arrow. Results of the PBO FRCM strengthened beams are also included (Pino et al., 2017). Predictably, increasing the maximum applied stress resulted in shorter fatigue life of the specimens. Based on the S-N curves, if the maximum cyclic load on C130-C2-F and C440-C2-F strengthened beams was less than 65 PSY, the beam could endure two million cycles of loading without suffering fatigue failure. The results of carbon and PBO FRCM were consistent in general, but the fatigue endurance of PBO FRCM was slightly higher. A probable explanation for the difference in fatigue endurance limit of carbon and PBO strengthened beams can be the fact that the FRCM material properties obtained from experimental results per AC434 did not reflect realistic values and resulted in an inaccurate estimation of stress in the steel rebars. Compared to the control beam, all the strengthened specimens subject to the same maximum cyclic load equivalent to 75 PSY (F-C130-75, F-C440-75 and also the PBO strengthened beam under 75 PSY) had an extended fatigue life.

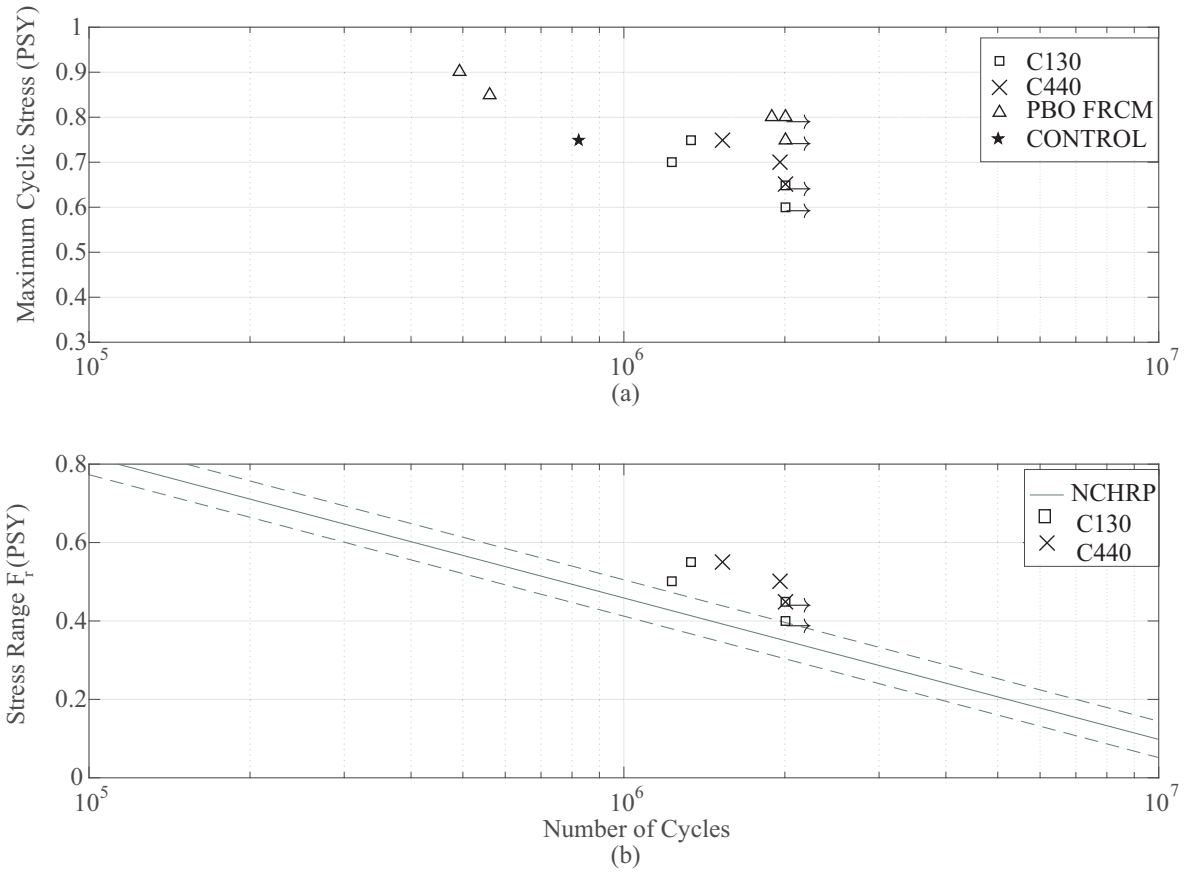

Figure 4.3: Stress versus number of cycles

In the literature, effects of the minimum applied stress on fatigue life is often taken into consideration by using stress range F_r, that is the difference between maximum and minimum applied stress. Figure 4.3b shows the applied stress range versus number of endured cycles for C130-C2-F and C440-C2-F strengthened beams while the minimum stress range was constantly 20 PSY for all the specimens. In Figure 4.3b, results of a comprehensive experimental campaign of the National Cooperative Highway Research Program (NCHRP) (Helgason et al., 1976) on fatigue behavior of steel rebars in RC beams are also shown. The study of fatigue performance of FRCM composites herein and the NCHRP study of fatigue

performance of steel rebars share similar test setup, rebar grade, rebar size, and minimum applied cyclic stress. Thus the two data sets are comparable. Results of the NCHRP experiments was formulated in logarithmic relation between stress range and number of cycles in the following form:

$$Log(N) = 7.2714 \pm 0.1285 - 0.0461 F_r \tag{4.1}$$

where statistically, the corrective coefficient (± 0.1285) is to consider the effects of minimum applied cyclic load f_{min}, the grade of rebars G and their diameter D_{nom} on fatigue life of steel rebars in concrete beams. These parameters impose an upper and lower bounds on the main experimental equation and are shown in the Figure 4.3b with dashed lines. Carbon FRCM strengthened beams are very approximate to the NCHRP upper bound. However, comparatively, the strengthened beams are located above the NCHRP S-N curves. So similar to the conclusions drawn from Figure 4.3a, the results imply that a strengthened beam can endure more number of load cycles while sustaining the same stress range than its unstrengthened counterpart.

4.4 Glass FRCM

4.4.1 Experimental Results

Seven RC beams were tested under cyclic loading. One beam was unstrengthened and served as a control specimen and six others were strengthened with 4-ply G225-C1-F. The peak applied cyclic load was the main variable of the tests. The peak cyclic load ranged from 60 PSY to 85 PSY. Table 4.3 lists the tested speci-

mens ordered by the applied peak load and their corresponding endured number of cycles. Cyclic loading was applied up to two million cycles or failure, whichever occurred first. The specimens which endured two million cycles were tested under monotonic loading to obtain their residual strength. The residual strength of these beams (called residual specimens in the following) was compared to the average of the ultimate strength of the monotonically loaded FRCM strengthened RC beams (called benchmark specimens in the following), as shown in the last column of Table 4.3. Figure 4.4 compares the applied load vs. deflection curves of the residual and benchmark specimens, in which the X marker indicates the FRCM debonding, and the triangle marker indicates the ultimate strength.

As shown in Table 4.3, three specimens with 75, 65, and 60 peak PSY endured two million cycles of loading. Among the three, the F-G225-75a was considered an anomaly to the endurance limit trend because a specimen with lower peak cyclic load (F-G225-70) had failed at 882,000 cycles. Therefore, the test was repeated with 75 PSY peak load (specimen named F-G225-75b), in which the specimen endured only 635,000 cycles. The ultimate residual strength in specimen F-G225-75a was 96.7 kN, while the G225-C1-F debonded at 88.9 kN. The specimen F-G225-65 showed a similar behavior, in which the ultimate strength was 102.6 kN when concrete crushed, while G225-C1-F debonded at earlier but around the same load (see different peak stress and debonding deflections in Figure 4.4). Comparing the specimens F-G225-75a to F-G225-60 shows the extent of fatigue damage in G225-C1-F in residual specimens. The residual specimen F-G225-60 behaved similarly to the benchmark specimens, i.e., the FRCM debonding marked the ultimate capacity

of the strengthened RC beam. The strength loss in F-G225-60 was minimal (only 5%) compared to 9 and 15% strength loss in F-G225-75a and F-G225-65 specimens.

Table 4.3: Summary of glass FRCM fatigue results

Specimen ID	**Peak PSY**	**Peak Load kN**	**Endured Cycles** x10^6	**Failure Type**	**Residual Max. Load** Pu_R **kN**	**Residual/ Bench-mark Load** $P_{u_R}/P_{u_{avg}}$
F-CON-75	75	51.0	0.824	S[1]	-	-
F-G225-85	85	58.9	0.316	S	-	-
F-G225-75a	75	52.9	2.000	N/A	96.71	0.85
F-G225-75b	75	52.9	0.635	S	-	-
F-G225-70	70	48.5	0.882	S	-	-
F-G225-65	65	45.1	2.000	N/A	102.63	0.91
F-G225-60	60	41.6	2.000	N/A	107.08	0.95

[1] Steel: fatigue fracture in the steel rebars.

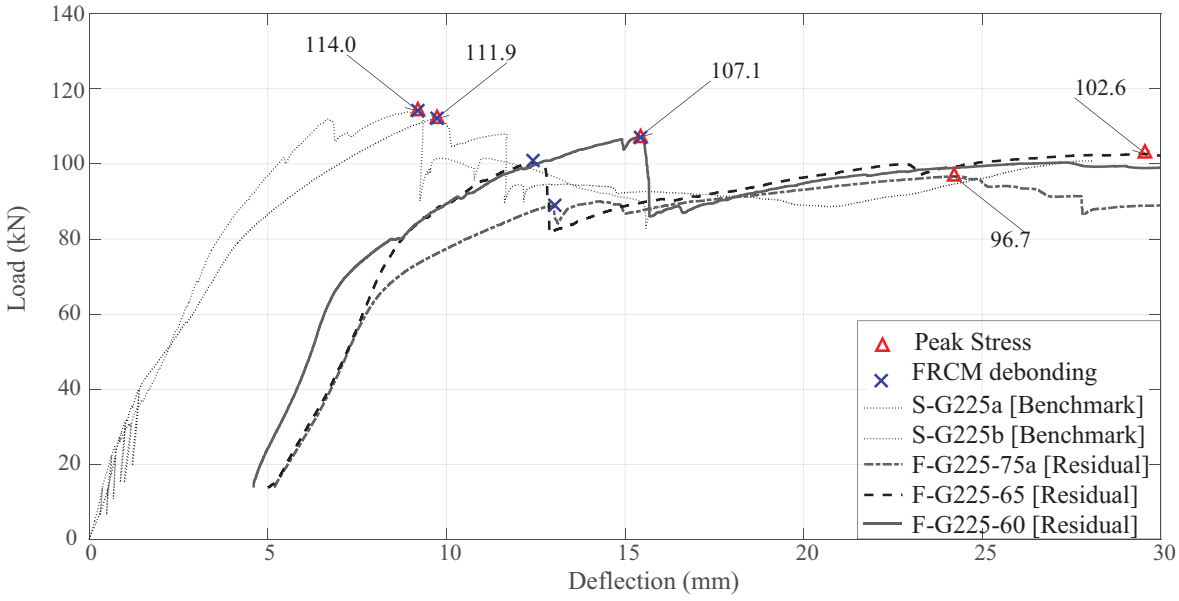

Figure 4.4: Residual strength

4.4.2 Post Failure Inspection

Three specimens which failed under cyclic loading (F-G225-85, F-G225-75b, and F-G225-70) were examined in detail. Tension steel rebars were extracted from the concrete without tampering the fracture surface. Scanning Electron Microscope (SEM) images in Figure 4.5 taken from the fracture surface showed fatigue cracks in the steel rebars.

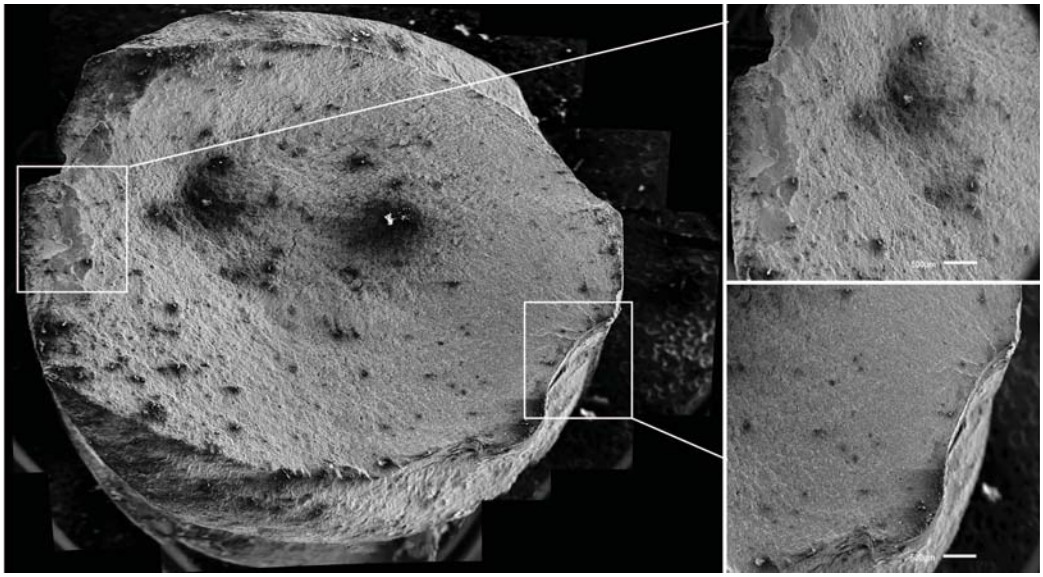

Figure 4.5: Steel rebar fracture surface

4.4.3 Stress and Strain in FRCM

Stresses and strains in G225-C1-F under peak cyclic loads were calculated. Table 4.4 shows *design* and *theoretical* strains and stresses in G225-C1-F under various applied peak cyclic loads, which were normalized to the ultimate strain and ultimate stress values. In calculating the *design* values (DNFE and DNFS), G225-C1-F ultimate strain (i.e., mean characteristic value minus one standard deviation, as per Table 2.2 was limited to $0.012 mm/mm$, following ACI 549.4R-13. In calculating the *theoretical* values (TNFE and TNFS), G225-C1-F ultimate strain value of 2.2% from Table 2.2 was used, with no limitation.

The highest normalized design stress, DNFS, in G225-C1-F was 0.49 in F-G225-85, at which the failure was in the steel rebars rather than the G225-C1-F. ACI 549.4R-13 limitation on design stress in presence of fatigue and creep is $0.2 f_{fd}$ for G225-C1-F, which is on the safe side compared to the analytical results.

The maximum theoretical normalized stress, TNFS, in G225-C1-F was 0.47 in F-G225-85, which was very close to the fatigue threshold of glass fibers. The literature on fatigue threshold of glass fibers (Mandell et al., 1985) suggest that 0.49 peak cyclic stress can cause fatigue rupture at higher cycles (close to one million cycles). However, the steel rebar fatigue rupture was governing in this study.

Table 4.4: Strains and stresses in G225-C1-F under peak cyclic loads

Specimen ID	Peak PSY	β^f (%)	DNFE[1]	TNFE[2]	DNFS[3]	TNFS[4]
F-CON-75	75	-	-	-	-	-
F-G225-85	85		0.233	0.128	0.492	0.466
F-G225-80	80		0.220	0.121	0.488	0.462
F-G225-75a	75		0.206	0.113	0.483	0.457
F-G225-75b	75	1.1	0.206	0.113	0.483	0.457
F-G225-70	70		0.192	0.106	0.479	0.453
F-G225-65	65		0.178	0.098	0.474	0.449
F-G225-60	60		0.165	0.091	0.470	0.445

[1] Design Normalized FRCM Strain

[2] Theoretical Normalized FRCM Strain

[3] Design Normalized FRCM Stress

[4] Theoretical Normalized FRCM Stress

4.4.4 Steel Rebars

ACI 549.4R-13 limits the tensile stress in steel rebars under "service loads" to $0.8f_y$, which the chief reason for choosing high peak cycling loads up to 85 peak PSY in this study. However, the experimental results proved that fatigue rupture

in the steel rebars can occur at lower stresses, e.g., 70 peak PSY.

Equation 4.1 shows that steel rebar fatigue rupture under two million load cycles takes place at peak cyclic stresses higher than 48 PSY. Thus, the 65 peak PSY steel rebar fatigue threshold in this study might be related to the FRCM material characterization, as it is discussed in what follows.

4.4.5 S-N Curves

Peak applied cyclic stress vs. number of endured cycles to failure, or S-N curves, are plotted in Figure 4.6. The graph puts three sets of data for RC beam strengthened with G225-C1-F, PBO-FRCM (Pino et al., 2017), and two types of carbon-FRCM from 4.1 together. Specimens which did not fail until two million cycles are marked with an arrow. These three systems have different characteristics and β^f ratios. Four curves were fit to the experimental data for different β^f ratios of each material system. Table 4.5 shows the reinforcement ratio of each material system. Figure 4.7 shows the S-N curves differentiated by the β^f. The fatigue performance of strengthened specimens are a function of the β^f ratio. The diagrams confirm that FRCM systems with higher β^f ratios had a superior fatigue performance compared the ones with lower β^f. The reason for this behavior appears to be the steel performance, not in changing its fundamental characteristics, but by decreasing the maximum stress that steel experiences with increasing the β^f. The latter is not intentional, but it is the result of conservatism in the analytical approach. The AC434 test methods result in underestimated characterization values, so the stress in steel from section analysis is higher than the actual stress value that steel undergoes during the experiments.

Fatigue thresholds of four FRCM systems in the three joint studies are summarized in Table 4.5. All these specimens have reached two million cycles of loading without failure, and maintained their integrity with minor residual stress loss. As before, the DNFS is the FRCM normalized design stress, which can be compared to the normalized ACI 549.4R-13 fatigue stress limits. From the table, ACI FRCM fatigue limits are safe to use.

Table 4.5: Fatigue threshold summary

Fabric Type	β^f [%]	**Peak PSY**	**DNFS**	**DNFE**	**Residual/ Exp. Load**	**ACI 549.4R-13 * Stress Limits**
AR Glass	1.1	65	0.49	0.23	0.91	0.2
C200 Carbon	1.8	65	0.62	0.22	0.99	0.55
C600 Carbon	6.3	65	0.37	0.18	0.95	0.55
PBO	5.1	75	0.40	0.16	0.99	0.3

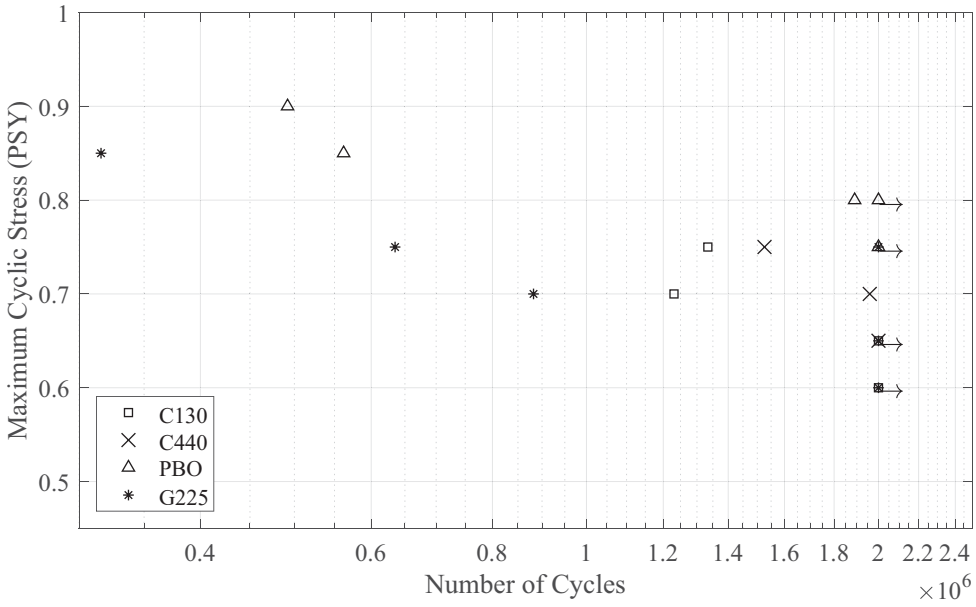

Figure 4.6: S-N curves for FRCM strengthened RC beams

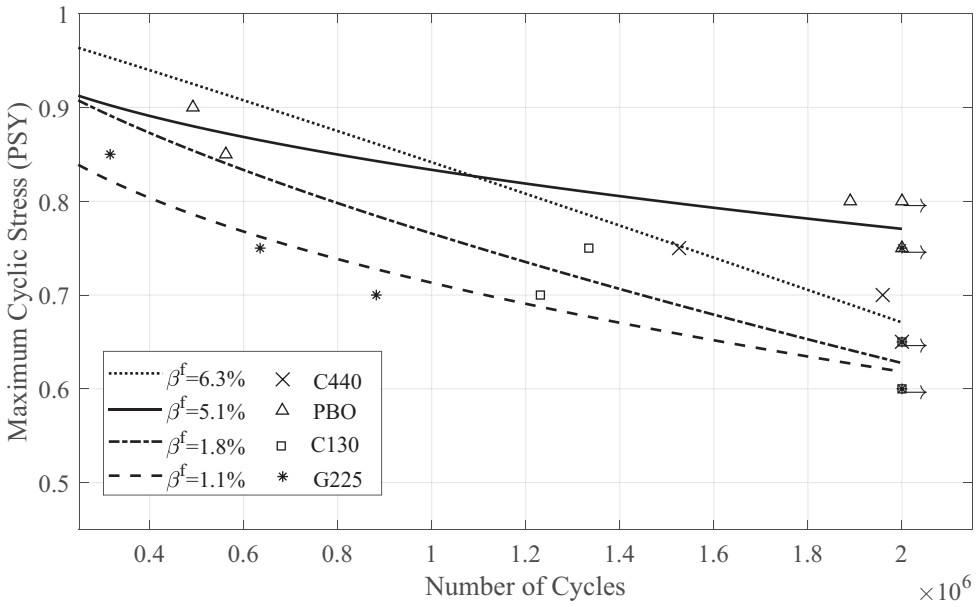

Figure 4.7: Effect of reinforcement ratio on fatigue behavior of FRCM-strengthened RC beams

4.5 Conclusion

The experimental work presented in this chapter investigates the fatigue behavior of carbon and glass FRCM strengthened RC beams. The FRCM characteristic values were investigated in Chapter 2, and the mechanical performance of FRCM strengthened RC beams identical to use used in the fatigue study were discussed in Chapter 3.

Fatigue endurance limit of the carbon and glass FRCM strengthened beams were 65 PSY, regardless of the β^f factor. Residual stress of the carbon and glass FRCM strengthened beams that endured two million cycles of loading retained at least 95% and 91% of the monotonically tested benchmarks.

Fatigue failure of strengthened and unstrengthened beams was due to fatigue fracture in the reinforcing steel bars and the FRCM fabrics did not suffer from fatigue loading. FRCM strengthened beams had an extended fatigue life compared to the control specimens.

The design and theoretical stresses and strains at FRCM were calculated for each specimen.

The S-N curves suggest that performance of FRCM strengthened RC beams depends on the β^f ratio, in which higher reinforcement ratios showed superior fatigue performance. This performance improvement was not intentional, but it might be the result of conservatism in the analytical approach and FRCM material characterization.

This study concludes that under cyclic fatigue loading, the ACI 549.4R-13 stress limits are safe to use for FRCM, however, the stress limitation in steel rebars is not safe to use and needs to be reconsidered.

Chapter 5

Conclusions

This dissertation deals with FRCM and SRG composites as a potential externally bonded strengthening and rehabilitation solution for RC structures including the transportation infrastructure.

Material characteristics of FRCM and SRG composites were investigated in Chapter 2. Various FRCM and SRG systems were tested in accordance with AC434 acceptance criteria. Failure modes and effects of fabric layers, specimen width, fabric architecture, and test setup on mechanical properties were discussed.

The failure mechanism of FRCM and SRG were distinctly different. The FRCM systems failed due to fabric slippage. Therefore, the quality of bond between the fabric and the matrix governed the FRCM tensile properties. SRG systems failed when a fracture surface at the fabric-matrix interface was formed due to shear stresses. Thus, SRG characteristics depended mainly on the matrix performance. Increasing the fabric area, which increased the shear stresses at the fabric-matrix interface, significantly reduced the tensile strength of the tested SRG systems. The results suggest that although FRCM and SRG systems are similar as a technology,

there are distinct differences in their mechanical performance.

Tensile strength and modulus of elasticity of tested FRCM specimens were reduced by increasing number of fabric layers. Therefore, material properties based on tests conducted on one-layer specimens are not necessarily representative of multiple-layer configurations, which should be taken into account in the acceptance criteria and design guidelines.

Two different acceptance methods were compared to characterize FRCM/SRG materials. The ultimate strength values provided by the two methods coincided for the carbon FRCM, which failed due to fabric slippage also in the bond test. On the other hand, the different boundary conditions applied in tensile tests generally led to a lower tensile modulus of elasticity and to a higher ultimate strain obtained from the clevis-grip test with respect to the clamping-grip one.

Performance of FRCM and SRG strengthened RC beams and slabs was studied in Chapter 3. First, FRCM/SRG characteristics from Chapter 2 were used to analytically predict the yielding and ultimate strengths of the RC beams and slabs according to ACI 549.4R-13.

It appears that there is an almost linear relation between the reinforcement ratio β^f and increase in the ultimate capacity of the RC members, which is an important factor for design purposes.

Specimens were tested under monotonic loading. The increase in ultimate strength from experiments were in good agreement with the analytical results. The failure sequence of the strengthened specimens (from analysis and experiments) was yielding of steel rebar in tension, debonding of FRCM/SRG, and concrete crushing. The FRCM debonding was at the matrix-fabric interface with high interfacial

slippage for glass FRCM, internal delamination for carbon FRCM, and debonding at substrate-matrix or fabric-substrate for SRG strengthened specimens.

The experimental and analytical results of strengthened RC slabs in this study showed that for a constant β^f ratio, the percentage of increase in the ultimate capacity of the strengthened specimens was almost constant, regardless of beam's geometry.

Fatigue behavior of carbon and glass FRCM strengthened RC beams were investigated in the last chapter. Analytical and experimental results of strengthened RC beams from Chapter 2 were used as benchmarks for fatigue studies.

Fatigue life of FRCM strengthened beams was 65 PSY, regardless of the β^f factor and FRCM type. Residual stress of the FRCM strengthened beams after two million cycles of loading showed minor loss (thus, minor damage) in ultimate strength.

Fatigue fracture in steel rebars was the governing failure mode. FRCM strengthened beams had an extended fatigue life compared to the control specimens.

Experimental results suggest that performance of FRCM strengthened RC beams depends on the β^f ratio, in which higher reinforcement ratios showed superior fatigue performance. This performance improvement was not intentional, but it might be the result of conservatism in the analytical approach and FRCM material characterization.

Design Implications

Currently, ACI 549.4R-13 document deals only with FRCM, and does not include SRG. The difference in behavior of FRCM and SRG systems must be ac-

knowledged and accounted for in future design guidelines.

Increasing number of fabric layers adversely affected the tensile characteristics of the tested FRCM system, which should be accounted in the acceptance criteria and design guidelines.

The relation between β^f ratio and increase in ultimate capacity helps the licensed design professional (LDF) to estimate the strengthened ultimate capacity, without knowing the specific FRCM/SRG system. The latter is necessary to design a project, in which the material providers are not usually known at the design phase.

Finally, the fatigue threshold of 65 PSY for FRCM strengthened RC beams proves that the service limits of steel rebars in ACI 549.4R-13 are not safe to use, and must be reduced according to the experimental results. FRCM stress limitations in ACI 549.4R-13 are validated by the analytical and experimental results of this study.

Future Work

The effect of number of fabric layers on FRCM material characteristic was studied for one FRCM system. This subject can be further studied to include the SRG and other FRCM types (e.g., carbon, PBO, etc). The results can be expressed in terms of reduction coefficients as a function of number of layers for each material type. These reduction coefficients will have meaningful design implications. It is also critical to study the other parameters that can affect FRCM/SRG material characterization, such as bond length of FRCM/SRG in test method per AC434.

In studying the structural performance of FRCM/SRG strengthened RC beams, cross section analysis based on the equilibrium of forces was conducted. More advanced numerical and analytical methods can be used in material characterization

and structural analysis to predict the behavior of FRCM/SRG strengthened RC beams.

The durability of the FRCM/SRG were not within the scope of this study, nevertheless, the durability of the FRCM/SRG systems need further investigation. The glass FRCM could potentially degrade in the alkaline environments and the steel wires of the SRG fabrics might rust. The corrosion of the SRG fabrics is of great concern mainly because of the relatively small cross section of single wires which are placed in a cementitious matrix with overall thickness of roughly half an inch. Therefore, the use of SRG in corrosion prone applications (i.e., the saltwater splashing zone, or subject to deicing agents) needs to be carefully studied and potentially limited. Moreover, the freeze/thaw degradation of the FRCM/SRG composites becomes important since an appealing application of these composites are the highway bridges. Therefore, the material characterization must include the air content and cyclic freeze/thaw tests.

APPENDICES

Appendix A

AC434

ICC EVALUATION SERVICE
Most Widely Accepted and Trusted

www.icc-es.org | (800) 423-6587 | (562) 699-0543 *A Subsidiary of the International Code Council®*

ACCEPTANCE CRITERIA FOR MASONRY AND CONCRETE STRENGTHENING USING FABRIC-REINFORCED CEMENTITIOUS MATRIX (FRCM) AND STEEL REINFORCED GROUT (SRG) COMPOSITE SYSTEMS

AC434

Approved June 2016

Compliance Date January 15, 2017

Previously approved August 2014, February 2013, October 2011

(Previously editorially revised December 2015)

PREFACE

Evaluation reports issued by ICC Evaluation Service, LLC (ICC-ES), are based upon performance features of the International family of codes. (Some reports may also reference older code families such as the BOCA National Codes, the Standard Codes, and the Uniform Codes.) Section 104.11 of the *International Building Code*® reads as follows:

> **The provisions of this code are not intended to prevent the installation of any materials or to prohibit any design or method of construction not specifically prescribed by this code, provided that any such alternative has been approved. An alternative material, design or method of construction shall be approved where the building official finds that the proposed design is satisfactory and complies with the intent of the provisions of this code, and that the material, method or work offered is, for the purpose intended, at least the equivalent of that prescribed in this code in quality, strength, effectiveness, fire resistance, durability and safety.**

This acceptance criteria has been issued to provide interested parties with guidelines for demonstrating compliance with performance features of the codes referenced in the criteria. The criteria was developed through a transparent process involving public hearings of the ICC-ES Evaluation Committee, and/or on-line postings where public comment was solicited.

New acceptance criteria will only have an "approved" date, which is the date the document was approved by the Evaluation Committee. When existing acceptance criteria are revised, the Evaluation Committee will decide whether the revised document should carry only an "approved" date, or an "approved" date combined with a "compliance" date. The compliance date is the date by which relevant evaluation reports must comply with the requirements of the criteria. See the ICC-ES web site for more information on compliance dates.

If this criteria is a revised edition, a solid vertical line (|) in the margin within the criteria indicates a change from the previous edition. A deletion indicator (→) is provided in the margin where any significant wording has been deleted.

ICC-ES may consider alternate criteria for report approval, provided the report applicant submits data demonstrating that the alternate criteria are at least equivalent to the criteria set forth in this document, and otherwise demonstrate compliance with the performance features of the codes. ICC-ES retains the right to refuse to issue or renew any evaluation report, if the applicable product, material, or method of construction is such that either unusual care with its installation or use must be exercised for satisfactory performance, or if malfunctioning is apt to cause injury or unreasonable damage.

Acceptance criteria are developed for use solely by ICC-ES for purposes of issuing ICC-ES evaluation reports.

Annex A
Tensile Testing of Fabric-reinforced Cementitious Matrix (FRCM) and Steel Reinforced Grout (SRG) Composite Specimens

A1.0 Summary of Test Method

A thin flat strip of material having a near-constant rectangular cross section is mounted in the grips of a mechanical testing machine and loaded with monotonically increasing load in tension while recording load and displacement. The ultimate strength of the material can be determined from a maximum load carried before failure. The coupon strain or elongation is monitored with displacement transducers to determine the nominal stress-strain response of the material, and from that the cracking stress and strain, ultimate tensile strain, tensile modulus of elasticity before and after cracking of cement-based matrix can be derived.

This test procedure is designed to produce tensile property data for material specifications, quality assurance, and structural design and analysis. Factors that influence the tensile response and shall therefore be reported include the following: material, methods of material preparation and lay-up, specimen preparation, specimen conditioning, environment of testing, specimen alignment and gripping, and speed of testing. Properties, in the test direction, which may be obtained from this test include:

1. Ultimate tensile strength
2. Ultimate tensile strain
3. Tensile modulus of elasticity of uncracked specimen
4. Tensile modulus of elasticity of cracked specimen
5. Transition point

Attention shall be paid to material and specimen preparation, gripping, and test system alignment. Poor material fabrication practices, lack of control in alignment of fiber grid, and damage induced by improper cutting and machining the coupons are known causes of high material data scatter. Specimen gripping problems can also cause a high percentage of grip-influenced failures and therefore more scatter in data. Every effort shall be made to eliminate excess bending due to system misalignment and out-of-tolerance conditions caused by poor specimen preparation.

A2.0 Apparatus

A2.1 Dimension Measurements: The accuracy of instruments used for measuring dimensions of the test specimens shall be suitable for reading to within 1 percent of the sample dimensions.

A2.2 Testing Machine: The testing machine shall be in conformance with Practices ASTM E4. The testing machine shall have both an essentially stationary head and a movable head. The drive mechanism shall be capable of imparting to the movable head a controlled velocity with respect to the stationary head. The testing machine load sensing device shall be able to indicate the applied load to the specimen within 1 percent of the indicated value. Each head of the testing machine shall carry one grip for holding the test specimen in coincident with the longitudinal axis of the specimen. It is desirable to use grips that are rotationally self-aligning to minimize bending stresses in the coupon.

A2.3 Gripping mechanism: Clevis-type grips shall be used to transfer the load from the testing machine to the specimen. At least one of the two grips (preferably the top one) shall allow for rotation in two perpendicular planes. No clamping force (i.e., pressure exerted on the tabs) should be applied to the specimen during testing. An illustration depicting the gripping mechanism with typical specimen dimensions is shown in Figure A1.

A.2.4 Strain Indicating Device: An extensometer satisfying Practice ASTM E83, Class B-1 requirements can be used for strain/elongation measurement. A minimum gage length of 2 inches (50 mm) shall be used. Since the coupon undergoes cracking in the early stages of loading, the gage length shall be adequate to at least include within itself one transverse crack. The bearing points of the extensometer on the coupon shall not be disturbed by cracking. If cracking occurs at the bearing points, the specimen shall be unloaded and extensometer moved. The discontinuity in elongation reading can be removed in data reduction process by matching the stop and restart point or similar means. The weight of extensometer shall not cause significant bending in the specimen.

A3.0 Test Specimens

At least ten (no conditioning) and five (conditioned) specimens shall be tested per test condition. Specimens can be cut from larger panels laid up in special molds. Control of fiber grid alignment is critical in lay-up procedure. Effective cutting tools and methods need to used, and precautions shall be taken to avoid notches, undercuts, uneven surfaces, or delaminations. The specimen preparation method shall be reported. Specimens shall be labeled properly to be distinct from each other and traceable to the raw material.

The test specimens shall be rectangular coupons. The thickness of coupons shall be as required and be a function of number of layers and thickness of matrix for each layer. The width of the coupon shall be adequate to include a minimum number of strands (e.g., three (3) strands in each layer) and shall not be less than four times the thickness of the specimen. The width shall also be kept as a multiple of the grid spacing. Also, in case the strands in different layers are staggered with respect to each other, it is preferable to have the same number of strands in each layer along the width of the coupon. The

minimum length of the coupon shall include gripping distance, plus twice the width plus gage length. Longer lengths are preferred to minimize the bending effects on the specimen.

Metallic tabs (e.g., steel, aluminum) are recommended to avoid damage to the specimen by the clevis-type grips. The tabs can be glued to the specimen ends (two at each end, one at each face). The tabs shall have the same width as the coupon. The tab length can be calculated based on the maximum expected tensile load, glue and tab bond strength to the matrix, and development length of the fiber strands within matrix. A minimum of 4 inches (101 mm) tab length is recommended. The thickness of the tabs shall be adequate to distribute uniformly the gripping force to the overall width of the coupons. A minimum thickness of $^1/_{16}$ inch (2 mm) is recommended.

The tensile specimen must have sufficient fabric area to achieve 50 percent strength over transition point (so that the $0.6f_{fu}$ and $0.9f_{fu}$ will be in the correct part of the curve)

A4.0 Calibration

The accuracy of all measuring equipment shall have certified calibrations that are current at the time of use of the equipment.

A5.0 Conditioning

Unless a different environment is specified as part of the experiment, test specimens shall be moist cured at least for seven days after lay-up, and another seven days at laboratory environment before testing. Tests can be conducted at 14-day age and later. Storage after curing and testing shall be at standard laboratory atmospheric conditions.

A6.0 Procedure

After conditioning and before testing, coupon type and geometry and environmental conditioning test parameters are specified. The overall cross-sectional area of the specimen is calculated as follows:

$$A = w_s\, h_s \tag{A1}$$

where w_s is the nominal width and h_s is the nominal thickness of the coupon. The width and thickness are measured at three locations along the specimen and averaged. This value is determined for reporting purposes only. For computation of FRCM/SRG mechanical properties, the area of grid reinforcement by unit width, A_f measured in.^{2}/in (mm^2/mm), as reported by the manufacturer, is used.

Special tabs prepared for installation are glued to the specimen. The glue shall be permitted to cure per applicant instruction. The specimen placed in the clevis-type grips of testing machine, taking care to align the axis of the gripped specimen with the test direction. An initial minimal tension, less than 5 percent of the anticipated failure load, is applied to straighten potential bow in the specimen. The displacement transducer is attached to the specimen, preferably symmetrically about the mid-span, mid-width location. The load is applied under displacement control. The loading rate can be adjusted by the velocity of the machine head. A standard rate of 0.01 in./min (0.2 mm/min) is recommended.

The load versus displacement shall be recorded continuously or at frequent regular intervals. The load, displacement, and mode of cracking (or any other damage) during testing that would cause transition region in otherwise a linear response are recorded. Cracks may occur at regular spacing along the specimen. If the cracks intercept the transducer bearing points, the specimen shall be unloaded to the level of the initial loading. The displacement transducer shall then be slightly moved and reinstalled to bear at uncracked region of the matrix. Reload the specimen with the same rate of loading and continue data recording. The displacement transducer shall be removed before anticipated failure to avoid damage to the sensor, but load readings shall continue until failure. The maximum load, the failure load, and corresponding displacements at, or as near as possible to, the moment of rupture shall be recorded, along with the failure mode and location.

A7.0 Calculation

The recorded data shall be reduced to reflect the initial tensile loading and reading discontinuity if the transducer were to be moved during the test. This will likely result in a near bilinear response curve (Figure A2) with an initial line for uncracked specimen, a secondary line for cracked specimen, and possibly a curved transition segment in between.

A7.1 Expected Tensile Stress – Strain Curve: The expected tensile stress, f_f, versus tensile strain, ε_f, curve of an FRCM/SRG coupon specimen is shown in Figure A2. If a curved segment exist in between two linear portions of the response curve, the two lines to initial and secondary segments of the response curve shall be continued until they intersect. The displacement and load corresponding to the intersection are calculated as the transition point data, named T in Figure A2.

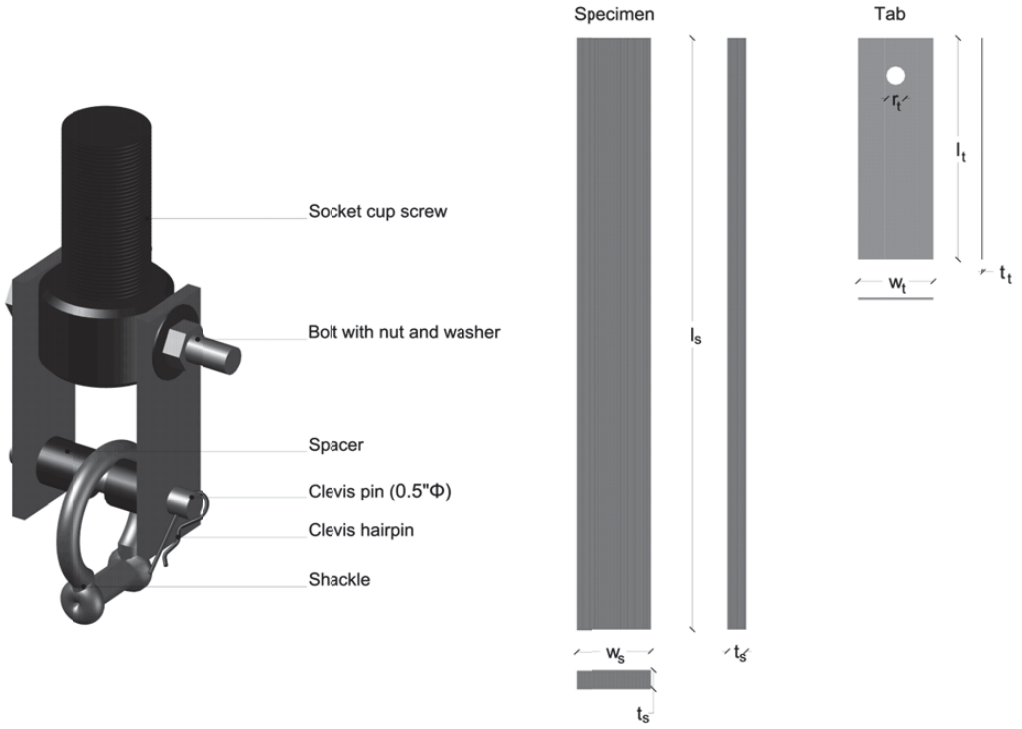

FIGURE A1—GRIPPING MECHANISM AND TYPICAL SPECIMEN DIMENSIONS

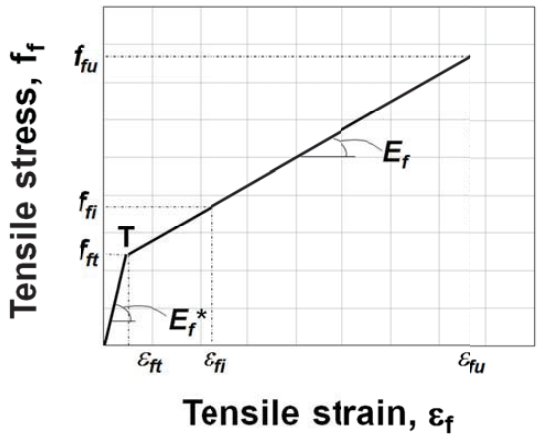

FIGURE A2—EXPECTED TENSILE STRESS VERSUS TENSILE STRAIN CURVE OF AN FRCM/SRG COUPON SPECIMEN. THE TRANSITION POINT (T) IS INDICATED

In Figure A2 the following quantities are shown:

E_f = tensile modulus of elasticity of the cracked specimen, psi (MPa)

E_f^* = tensile modulus of elasticity of the uncracked specimen, psi (MPa)

f_{fi} = tensile stress at *i*th data point, psi (MPa)

f_{fu} = ultimate tensile strength, psi (MPa)

f_{ft} = tensile stress corresponding to the transition point, psi (MPa)

ε_{fi} = tensile strain at *i*th data point, in./in. (mm/mm)

ε_{fu} = ultimate tensile strain, in./in. (mm/mm)

ε_{ft} = tensile strain corresponding to the transition point, in./in. (mm/mm)

A7.2 Transition Point (T): If a curved segment exist in between two linear portions of the response curve, the two lines to initial and secondary segments of the response curve shall be continued until they intersect. The displacement and load corresponding to the intersection are calculated as the transition point data.

A7.3 Tensile Stress/Tensile Strength: The ultimate tensile strength and, if needed, the tensile stress at a specific data point are calculated using the following equations:

$$f_{fu} = P_{max} / (A_f, w_s) \quad \text{(A2)}$$

$$f_{fi} = P_i / (A_f\, w_s) \quad \text{(A3)}$$

where:

P_{max} = maximum load before failure, lbf (N).

P_i = load at *i*th data point, lbf (N).

A_f = area of grid reinforcement by unit width, $in.^2$/in (mm^2/mm), as provided by the manufacturer.

w_s = nominal width of the specimen , in. (mm)

$A_f w_s$ = a) calculate the number of strands per unit width, foot (meter), of fabric based on strand spacing;

b) determine the area of each strand, A_{fj} , based on A_f as provided by the manufacturer;

c) recompute A_f, w_s as the product of the A_{fi} *n, where n is the number of strands effectively present in the width of the coupon.*

A7.4 Tensile Strain: Tensile strain at a specific data point is calculated using the following equation:

$$\varepsilon_{fi} = \delta_i / L_g \quad \text{(A4)}$$

where:

δ_i = extensometer displacement at *i*th data point, in. (mm).

L_g = extensometer gage length, in. (mm).

A7.5 Tensile Modulus of Elasticity of Uncracked Specimen: On the linear segment of the initial line of the response bilinear curve corresponding to uncracked behavior of the specimen two points connecting the results in a line that closely follows the trend and slope of the response curve at that region are selected. The tensile modulus of elasticity of the uncracked specimen is calculated using:

$$E_f^* = \Delta f / \Delta\varepsilon \quad \text{(A5)}$$

where:

Δf = difference in tensile stress between two selected points, psi (MPa).

$\Delta\varepsilon$ = *difference in tensile strain between two selected points, in/in (mm/mm).*

Alternatively, the slope of the initial line passing through the origin and drawn to obtain the transition point on the response curve can be calculated as the modulus of elasticity of uncracked specimen.

A7.6 Tensile Modulus of Elasticity of Cracked Specimen: On the segment of the response curve corresponding to cracked behavior after the transition as defined in Section A7.2, two points are selected on the experimental curve at a stress level equal to $0.90f_{fu}$ and $0.60f_{fu}$[1]. The slope of the line that connects these two points represents the tensile modulus of elasticity at that region:

$$E_f = \Delta f / \Delta\varepsilon = (0.90f_{fu} - 0.60f_{fu}) / (\varepsilon_{f@0.90ffu} - \varepsilon_{f@0.60ffu}) \quad \text{(A6)}$$

[1] The experimental stress-strain curve is typically jagged and intersects with horizontal lines at values of $0.90f_{fu}$ and $0.60f_{fu}$ may occur more than once. In this instance, the first $0.90f_{fu}$ and the last $0.60f_{fu}$ intersects are the ones selected for the computation of E_f.

A7.7 Ultimate Tensile Strain: Ultimate tensile strain, ε_{fu}, is by obtaining the y-intercept of the line used to compute E_f as defined in A7.6 (i.e., $y_{intercept} = 0.60f_{fu} - E_f\,\varepsilon_{f@0.60ffu}$) and the following equation:

$$\varepsilon_{fu} = (f_{fu} - y_{intercept}) / E_f \qquad \text{(A7)}$$

A8.0 Report

The following information shall be reported to the maximum extent applicable:

- Date and location of the test
- Name of test operator
- Any variations to this test method
- Identification of the material tested including material specification, type, and designation, manufacturer
- Description of the fabrication steps used to prepare the composite material including fabrication date, process, cure cycle, and description of equipment used
- Orientation of the fiber grid
- Area of grid reinforcement by unit width and nominal cross-section area of all specimens
- Method of preparation of test specimen including labeling system, geometry, sampling method, cutting, tab identification, geometry and adhesive used
- Calibration information for all measurement and test equipment
- Description of the test machine
- Conditioning parameters and results
- Temperature and humidity of testing laboratory
- Number of specimens tested
- Speed of testing
- Type and placement of transducers on the test specimens
- Stress-strain curve and tabulated results
- Individual strengths, average, standard deviation, and coefficient of variation (in percent) for the population
- Individual strains at failure and average, standard deviation, and coefficient of variation (in percent) for population
- Strains used for modulus calculation
- Describe the method used for calculation of the moduli of elasticity
- Individual moduli of elasticity and average, standard deviation, and coefficient of variation (in percent) for population
- If transition strain is determined, describe the method of linear fit
- Individual values of transition strains and average, standard deviation, and coefficient of variation (in percent) for population
- Failure mode and location of failure for each specimen.

Appendix B

Section Analysis

RC Beam Strengthened with G600-G0-S

Define beam geometry and concrete properties

Geometry

$b := 6in$ Beam width

$h := 12in$ Beam height

$L_0 := 5ft$ Beam length

$c_c := 1.25in$ Clear concrete cover at bottom

$c'_c := 1.25in$ Clear concrete cover at top

Concrete properties

$\varepsilon_{cu} := 0.003$ Ultimate compressive strain

$\rho_c := 145 \frac{lbf}{ft^3}$ Density

$w_{dl} := \rho_c \cdot b \cdot h = 72.5 \cdot plf$ Dead load per foot of concrete

$M_0 := \frac{w_{dl} \cdot L_0^2}{8} = 2.7187 \cdot kip \cdot in$ Dead Load Moment

$f'_c := 5859psi$ Compressive strength

$E_c := 33psi^{0.5} \left(\frac{\rho_c}{lbf \cdot ft^{-3}} \right)^{1.5} \cdot \sqrt{f'_c}$ Compressive modulus of elasticity (ACI 318-14)

$E_c = 4410\,ksi$

$f'_{ct} := 7.5 \cdot \sqrt{f'_c \cdot psi} = 0.57 \cdot ksi$ Tensile strength (ACI 318-14)

Analytical Approximations to the Compressive Stress-Strain Curve

Todeschini's Model

$\varepsilon_{c0} := \frac{1.71 \cdot f'_c}{E_c} = 0.0023$ Compressive strain at peak

$\sigma''_c := 0.9 \cdot f'_c = 5273.1 \cdot psi$ Compressive stress at peak

$\sigma_c(\varepsilon_c) := \frac{2 \cdot \sigma''_c \cdot \left(\frac{\varepsilon_c}{\varepsilon_{c0}}\right)}{1 + \left(\frac{\varepsilon_c}{\varepsilon_{c0}}\right)^2}$ Stress-strain curve equation

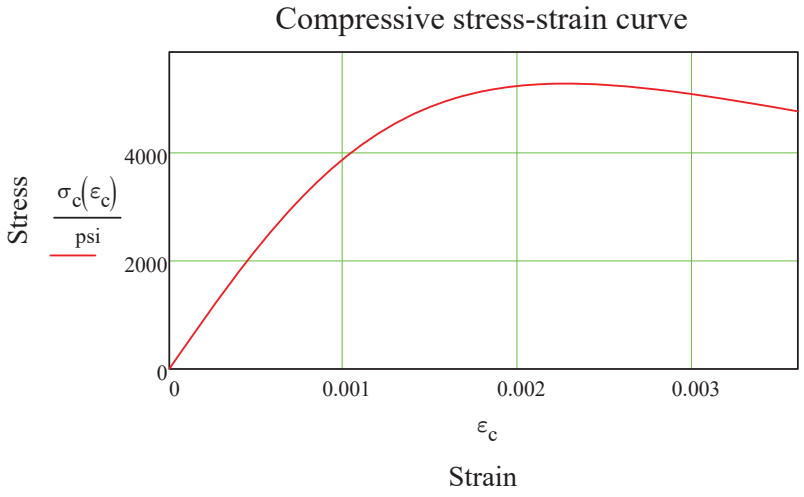

Define Internal and External Reinforcement Properties

US steel reinforcement

Legend

Area (in^2)
Weight (lbf/ft)
Diameter (in)

$cb := 0 .. 2$ $rb := 0 .. 11$ $Bar_{rb,cb} := 0.0$ Counters definition

$Bar_{3,cb} := Bar_{4,cb} := Bar_{5,cb} := Bar_{6,cb} := Bar_{7,cb} := Bar_{8,cb} := Bar_{9,cb} := Bar_{10,cb} := Bar_{11,cb} :=$

0.11	0.2	0.31	0.44	0.6	0.79	1.00	1.27	1.56
0.376	0.668	1.043	1.502	2.044	2.67	3.4	4.303	5.313
0.375	0.5	0.625	0.75	0.875	1.0	1.128	1.27	1.41

Secondary Shear Reinforcement Properties

$\Phi_v := 0.252in$ Stirrup diameter

$s_v := 5in$ Stirrup spacing

$f_{yt} := 75ksi$ Yield strength

$A_v := 2 \cdot \pi \cdot \frac{\Phi_v^2}{4} = 0.0998\,in^2$ Area of transversal steel reinforcement

$$A_{vmin} := \max\left(0.75 \cdot \sqrt{\frac{f'_c \cdot 1000}{ksi}} \cdot b \cdot \frac{s_v}{\frac{f_{yt} \cdot 1000}{ksi}}, 50 \cdot b \cdot \frac{s_v}{\frac{f_{yt} \cdot 1000}{ksi}}\right) = 0.02\,in^2$$

Internal Steel Reinforcement Properties

$BarSize := 3$ i.e. #3 bar

$n_{bar} := 3$ Number of bars

$f_y := 75ksi$ Specified yield strength of reinforcement steel

$E_s := 29000ksi$ Tensile modulus of elasticity of reinforcement steel

$\Phi_s := Bar_{BarSize,2}\,in = 0.375\,in$ Bar diameter

$A_s := n_{bar}\,Bar_{BarSize,0} \cdot in^2 = 0.33\,in^2$ Area of longitudinal steel reinforcement

$d := h - c_c - \Phi_v - \frac{\Phi_s}{2} = 10.31\,in$ Distance from extreme compression fiber to centroid of tension reinforcement

$\varepsilon_{sy} := \frac{f_y}{E_s} = 0.00259$ Yield tensile strenght of the reinforcement steel

$\varepsilon_{sh} := 0.01$ Hardening strain

$\varepsilon_{sd} := 0.02$ Design Strain (I used a larger value than yield)

$\varepsilon_{su} := \varepsilon_{sd}$

$n_s := \frac{E_s}{E_c} = 6.6$ Ratio of steel to concrete modulus

Internal Compressed Steel Reinforcement Properties

$BarSize' := 3$

$n'_{bar} := 2$

$\Phi' := Bar_{BarSize',2}\,in = 0.375\,in$ Bar diameter

$A'_s := n'_{bar}\,Bar_{BarSize',0}\cdot in^2 = 0.22\,in^2$ Area of longitudinal steel reinforcement

$d' := c'_c + \Phi_v + \frac{\Phi'}{2} = 1.7\,in$ Distance from extreme compression fiber to centroid of tension reinforcement

Analytical approximations to the tensile stress-strain curve

$$f_s(\varepsilon_s) := \begin{cases} E_s\cdot\varepsilon_s & \text{if } \varepsilon_s < \varepsilon_{sy} \\ f_y & \text{if } \varepsilon_{sy} \le \varepsilon_s \le \varepsilon_{sh} \\ \frac{110ksi - f_y}{0.075 - \varepsilon_{sh}}\cdot(\varepsilon_s - \varepsilon_{sh}) + f_y & \text{if } \varepsilon_{sh} < \varepsilon_s \end{cases}$$

Stress-strain curve equation with strain hardening - per experimental tests.

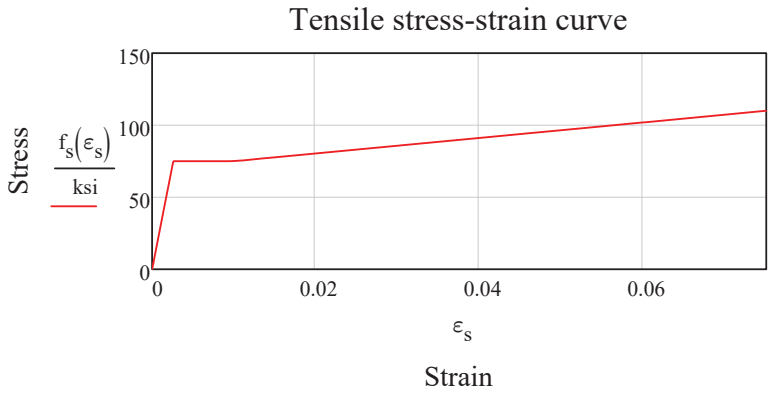

FRCM Material Properties:

Modulus of Elasticity from characterization	$E_f := 89.49GPa = 12979.43 \cdot ksi$
Ultimate Design Stress from characterization tests	$f_{fu} := 1381.4MPa = 200.36\,ksi$
Ultimate Design Strain from characterization	$\varepsilon_{fd} := 0.0123$
Strain Used in the Analysis	$\varepsilon_{fe1} := \min(\varepsilon_{fd}, 0.012) = 0.012$
Number of plies	$n := 1$
Area of FRCM mesh by unit length	$A_{f.unit} := 84\frac{mm^2}{m} = 0.0033\,in \cdot \left(\frac{in}{in}\right)^2$
Ply Width	$b_f := b = 6\,in$
Area1 of FRCM	$A_f := b_f \cdot A_{f.unit} \cdot n = 0.0198\,in^2$
Distance to center of Area 1 of FRCM	$d_f := h = 12\,in$

Reinforcement Ratio Analysis:

$$\beta_1 := .85 - .005 \cdot \left(\frac{f'_c - 4000psi}{1000psi}\right) = 0.8407$$

Balanced Steel Ratio $\rho_b := .85 \cdot \frac{f'_c}{f_y} \cdot \beta_1 \cdot \frac{\varepsilon_{cu}}{\varepsilon_{cu} + \varepsilon_{sy}} = 0.03$

Balanced $E_s \cdot \rho_b$ $E_s \cdot \rho_b = 869.4148\,ksi$

Actual Steel Ratio $\rho_s := \frac{A_s}{b \cdot d} = 0.0053$ much less than ρ_b

Actual $E_s \cdot \rho_b$ $E_s\,\rho_s = 1066.596 \cdot MPa$

$$\frac{E_s \rho_s}{E_s \cdot \rho_b} = 17.7932 \cdot \%$$

Actual FRCM Ratio $\rho_f := \frac{A_f}{b \cdot h} = 0.0003$

Actual $E_f \rho_f$ $E_f \rho_f = 24.6626 \cdot MPa$

Total $E\rho$ $E\rho := E_s \rho_s + E_f \rho_f = 158.2737\,ksi$

Increase $\frac{E\rho}{(E_s \cdot \rho_b)} = 18.2046 \cdot \%$ $\frac{E_f \rho_f}{E_s \rho_s} = 2.3123 \cdot \%$

Analytical approximations to the tensile stress-strain curve

$f_{fi}(\varepsilon_{fi}) := E_f \cdot \varepsilon_{fi}$ Stress-strain curve equation

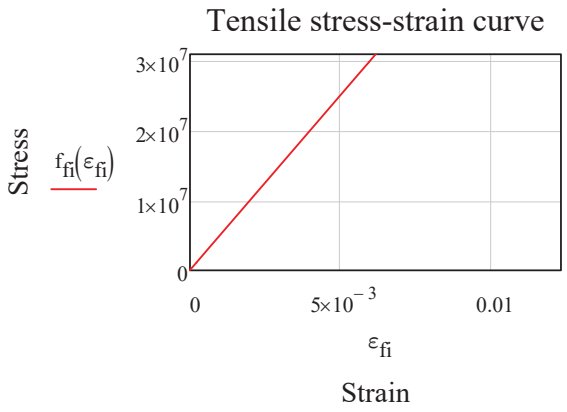

$n_f := \frac{E_f}{E_c} = 2.9$ Ratio of modulus of elasticity of FRP Reinforcement to modulus of elasticity of concrete

Calculate Strain in Each Material to Determine the Neutral Axis Location and Failure Mode

Effective level of strain in the FRCM reinforcement

$$\varepsilon_c(x) := \begin{cases} \varepsilon_{cu} \text{ if } \varepsilon_{cu} < \dfrac{\varepsilon_{sd} \cdot x}{(d - x)} \\ \dfrac{\varepsilon_{sd} \cdot x}{d - x} \text{ if } \left[\dfrac{\varepsilon_{sd} \cdot x}{(d - x)} < \varepsilon_{cu}\right] \end{cases}$$

$\varepsilon_{su} = 0.02$

$\varepsilon_{fe1} = 0.012$

$\varepsilon_{cu} = 0.003$

Strain in concrete

$$\varepsilon_{fe}(x) := \frac{(h - x)}{x} \cdot \varepsilon_c(x)$$

Strain in the reinforcing steel

$$\varepsilon_s(x) := \varepsilon_c(x) \cdot \left(\frac{d - x}{x}\right)$$

Strain in the compressed steel

$d' = 1.6895 \text{ in}$

$$\varepsilon'_s(x) := \varepsilon_c(x) \cdot \left(\frac{d' - x}{x}\right)$$

$$\sigma_s(x) := \begin{cases} E_s \cdot \varepsilon_s(x) \text{ if } \varepsilon_s(x) < \varepsilon_{sy} \\ f_y \text{ if } \varepsilon_{sy} \le \varepsilon_s(x) \le \varepsilon_{sh} \\ \dfrac{90.31\text{ksi} - f_y}{0.020 - \varepsilon_{sh}} \cdot \left(\varepsilon_s(x) - \varepsilon_{sh}\right) + f_y \text{ if } \varepsilon_{sh} < \varepsilon_s(x) \end{cases}$$

Stress level in the reinforcing steel

$$\sigma'_s(x) := \begin{cases} E_s \cdot \varepsilon'_s(x) \text{ if } \left|\varepsilon'_s(x)\right| < \varepsilon_{sy} \\ f_y \text{ if } \left|\varepsilon'_s(x)\right| \ge \varepsilon_{sy} \end{cases}$$

Stress level in the compressed steel

$$\sigma_f(x) := E_f \cdot \varepsilon_{fe}(x)$$

Stress level in the FRCM

Calculate the Internal Force Resultants and Check Equilibrium

$$\varepsilon_{c1}(x,y) := \frac{\varepsilon_c(x)}{\frac{x}{in}} y$$

Strain in concrete

$$C_c(x) := b \cdot \int_0^{\frac{x}{in}} \frac{2 \cdot \sigma''_c \cdot \left(\frac{\varepsilon_{c1}(x,y)}{\varepsilon_{c0}}\right)}{1 + \left(\frac{\varepsilon_{c1}(x,y)}{\varepsilon_{c0}}\right)^2} dy \cdot in$$

Compressive force in the concrete

$$T_{tot}(x) := \left(A_s \cdot \sigma_s(x) + A_f \cdot \sigma_f(x)\right) + \left(A'_s \cdot \sigma'_s(x)\right)$$

Tension force in the reinforcement

$$C_{tot}(x) := C_c(x)$$

Neutral Axis Location

Static equilibrium

$$f_1(x) := C_{tot}(x) - T_{tot}(x)$$

Input an anticipated value of neutral axis depth

$$x_{01} := 0.2 \cdot d$$

$$x_u := root\left(f_1\left(x_{01}\right), x_{01}\right)$$

Neutral axis depth

$x_u = 1.5\,in$ $\quad$ $d' = 1.69\,in$

Verify Neutral Axis Location

$T_{tot}\left(x_u\right) = 161.7 \cdot kN$

$C_{tot}\left(x_u\right) = 161.7 \cdot kN$

$Neutral_{Axis.Location} := if\left(\left|T_{tot}\left(x_u\right) - C_{tot}\left(x_u\right)\right| \le .0000001\,lbf, "OK", "Re-Evaluate"\right)$

$Neutral_{Axis.Location} = "OK"$

Determine Failure Type

$$\text{Failure}_{Type} := \begin{cases} \text{"Failure ConcCrush"} & \text{if } \varepsilon_{cu}\cdot\left(\frac{h - x_u}{x_u}\right) < \varepsilon_{fe1} \wedge \varepsilon_{cu}\cdot\left(\frac{h - x_u}{x_u}\right) < \varepsilon_{sd}\cdot\left(\frac{h - x_u}{d - x_u}\right) \\ \text{"Failure of Steel"} & \text{if } \varepsilon_{sd}\cdot\left(\frac{h - x_u}{d - x_u}\right) < \varepsilon_{fe1} \wedge \varepsilon_{sd}\cdot\left(\frac{h - x_u}{d - x_u}\right) < \varepsilon_{cu}\cdot\left(\frac{h - x_u}{x_u}\right) \\ \text{"Failure of FRCM"} & \text{otherwise} \end{cases}$$

$\text{Failure}_{Type} = \text{"Failure of FRCM"}$

$\varepsilon_{fe}(x_u) = 0.021$

Check yielding of steel

$\text{Yielding}_{steel} := \text{if}(\varepsilon_s(x_u) \geq \varepsilon_{sy}, \text{"YES"}, \text{"NO"})$

$\text{Yielding}_{steel} = \text{"YES"}$

$\varepsilon_t := \varepsilon_s(x_u) = 0.017579$

$\varepsilon'_s(x_u) = 0.0004$

$\varepsilon_c(x_u) = 0.003$

Determine Flexural Strength

$$M_n := A_s\cdot\sigma_s(x_u)\cdot(d - x_u) + A'_s\cdot\sigma'_s(x_u)\cdot(x_u - d') + A_f\cdot\sigma_f(x_u)\cdot(h - x_u) \ldots$$
$$+ b\cdot\int_0^{\frac{x_u}{in}} y\,\frac{2\cdot\sigma''_c\cdot\left(\frac{\varepsilon_{c1}(x_u, y)}{\varepsilon_{c0}}\right)}{1 + \left(\frac{\varepsilon_{c1}(x_u, y)}{\varepsilon_{c0}}\right)^2}\,dy\cdot in^2$$

$M_n = 38\cdot kN\cdot m$

$P_n := 4\cdot\frac{M_n}{L_0} = 100.98\cdot kN$

Appendix C

FRCM/SRG Characterization

Summary Tables

B200-L0-F

	Stress at Transition		Strain at Transition	Ultimate Strength		Ultimate Strain	Uncracked Modulus		Cracked Modulus	
	f_{ft}		ε_{ft}	f_{fu}		ε_{fu}	E*		Ef	
	[MPa]	[ksi]	%	[MPa]	[ksi]	%	[GPa]	[Msi]	[GPa]	[Msi]
	240.61	34.9	0.002989	679.33	98.5	0.87	389.58	56.50	50.64	7.34
	-	-	-	607.67	88.1	1.11	-	-	47.36	6.87
	314.80	45.7	0.003290	687.00	99.6	0.88	765.65	111.05	42.52	6.17
	213.04	30.9	0.006075	715.70	103.8	1.20	248.33	36.02	42.13	6.11
	-	-	-	654.11	94.9	0.57	475.00	68.89	46.31	6.72
	252.19	36.6	0.000337	655.07	95.0	2.15	232.17	33.67	43.65	6.33
	51.26	7.4	-	682.55	99.0	3.06	127.39	18.48	35.48	5.15
	-	-	-	633.69	91.9	2.34	-	-	46.59	6.76
	399.63	58.0	0.001332	727.52	105.5	2.20	241.87	35.08	40.83	5.92
	300.75	43.6	0.001321	570.16	82.7	1.73	180.59	26.19	59.79	8.67
Average	253.18	36.72	0.00256	661.28	95.91	1.61	332.57	48.24	45.53	6.60
S_{n-1}	108.05	15.67	0.00205	48.09	6.98	0.81	207.61	30.11	6.51	0.94
CV((%)	43	43	80	7	7	50	62	62	14	14
Min	51.26194	7.43488	0.00034	570.15586	82.69370	0.56600	127.38792	18.47606	35.47704	5.14551
Max	399.63235	57.96148	0.00607	727.52062	105.51741	3.05756	765.65412	111.04874	59.78706	8.67138

G250-L0-F

	Stress at Transition		Strain at Transition	Ultimate Strength		Ultimate Strain	Uncracked Modulus		Cracked Modulus	
	f_{ft}		ε_{ft}	f_{fu}		ε_{fu}	E*		Ef	
	[MPa]	[ksi]	%	[MPa]	[ksi]	%	[GPa]	[Msi]	[GPa]	[Msi]
	651.79	94.5	0.000260	1400.85	203.2	3.51	2,506.88	363.59	30.30	4.39
	839.80	121.8	0.000390	1250.75	181.4	2.82	2,153.33	312.31	33.68	4.88
	721.80	104.7	0.000500	1095.17	158.8	2.81	1,443.60	209.38	29.61	4.29
	736.21	106.8	0.000520	987.44	143.2	3.10	1,415.79	205.34	25.89	3.76
	913.95	132.6	0.000350	1279.26	185.5	2.68	2,611.29	378.73	34.19	4.96
	913.95	132.6	0.000350	1025.41	148.7	3.54	2,611.29	378.73	24.90	3.61
	653.59	94.8	0.000390	1276.34	185.1	3.32	1,675.87	243.06	28.39	4.12
	496.45	72.0	0.000120	966.96	140.2	3.38	4,137.08	600.03	27.96	4.06
	672.07	97.5	0.007820	1479.84	214.6	3.45	-	-	33.95	4.92
	583.42	84.6	0.000190	1010.19	146.5	2.12	3,070.63	445.36	37.40	5.42
Average	718.30	104.18	0.001089	1193.06	173.04	2.97	2402.86	348.51	31.17	4.52
S_{n-1}	137.36	19.92	0.002368	170.34	24.71	0.56	868.65	125.99	4.12	0.60
CV((%)	19	19	217	14	14	19	36	36	13	13
Min	496.45000	72.00362	0.00012	966.96	140.24	1.87	1415.79	205.34	24.90	3.61
Max	913.95000	132.55657	0.00782	1479.84	214.63	3.71	4137.08	600.03	37.75	5.48

C130-C2-F

	Transition point Strength		Strain	Ultimate Strength		Ultimate Strain	Modulus of Elasticity Cracked		Modulus of Elasticity Uncracked	
	MPa	ksi	%	MPa	ksi	%	GPa	Msi	GPa	Msi
	445	64.54	0.01	1200	174	1	78	11.25	6185	897
	420	60.92	0.01	1166	169	1.45	52	7.51	5551	805
	389	56.42	0.01	1039	151	1.05	87	12.62	7000	1016
	517	74.98	0.01	1182	171	1.2	55	7.98	5828	846
	548	79.48	0.01	1159	168	1.46	55	7.98	5002	726
Average	463.8	67.27	0.01	1149	167	1.23	65	9.47	5913	858
S_{n-1}	66.68	9.67	0	64	9	0.22	16	2.31	746	108
CV((%)	14.4	14.4	0	5.5	5.5	17.6	24.4	24.4	12.6	12.6
max	548	79.48	0.01	1200	174	1.46	87	12.62	7000	1016
min	389	56.42	0.01	1039	151	1	52	7.51	5002	726

C440-C2-F

	Transition point Strength		Strain	Ultimate Strength		Ultimate Strain	Modulus of Elasticity Cracked		Modulus of Elasticity Uncracked	
	MPa	ksi	%	MPa	ksi	%	GPa	Msi	GPa	Msi
	470.39	68.22	0.04	1584	229.7	1.92	59.1	8.58	1178.1	170.94
	413.39	59.96	0.034	1421	206.1	1.87	54.9	7.97	1217	176.59
	380	55.1	0.03	1064	154.3	0.9	82.7	12	1427	207.06
	338	49	0.02	1440	208.9	1.6	72.2	10.48	1520	220.55
	362	52.5	0.02	1461	211.9	1.9	58.6	8.5	1420	206.04
Average	392.76	56.96	0.03	1394	202.2	1.64	65.5	9.5	1352.4	196.24
S_{n-1}	51.38	7.45	0.01	195	28.3	0.43	11.64	1.69	147.4	21.39
CV((%)	13.1	13.1	30.5	14	14	26.4	17.8	17.8	10.9	10.9
max	470.39	68.22	0.04	1584	229.7	1.92	82.7	12	1520	220.55
min	338	49	0.02	1064	154.3	0.9	54.9	7.97	1178.1	170.94

S600-G0-S

	Transition Point			Ultimate Strength		Ultimate Strain	Modulus			
	Stress		Strain				Uncracked		Cracked	
	[MPa]	[ksi]	%	[MPa]	[ksi]	%	[GPa]	[Msi]	[GPa]	[Msi]
	565.49	82.0	0.0012	1332.06	193.2	0.90	461.8	66.98	97.9	14.19
	426.12	61.8	0.0004	1291.66	187.3	0.92	1,128.5	163.67	98.1	14.23
	669.30	97.1	0.0010	1440.33	208.9	1.58	621.3	90.11	52.3	7.59
	428.72	62.2	0.0003	1243.36	180.3	0.65	1,182.3	171.47	133.2	19.32
	706.68	102.5	0.0006	1432.00	207.7	1.09	1,262.5	183.11	69.9	10.13
	-	-	-	1405.59	203.9	1.31	1,254.5	181.95	128.7	18.66
	289.16	41.9	0.0006	1440.32	208.9	1.37	520.6	75.51	87.5	12.70
	448.91	65.1	0.0007	1422.91	206.4	1.10	604.9	87.74	94.6	13.71
	468.93	68.0	0.0007	1367.69	198.4	1.39	643.5	93.33	68.3	9.91
	138.50	20.1	0.0002	1437.67	208.5	2.04	865.0	125.46	64.4	9.34
Average	460.20	66.75	0.00	1381.36	200.35	1.23	854.49	123.93	89.49	12.98
S_{n-1}	177.01	25.67	0.00	70.48	10.22	0.39	322.48	46.77	26.81	3.89
CV((%)	38	38	51	5	5	32	37.7	38	30.0	30
Min	138.50	20.09	0.00	1243.36	180.33	0.65	461.83	66.98	52.32	7.59
Max	706.68	102.49	0.00	1440.33	208.90	2.04	1262.50	183.11	133.24	19.32

S600-L0-S

	Stress at Transition		Strain at Transition	Ultimate Strength		Ultimate Strain	Uncracked Modulus		Cracked Modulus	
	f_{ft}		ε_{ft}	f_{fu}		ε_{fu}	E*		Ef	
	[MPa]	[ksi]	%	[MPa]	[ksi]	%	[GPa]	[Msi]	[GPa]	[Msi]
	-	-	-	861.94	125.0	2.10	-	-	24.18	3.51
	208.94	30.3	0.000240	803.08	116.5	1.48	869.57	126.12	40.88	5.93
	299.83	43.5	0.000432	698.28	101.3	0.65	693.33	100.56	65.87	9.55
	175.45	25.4	0.000869	724.86	105.1	1.51	201.79	29.27	38.61	5.60
	283.48	41.1	0.000480	773.87	112.2	0.73	590.00	85.57	71.96	10.44
	459.56	66.7	0.002396	1034.47	150.0	1.94	191.76	27.81	33.78	4.90
	318.08	46.1	0.000755	1008.11	146.2	2.04	421.43	61.12	35.13	5.09
	381.00	55.3	0.000690	949.05	137.6	1.54	552.17	80.09	30.38	4.41
	377.00	54.7	0.000880	881.39	127.8	0.92	428.41	62.14	71.42	10.36
	365.00	52.9	0.000500	883.23	128.1	0.98	730.00	105.88	50.46	7.32
Average	318.70	46.22	0.000805	861.83	125.00	1.39	519.83	75.39	46.27	6.71
S_{n-1}	89.04	12.91	0.000634	113.70	16.49	0.54	231.67	33.60	17.64	2.56
CV((%)	28	28	79	13	13	39	45	45	38	38
Min	175.45	25.45	0.000240	698.28	101.28	0.65	191.76	27.81	24.18	3.51
Max	459.56	66.65	0.002396	1034.47	150.04	2.10	869.57	126.12	71.96	10.44

S1200-G0-S

	Transition Point			Ultimate Strength		Ultimate Strain	Modulus			
	Stress		Strain				Uncracked		Cracked	
	[MPa]	[ksi]	%	[MPa]	[ksi]	%	[GPa]	[Msi]	[GPa]	[Msi]
	-	-	-	711.25	103.2	1.80	-	-	39.5	5.73
	162.69	23.6	0.013	710.88	103.1	2.13	1296.7	188.07	27.3	3.97
	358.78	52.0	0.030	731.92	106.2	1.13	1192.0	172.89	44.8	6.50
	491.71	71.3	0.035	930.26	134.9	2.42	1422.6	206.34	21.1	3.06
	-	-	-	760.74	110.3	0.61	-	-	84.5	12.25
	359.20	52.1	0.023	796.36	115.5	1.04	1550.1	224.82	54.3	7.87
	-	-	-	743.97	107.9	0.74	-	-	58.8	8.52
	568.97	82.5	0.064	767.46	111.3	1.05	894.0	129.67	48.0	6.96
Average	388.27	56.31	0.033	769.11	111.5	1.36	1271.1	184.36	47.3	6.86
S_{n-1}	154.88	22.46	0.019	71.25	10.3	0.67	250.0	36.25	19.7	2.86
CV((%)	40	40	58	9	9	49	20	20	42	42
Min	162.69	23.60	0.01	710.88	103.1	0.61	894.0	129.67	21.1	3.06
Max	568.97	82.52	0.06	930.26	134.9	2.42	1550.1	224.82	84.5	12.25

S1200-L0-S

	Stress at Transition		Strain at Transition	Ultimate Strength		Ultimate Strain	Uncracked Modulus		Cracked Modulus	
	f_{ft}		ε_{ft}	f_{fu}		ε_{fu}	E*		Ef	
	[MPa]	[ksi]	%	[MPa]	[ksi]	%	[GPa]	[Msi]	[GPa]	[Msi]
	264.27	38.3	0.000566	605.15	87.8	1.14	414.48	60.12	31.31	4.54
	289.13	41.9	0.000764	534.33	77.5	0.84	342.22	49.64	32.10	4.66
	364.09	52.8	0.000979	618.66	89.7	1.01	344.27	49.93	27.91	4.05
	306.04	44.4	0.001294	614.35	89.1	0.96	220.93	32.04	36.87	5.35
	306.04	44.4	0.001294	614.35	89.1	0.96	220.93	32.04	36.87	5.35
	334.32	48.5	0.001370	687.61	99.7	0.93	252.16	36.57	44.50	6.45
	-	-	-	494.32	71.7	0.86	-	-	51.72	7.50
	-	-	-	616.85	89.5	1.14	-	-	33.88	4.91
	101.63	14.7	0.000443	706.84	102.5	1.73	250.30	36.30	35.94	5.21
	334.32	48.5	0.001370	687.61	99.7	0.93	252.16	36.57	44.50	6.45
Average	287.48	41.70	0.001010	618.01	89.63	1.05	287.18	41.65	37.56	5.45
S_{n-1}	81.09	11.76	0.000378	66.73	9.68	0.26	70.80	10.27	7.27	1.05
CV((%)	28	28	37	11	11	25	25	25	19	19
Min	264.27	38.33	0.000566	534.33	77.50	0.84	220.93	32.04	27.91	4.05
Max	364.09	52.81	0.001294	618.66	89.73	1.14	414.48	60.12	51.72	7.50

Bibliography

232-TDT, R. T. C. (2016). Recommendation of rilem tc 232-tdt: test methods and design of textile reinforced concrete: Uniaxial tensile test: test method to determine the load bearing behavior of tensile specimens made of textile reinforced concrete. *Materials and Structures*, *49*, 4923–4927.

Ahmed, H. I. & Robles-Austriaco, L. (1991). State-of-the-art report on rehabilitation and restrengthening of structures using ferrocement. *Journal of Ferrocement*, *21*(3), 243–258.

Akbari Hadad, H., Nanni, A., Ebead, U. A., & El Refai, A. (2018). Static and fatigue performance of frcm-strengthened concrete beams. *Journal of Composites for Construction*, *22*(5), 04018033.

Al-Kubaisy, M. & Jumaat, M. Z. (2000). Flexural behaviour of reinforced concrete slabs with ferrocement tension zone cover. *Construction and Building Materials*, *14*(5), 245–252.

Alecci, V., Focacci, F., Rovero, L., Stipo, G., & De Stefano, M. (2016). Extrados strengthening of brick masonry arches with pbo–frcm composites: Experimental and analytical investigations. *Composite Structures*, *149*, 184–196.

Alexander, D. (1991). Ferrocement retrofit hull for the rehabilitation of a historic wooden vessel. *Journal of Ferrocement*, *21*(3), 223–228.

Aljazaeri, Z. R. & Myers, J. J. (2017). Strengthening of reinforced-concrete beams in shear with a fabric-reinforced cementitious matrix. *Journal of Composites for Construction*, *21*(5), 04017041.

American Association of State Highway and Transportation Officials (AASHTO) (2014). *AASHTO LRFD Bridge Design Specifications*. Washington, D.C.

American Concrete Institute (ACI) (2013). *ACI 549. 4R-13: Guide to Design and Construction of Externally Bonded Fabric-Reinforced Cementitious Matrix (FRCM) Systems for Repair and Strengthening Concrete and Masonry Structures*. American Concrete Institute, Farmington Hill, MI, USA.

American Concrete Institute (ACI) (2014). *Building Code Requirements for Structural Concrete: (ACI 318-14)*. Farmington Hill, MI, USA.

Arboleda, D. (2014). *Fabric reinforced cementitious matrix (FRCM) composites for infrastructure strengthening and rehabilitation: Characterization methods*. Ph.D. thesis, University of Miami.

Ascione, L., de Felice, G., & De Santis, S. (2015). A qualification method for externally bonded fibre reinforced cementitious matrix (frcm) strengthening systems. *Composites Part B: Engineering*, *78*, 497–506.

ASTM A370-17a (2017). *Standard Test Methods and Definitions for Mechanical Testing of Steel Products*. West Conshohocken, PA, USA.

ASTM C39/C39M-18 (2018). *Standard Test Method for Compressive Strength of Cylindrical Concrete Specimens*. West Conshohocken, PA, USA.

Azam, R., Soudki, K., West, J. S., & Noël, M. (2017). Behavior of shear-critical rc beams strengthened with cfrcm. *Journal of Composites for Construction*, *22*(1), 04017046.

Babaeidarabad, S., Caso, F. D., & Nanni, A. (2013). Out-of-plane behavior of urm walls strengthened with fabric-reinforced cementitious matrix composite. *Journal of Composites for Construction*, *18*(4), 04013057.

Babaeidarabad, S., Loreto, G., & Nanni, A. (2014). Flexural strengthening of rc beams with an externally bonded fabric-reinforced cementitious matrix. *Journal of Composites for Construction*, *18*(5), 04014009.

Babaeidarabad, S. & Nanni, A. (2013). In-plane behavior of unreinforced masonry walls strengthened with fabricreinforced cementitious matrix (frcm). *ACI, Special Publication*.

Bakis, C. E., Bank, L. C., Brown, V., Cosenza, E., Davalos, J., Lesko, J., Machida, A., Rizkalla, S., & Triantafillou, T. (2002). Fiber-reinforced polymer composites for construction—state-of-the-art review. *Journal of Composites for Construction*, *6*(2), 73–87.

Balaguru, P., Nanni, A., & Giancaspro, J. (2008). *FRP composites for reinforced and prestressed concrete structures: A guide to fundamentals and design for repair and retrofit*. CRC Press.

Bathias, C. & Paris, P. C. (2004). *Gigacycle fatigue in mechanical practice*, volume 185. CRC Press.

Bellini, A., Incerti, A., Bovo, M., & Mazzotti, C. (2018). Effectiveness of frcm reinforcement applied to masonry walls subject to axial force and out-of-plane loads evaluated by experimental and numerical studies. *International Journal of Architectural Heritage*, *12*(3), 376–394.

Bisby, L. A., Green, M. F., & Kodur, V. K. (2005). Response to fire of concrete structures that incorporate frp. *Progress in Structural Engineering and Materials*, *7*(3), 136–149.

Borri, A., Casadei, P., Castori, G., & Hammond, J. (2009). Strengthening of brick masonry arches with externally bonded steel reinforced composites. *Journal of Composites for Construction*, *13*(6), 468–475.

Caggegi, C., Carozzi, F. G., De Santis, S., Fabbrocino, F., Focacci, F., Hojdys, Ł., Lanoye, E., & Zuccarino, L. (2017). Experimental analysis on tensile and bond properties of pbo and aramid fabric reinforced cementitious matrix for strengthening masonry structures. *Composites Part B: Engineering*, *127*, 175–195.

Carloni, C., Mazzotti, C., Savoia, M., & Subramaniam, K. V. (2014). Confinement of masonry columns with pbo frcm composites. *Key Engineering Materials*, *624*.

Carozzi, F. G., Bellini, A., D'Antino, T., de Felice, G., Focacci, F., Hojdys, Ł., Laghi, L., Lanoye, E., Micelli, F., Panizza, M., et al. (2017). Experimental investigation of tensile and bond properties of carbon-frcm composites for strengthening masonry elements. *Composites Part B: Engineering*, *128*, 100–119.

Cescatti, E., da Porto, F., & Modena, C. (2018). In-situ destructive testing of ancient strengthened masonry vaults. *International Journal of Architectural Heritage*, *12*(3), 350–361.

Chang, T. & Kesler, C. (1958). Fatigue behavior of reinforced concrete beams. In *Journal Proceedings*, volume 55, (pp. 245–254).

Colajanni, P., De Domenico, F., Recupero, A., & Spinella, N. (2014). Concrete columns confined with fibre reinforced cementitious mortars: experimentation and modelling. *Construction and Building Materials*, *52*, 375–384.

D'Ambrisi, A. D. & Focacci, F. (2011). Flexural strengthening of RC beams with cement based composites. *ASCE Journal of Composites for Construction*, *15*(5), 707–720.

de Felice, G., Aiello, M. A., Caggegi, C., Ceroni, F., De Santis, S., Garbin, E., Gattesco, N., Hojdys, Ł., Krajewski, P., Kwiecień, A., et al. (2018). Recommendation of rilem technical committee 250-csm: Test method for textile reinforced mortar to substrate bond characterization. *Materials and Structures*, *51*(4), 95.

De Santis, S., Casadei, P., De Canio, G., De Felice, G., Malena, M., Mongelli, M., & Roselli, I. (2016). Seismic performance of masonry walls retrofitted with steel reinforced grout. *Earthquake Engineering & Structural Dynamics*, *45*(2), 229–251.

De Santis, S., Ceroni, F., de Felice, G., Fagone, M., Ghiassi, B., Kwiecień, A., Lignola, G. P., Morganti, M., Santandrea, M., Valluzzi, M. R., et al. (2017). Round robin test on tensile and bond behaviour of steel reinforced grout systems. *Composites Part B: Engineering*, *127*, 100–120.

De Santis, S., Roscini, F., & de Felice, G. (2018). Full-scale tests on masonry vaults strengthened with steel reinforced grout. *Composites Part B: Engineering*, *141*, 20–36.

Emberson, N. & Mays, G. (1996). Significance of property mismatch in the patch repair of structural concrete. part 3: Reinforced concrete members in flexure. *Magazine of Concrete Research*, *48*(174), 45–57.

Faella, C., Martinelli, E., Nigro, E., & Paciello, S. (2010). Shear capacity of masonry walls externally strengthened by a cement-based composite material: an experimental campaign. *Construction and Building Materials*, *24*(1), 84–93.

Fossetti, M. & Minafò, G. (2016). Strengthening of masonry columns with bfrcm or with steel wires: an experimental study. *Fibers*, *4*(2), 15.

Garmendia, L., Larrinaga, P., García, D., & Marcos, I. (2014). Textile-reinforced mortar as strengthening material for masonry arches. *International Journal of Architectural Heritage*, *8*(5), 627–648.

Gonzalez-Libreros, J., Sneed, L., D'Antino, T., & Pellegrino, C. (2017). Behavior of rc beams strengthened in shear with frp and frcm composites. *Engineering Structures*, *150*, 830–842.

Hamid, A. A., Mahmoud, A., & El Magd, S. A. (1994). Strengthening and repair of unreinforced masonry structures: state-of-the-art. In *Proc., 10th Int. Brick and Block Masonry Conf*, volume 2, (pp. 485–497).

Helgason, T., Hanson, J., Somes, N., Corley, W., & Hognestad, E. (1976). Fatigue strength of high-yield reinforcing bars. *Nchrp Report*, (164).

Herrmann, A. W. (2013). Asce 2013 report card for america's infrastructure. In *IABSE symposium report*, volume 99, (pp. 9–10). International Association for Bridge and Structural Engineering.

ICC-Evaluation Service (2016). Proposed acceptance criteria for masonry and concrete strengthening using fiber-reinforced cementitious matrix (FRCM) composite systems (AC434). *ICC-Evaluation Service, Whittier, CA*.

Ismail, N., El-Maaddawy, T., Khattak, N., & Najmal, A. (2018). In-plane shear strength improvement of hollow concrete masonry panels using a fabric-reinforced cementitious matrix. *Journal of Composites for Construction*, *22*(2).

Kariou, F., Triantafyllou, S., Bournas, D., & Koutas, L. (2018). Out-of-plane response of masonry walls strengthened using textile-mortar system. *Construction and Building Materials*, *165*, 769–781.

Kazemi, M. T. & Morshed, R. (2005). Seismic shear strengthening of rc columns with ferrocement jacket. *Cement and Concrete Composites*, *27*(7), 834–842.

Lignola, G. P., Caggegi, C., Ceroni, F., De Santis, S., Krajewski, P., Lourenço, P. B., Morganti, M., Papanicolaou, C. C., Pellegrino, C., Prota, A., et al. (2017). Performance assessment of basalt frcm for retrofit applications on masonry. *Composites Part B: Engineering*, *128*, 1–18.

Loreto, G., Babaeidarabad, S., Leardini, L., & Nanni, A. (2015). Rc beams shear-strengthened with fabric-reinforced-cementitious-matrix (frcm) composite. *International Journal of Advanced Structural Engineering (IJASE)*, *7*(4), 341–352.

Mandell, J., McGarry, F., Hsieh, A.-Y., & Li, C. (1985). Tensile fatigue of glass fibers and composites with conventional and surface compressed fibers. *Polymer Composites*, *6*(3), 168–174.

Marcari, G., Basili, M., & Vestroni, F. (2017). Experimental investigation of tuff masonry panels reinforced with surface bonded basalt textile-reinforced mortar. *Composites Part B: Engineering*, *108*, 131–142.

Minafò, G. & La Mendola, L. (2018). Experimental investigation on the effect of mortar grade on the compressive behaviour of frcm confined masonry columns. *Composites Part B: Engineering*, *146*, 1–12.

Mourad, S. & Shannag, M. (2012). Repair and strengthening of reinforced concrete square columns using ferrocement jackets. *Cement and concrete composites*, *34*(2), 288–294.

Naamann, A. (2012). Evolution in ferrocement and thin reinforced cementitious composites. *Arabian Journal for Science and Engineering*, *37*(2), 421–441.

Nanni, A. (1993). Flexural behavior and design of RC members using FRP reinforcement. *Journal of structural engineering*, *119*(11), 3344–3359.

Nanni, A. (1995). Concrete repair with externally bonded FRP reinforcement. *Concrete International*, *17*(6), 22–26.

Ombres, L. (2014). Concrete confinement with a cement based high strength composite material. *Composite Structures*, *109*, 294–304.

Ombres, L. (2015a). Confinement effectiveness in eccentrically loaded masonry columns strengthened by fiber reinforced cementitious matrix (frcm) jackets. In *Key Engineering Materials*, volume 624, (pp. 551–558). Trans Tech Publ.

Ombres, L. (2015b). Structural performances of reinforced concrete beams strengthened in shear with a cement based fiber composite material. *Composite Structures*, *122*, 316–329.

Papanicolaou, C., Triantafillou, T., Papantoniou, I., & Balioukos, C. (2009). Strengthening of two-way slabs with textile-reinforced mortars (trm). In *Proceedings 11th International Fib Symposium, London*.

Papanicolaou, C. G., Triantafillou, T. C., Karlos, K., & Papathanasiou, M. (2007). Textile-reinforced mortar (trm) versus frp as strengthening material of urm walls: in-plane cyclic loading. *Materials and Structures*, *40*(10), 1081–1097.

Papanicolaou, C. G., Triantafillou, T. C., Papathanasiou, M., & Karlos, K. (2008). Textile reinforced mortar (trm) versus frp as strengthening material of urm walls: out-of-plane cyclic loading. *Materials and Structures*, *41*(1), 143–157.

Paris, P. C. (1961). A rational analytic theory of fatigue. *Trends Engin*, *13*, 9–14.

Pino, V., Akbari Hadad, H., De Caso y Basalo, F., Nanni, A., Ali Ebead, U., & El Refai, A. (2017). Performance of frcm-strengthened rc beams subject to fatigue. *Journal of Bridge Engineering*, *22*(10), 04017079.

Pino, V., Hadad, H. A., De Caso, F., Nanni, A., Ebead, U. A., & El Refai, A. (2016). Performance of FRCM strengthened RC beams subject to fatigue. In *Sustainable Construction Materials and Technologies (SCMT4)*, Las Vegas, USA.

Pino, V. A. (2016). *Fabric reinforced cementitious matrix (FRCM) composites as a repair system for transportation infrastructure*. Ph.D. thesis, University of Miami.

Prota, A., Marcari, G., Fabbrocino, G., Manfredi, G., & Aldea, C. (2006). Experimental in-plane behavior of tuff masonry strengthened with cementitious matrix–grid composites. *Journal of Composites for Construction*, *10*(3), 223–233.

Ramaglia, G., Lignola, G. P., Balsamo, A., Prota, A., & Manfredi, G. (2016). Seismic strengthening of masonry vaults with abutments using textile-reinforced mortar. *Journal of Composites for Construction*, *21*(2), 04016079.

CEN European Committee for Standardization (2002). *Eurocode 0: Basis of structural design*. Brussels, BE: BSi.

CEN European Committee for Standardization (1995). *BS EN 2561-1995 Carbon fibre reinforced plastics, Undirectional laminates, Tensile test parallel to the fibre direction*. Brussels, BE: BSi.

Santandrea, M., Quartarone, G., Carloni, C., & Gu, X. L. (2017). Confinement of masonry columns with steel and basalt frcm composites. In *Key Engineering Materials*, volume 747, (pp. 342–349). Trans Tech Publ.

Tekieli, M., De Santis, S., de Felice, G., Kwiecień, A., & Roscini, F. (2017). Application of digital image correlation to composite reinforcements testing. *Composite Structures*, *160*, 670–688.

Triantafillou, T. C. & Papanicolaou, C. G. (2006). Shear strengthening of reinforced concrete members with textile reinforced mortar (trm) jackets. *Materials and structures*, *39*(1), 93–103.

Valluzzi, M. R., Da Porto, F., Garbin, E., & Panizza, M. (2014). Out-of-plane behaviour of infill masonry panels strengthened with composite materials. *Materials and Structures*, *47*(12), 2131–2145.

Walton, J. & Yeung, Y. Flexible tension members from composite materials. In *Proc. of the Sixth Int. OMAE Symp*, volume 3.

Zhao, X.-L. & Zhang, L. (2007). State-of-the-art review on frp strengthened steel structures. *Engineering Structures*, *29*(8), 1808–1823.